High Efficient Power Electronic Converter for new Generator Technology

Dimopoulos, Emmanouil

Publication date:
2015

Document Version
Publisher's PDF, also known as Version of record

HIGH EFFICIENT POWER ELECTRONIC CONVERTER FOR NEW GENERATOR TECHNOLOGY

EMMANOUIL DIMOPOULOS

DISSERTATION SUBMITTED TO THE
FACULTY OF ENGINEERING & SCIENCE AT
AALBORG UNIVERSITY
IN CANDIDACY FOR THE DEGREE OF
DOCTOR OF PHILOSOPHY IN ELECTRICAL ENGINEERING

RECOMMENDED FOR ACCEPTANCE
BY THE DEPARTMENT OF ENERGY TECHNOLOGY

SUPERVISOR: STIG MUNK-NIELSEN

MAY 2015

Title:	High efficient power electronic converter for new generator technology
Author:	Emmanouil Dimopoulos
PhD Supervisor:	Prof. Stig Munk-Nielsen, Aalborg University
PhD Committee:	Prof. Frede Blaabjerg, Aalborg University
	Prof. Jorma Kyyrä, Aalto University
	Prof. Alex Van den Bossche, Ghent University
PhD Project Title:	Highly efficient low cost energy generation and actuation using disruptive DEAP technology. Højteknologifonden J.nr. 009-2011-2
PhD Project Type:	Paper-based
PhD Project Period:	June 2012 -June 2015
Collaborators:	Aalborg University Bang & Olufsen A/S Danfoss A/S Danfoss PolyPower A/S ESS Technology A/S Noliac A/S Polyteknik A/S Technical University of Denmark University of Southern Denmark Wave Star A/S

Aalborg University
Department of Energy Technology
Pontoppidanstræde 101
DK-9220 Aalborg East
Aalborg University Press
ISBN: 978-87-92846-61-7

List of published papers:

- Emmanouil Dimopoulos, Ionut Trintis, Stig Munk-Nielsen, 'Energy Harvesting Cycles of Dielectric ElectroActive Polymer Generators', *38th Annual Conference on IEEE Industrial Electronics Society (IECON 2012)*, Montreal, Canada, 2012.
- Emmanouil Dimopoulos, Ionut Trintis, Stig Munk-Nielsen, 'Comparison of the dielectric electroactive polymer generator energy harvesting cycles', *Proceedings of the SPIE Smart Structures and Materials / Nondestructive Evaluation and Health Monitoring: ElectroActive Polymer Actuators and Devices (EAPAD 2013)*, San Diego CA, USA, 2013.
- Ionut Trintis, Emmanouil Dimopoulos, Stig Munk-Nielsen, 'Simple DCM or CCM analog peak current controller for HV capacitor charge-discharge applications', *15th European Conference on Power Electronics and Applications (EPE 2013)*, Lille, France, 2013.
- Emmanouil Dimopoulos, Ionut Trintis, Stig Munk-Nielsen, Björn Rechenbach, Morten Willatzen, Benny Lassen, 'An Electromechanical Model of a Dielectric ElectroActive Polymer Generator', *15th European Conference on Power Electronics and Applications (EPE 2013)*, Lille, France, 2013.
- Emmanouil Dimopoulos, Stig Munk-Nielsen, 'Serializing off-the-shelf MOSFETs by Magnetically Coupling Their Gate Electrodes', *15th European Conference on Power Electronics and Applications (EPE 2013)*, Lille, France, 2013.
- Emmanouil Dimopoulos, Stig Munk-Nielsen, 'Scaling the serialization of MOSFETs by Magnetically Coupling Their Gate Electrodes', *Energy Conversion Congress and Exposition (ECCE 2013)*, Denver CO, USA, 2013.
- Emmanouil Dimopoulos, Stig Munk-Nielsen, 'A Tapped-Inductor Buck-Boost Converter for a Dielectric ElectroActive Polymer Generator', *Applied Power Electronics Conference and Exposition (APEC 2014)*, Dallas TX, USA, 2014.
- Emmanouil Dimopoulos, Stig Munk-Nielsen, 'A tapped-inductor buck-boost converter for a multi-DEAP generator energy harvesting system', *Proceedings of the SPIE Smart Structures and Materials / Nondestructive Evaluation and Health Monitoring: ElectroActive Polymer Actuators and Devices (EAPAD 2014)*, San Diego CA, USA, 2014.
- Tahir Lağap, Emmanouil Dimopoulos, Stig Munk-Nielsen, 'An RCDD Snubber for a Bidirectional Flyback Converter', *17th European Conference on Power Electronics and Applications (EPE 2015)*, Geneva, Switzerland, Sep. 2015, accepted.

This page is intentionally left blank

Abstract

This PhD dissertation summarizes the experience accumulated over three-years of research on Dielectric ElectroActive Polymer (DEAP) generators; conducted within the seventh Work-Package (WP7) framework of Innovation Fund Denmark €15 million project '*Highly efficient low cost energy generation and actuation using disruptive DEAP technology*' (Højteknologifonden J.nr. 009-2011-2).

In particular, WP7 primary goal was to investigate the degree of high-efficient, cost-effective, large-scale, potential applicability of Danfoss PolyPower® A/S DEAP generators to wave energy harvesting applications, due to the latter one's direct energy conversion feature and prominent low-speed performance. To that end, and after a brief introduction of Danfoss PolyPower® A/S DEAP technology, a meticulous and precise electromechanical model of a DEAP generator, accounting for both the visco-hyperelastic characteristics of the elastomer as well as the latter one's stretch-dependent capacitance, was designed, tuned via merely mechanical experiments and assessed via direct juxtaposition with actual experimental data, under all distinct energy harvesting cycles; namely the Constant Charge (CC), Constant Voltage (CV) and Constant E-field (CE).

In addition, a first complete energy harvesting system, i.e. demo#0, was build to facilitate the conduction of experimental work on several mechanically in-phase co-cycled DEAP generators. Post the establishment of an appropriate comparative benchmark, the DEAP generators energy harvesting cycles were, for the first time, experimentally outlined and compared, by means of energy gain, energy harvesting efficiency and energy conversion efficiency, by employing a typical non-isolated bidirectional half-bridge buck-boost converter. In a nonpareil demo#0 energy harvesting experiment, mechanical energy was successfully converted into electrical one with a 3.5 % energy conversion efficiency.

Yet, and as demonstrated in demo#0 experiments, great challenges are imposed on the power electronic converter design, by the necessity for bidirectional energy flow in an energy harvesting cycle, under high step-up and high step-down voltage conversion ratios, accompanied by low-average but relatively high-peak currents; let alone that the effective operational range of the latter one is usually limited by the lack of commercially-available, high-efficient, high-voltage, low-power switches. Hence, and towards the establishment of such a prominent power semiconductor device, the gate balancing core stacking technique was revisited and a new design specification for its transformer interwinding capacitance was derived, enabling the serialization of low-power MOSFETs.

Assuredly, besides enabling the out-of-phase co-cycling of several DEAP generators, increasing the utilization factor of the infrastructure input mechanical energy by 86.8 %, demo#1 drove the DEAP generators at high E-field strength values, by employing a power electronic converter prototype, based on a

string of three (3) off-the-shelf non-matched non-thermally-coupled MOSFETs. Demo#1 achieved energy conversion efficiency of 7 %, characterized by energy density of 2 J/kg of active material, which was - at date - a world-first for an active power electronic converter coupled to such a sizeable DEAP generator.

Unfortunately, all voluminous DEAP generators, designed to accommodate the operation of the final demonstrator, i.e. demo#2, towards the scaling-up of the energy harvesting system, experienced early destructive electrical breakdowns and they were thus rendered inoperative. However, new, smaller scale DEAP generators were manufactured, validating the applicability of demo#2 novel converter to DEAP-generator-based energy harvesting systems. Indeed, founding its - up to 3000 V - operation on the revised gate balancing core technique, the corresponding tapped-inductor buck-boost converter demonstrated high-efficient bidirectional energy flow, above 94 % for the buck function and 92 % for the boost function, under high step-up and high step-down voltage conversion ratios, accompanied by low-average but relatively high-peak currents.

Finally, this PhD dissertation is concluded with a judicious perspective analysis on the DEAP technology and its potential large-scale commercialization, highlighting key activities in areas such as the DEAP film research and development and the DEAP film production, as well as trends in modern power electronic converters and semiconductors; materializing WP7 years of experience and collaboration with seven (7) industrial partners and three (3) universities.

This page is intentionally left blank

This page is intentionally left blank

Resumé

Denne ph.d.-afhandling sammenfatter erfaringer gennem tre års forskning i Dielektriske Elektro Aktive Polymer (DEAP) generatorer og gennemføres inden for rammerne af projektet '*Highly efficient low cost energy generation and actuation using disruptive DEAP technology'* i arbejdspakke syv (WP7). Det er et innovationsfonds projekt med et samlet budget på 97 millioner (Højteknologifonden J.nr. 009-2011-2).

Primært var målet for WP7 at undersøge mulighederne for højeffektiv, billig og skalerbar anvendelse af Danfoss PolyPower® A/S DEAP generatorer ved omdannelse af bølgeenergi til elektriskenergi. I ph.d.-afhandlingen beskrives først grundlæggende principper for energiomdannelse. Dernæst præsenteres en elektromekanisk model af DEAP generatorer inkluderende viskositet samt stræk afhængig kapacitet. Modellen er udviklet og parametre til model er fundet ved eksperimentelle test hvor generatoren har arbejdet ved tre forskellige kontrol måder: konstant ladning (CC), konstant spænding (CV) og konstant E-felt (CE).

Demonstratorer er udviklet for at muliggøre eksperimentelle forsøg som kan teste DEAP teknologien. Den første demo#0, anvendes til at teste enkelt element DEAP generatorer, inden at der blev bygget en DEAP generator med flere elementer. Dernæst udføres målinger af genereret af elektrisk energi, effektivitet i omsætning fra mekanisk til elektrisk energi måles for første gang. Der måles en effektivitet på 3.5 % inklusiv effekttab i den anvendte ikke isoleret halvbro konverter.

Under arbejdet med demo#0 blev det tydeligt at der er tekniske udfordringer forbundet med at lave en effektelektronisk konverter som skal høste DEAP generator energi. Konverteren skal være i stand til at modtage og sende energi, dernæst skal DEAP spændingen som er pulserende med en maksimal spænding på flere 1000 V konverteres til en spænding som er konstant og omkring 300 V. Der er også en pulserende strøm hvis peak værdi er markant højere end middelværdien, høj spænding og høj peak strøm gør det vanskeligt at købe en standard effekthalvleder som kan anvendes i konverterne. Derfor er der udviklet en design metodik til seriekobling af standard MOSFET effekthalvledere ved brug af gate seriekoblede transformatorer.

Med demo#1 opbygges en DEAP generator med plads til fire aktive elementer hvilket muliggør øget udnyttelse af mekanisk energi med 87 % i forhold til enkelt element generatoren. Der blev anvendt seriekobling af tre standard MOSFET effekthalvledere og konstant E-felt kontrol ved test og en mekanisk til elektrisk effektivitet på 7 % blev målt samt der blev opnået en energitæthed på 2 J/kg aktivt DEAP materiale hvilket på det tidspunkt var det højest rapportere i videnskabelig litteratur på verdensplan.

Beklageligvis var arbejdet mod demo#2 som er en eskaleret generator ramt af kort levetid for DEAP generator elementerne som skyldes spændingsoverslag og mekanisk slitage hvilket umuliggjorde at opbygge en funktionel demo#2. Alternativt til en større generator blev fabrikeret enkelte DEAP generator elementer som viser forbedringer i materialet og konstruktion. Der blev udført test op til 3000 V med seriekoble MOSFETS og der blev vist målte virkningsgrader for buck konverter delen på 94 % og for boost konverter delen på 92 %.

Til slut i ph.d.-afhandling konkluderes perspektiverne for DEAP teknologien og potentiale for stor-skala kommercialisering med fokus på DEAP polymer forskning og udvikling og DEAP polymer i produktion samt trend inden for moderne effektelektronikske konvertere og halvlederteknologi, baseret på tre års erfaring i arbejdspakke syv (WP7) og det øvrige samarbejde med projektets syv industrielle partnere og tre universitets partnere.

This page is intentionally left blank

This page is intentionally left blank

Acknowledgements

I would primarily like to thank my supervisor Professor Stig Munk-Nielsen, for his proficient and meticulous guidance throughout the entire PhD project period as well as for our wonderful cooperation and the numerous enlightening discussions we held. Many thanks to Ionut Trintis, Assistant Professor, who, besides his valuable scientific input, introduced me to the academia world. Furthermore, I would like to express my gratitude to Carsten Karup Nielsen, Staff Member, for all his technical support during the design, assembling and debugging of all printed circuits boards associated with this PhD project.

I would also like to acknowledge the financial support from the Innovation Fund Denmark under the '*Highly efficient low cost energy generation and actuation using disruptive DEAP technology*' project (J.nr. 009-2011-2). Many thanks to all the - more than 120 - project members. Special thanks to Jens Yde Juul, Project Manager at Danfoss PolyPower® A/S, Laurent Marquis, Technical Director at Wave Star® A/S and Sarban Rahimullah, Director and Partner at LEAP Technology ApS, for broadening my horizons with their interdisciplinary expertise, via our close collaboration and round-the-clock exchange of ideas.

I would also like to thank Hans-Erik Kiil, Director of Research & Development at Danfoss PolyPower® A/S and Benjamin Thomsen, Director and Partner at LEAP Technology ApS, for their zeal to share knowledge and experiences, while introducing me to the basics of the DEAP technology. Additional thanks, to the late Jes Kristensen, Technical Director at ESS® Technology A/S, for all his help during the design and manufacturing of demonstrator #1 as well as to Enrique Vidal Sanchez, Senior R&D engineer at Wave Star® A/S, for our pleasant and enriching discussions during the demonstrator modelling efforts.

I would further like to address my thanks to Björn Rechenbach, PhD Fellow at Southern University of Denmark (SDU), Morten Willatzen, Professor at SDU and at Technical University of Denmark (DTU) and Benny Lassen, Associate Professor at SDU, for our collaboration towards the acquisition of an electromechanical model for a dielectric electroactive polymer generator, as our research solidified and enhanced my understanding of the elastomer physical properties.

I am grateful to Jan Christiansen and Danny Rabih Friwat, Assistant Engineers at Aalborg University (AAU), for their contribution in designing and assembling demonstrators #0 and #1 as well as for all their help in installing the various sensors used within the framework of this PhD project. I am additionally thankful to Walter Neumayr, Assistant Engineer at AAU, for his invaluable help in acquiring all necessary components and pieces of equipment.

I would also like to thank all my colleagues and AAU students, for forming a prosperous working environment and more specifically I would like to acknow-

ledge Pramod Ghimire, Dong Wang and Nicolae Cristian Sintamarean with whom I shared office for more than two years during my PhD project. Special acknowledgements to my late colleague and friend Adrian Augustin Hasmasan.

I am also grateful to Tahir Lağap, Power Electronics Engineer at Danfoss® VLT drives, with whom I worked closely for two years during his MSc studies. Many thanks to Anna Miltersen, Project Secretary at AAU, and the rest of AAU secretarial staff for their devoted help. Last, but most certainly not least, I would like to express my most sincere gratitude to my family and life-lasting friends, whose multilateral support strengthened me over the last three years.

Emmanouil Dimopoulos

Aalborg, May 2015

To My Family
Anastasios, Despoina and Sotirios.

This page is intentionally left blank

Contents

This page is intentionally left blank

Nomenclature

Latin symbols

A_x	DEAP sheet area on the x-axis [m^2]
A_y	DEAP sheet area on the y-axis [m^2]
A_z	DEAP sheet area on the z-axis [m^2]
C	DEAP generator capacitance [F]
$C^{(0)}$	Undeformed DEAP generator capacitance [F]
$C^{(\lambda_x)}$	DEAP generator capacitance at λ_x stretch [F]
C_1	Snubber #1 capacitance [F]
C_2	Snubber #2 capacitance [F]
C_3	Snubber #3 capacitance [F]
$C^{(0)}_{\text{exp}}$	Undeformed DEAP generator capacitance (empirical value) [F]
C_{gd}	MOSFET Miller capacitance [F]
C_{sheet}	DEAP sheet capacitance [F]
C_{01}	Mooney-Rivlin model material constant [Pa]
C_{10}	Mooney-Rivlin model material constant [Pa]
$C_{\text{gd}_{\text{off}}}$	MOSFET Miller capacitance during turn-off [F]
$C_{\text{gd}_{\text{on}}}$	MOSFET Miller capacitance during turn-on [F]
C_{w}	Transformer interwinding capacitance [F]
C_{ies}	MOSFET input capacitance [F]
d_z	DEAP sheet thickness on the z-axis [m]
$d_z^{(0)}$	Undeformed DEAP sheet thickness on the z-axis [m]

E	DEAP sheet/generator electric field strength [Vm^{-1}]
$E^{''}$	Tensile loss modulus [Pa]
$E^{'}$	Tensile storage modulus [Pa]
E_{charge}	Boost function targeted E-field strength [Vm^{-1}]
E_{max}	DEAP generator maximum attainable E-field strength during an energy harvesting cycle [Vm^{-1}]
E_{min}	DEAP generator minimum attainable E-field strength during a CE cycle relaxation phase [Vm^{-1}]
E_{rated}	DEAP sheet/generator rated electric field strength [Vm^{-1}]
F	DEAP generator force [N]
f	DEAP generator cycling frequency [Hz]
I_{g}	MOSFET gate current [A]
$I_{\mathrm{g_{off}}}$	MOSFET gate current during turn-off [A]
$I_{\mathrm{g_{on}}}$	MOSFET gate current during turn-on [A]
$I_{L_{\mathrm{s,peak}}}$	Transformer secondary inductance peak current [A]
$I_{C_{\mathrm{w,off}}}$	Transformer interwinding capacitance current during turn-off [A]
$I_{C_{\mathrm{w,on}}}$	Transformer interwinding capacitance current during turn-on [A]
$I_{C_{\mathrm{w}}}$	Transformer interwinding capacitance current [A]
L	Overall tapped-inductance [H]
L_{lk}	Transformer leakage inductance [H]
L_{m}	Transformer magnetizing inductance [H]
L_{p}	Transformer primary inductance [H]
L_{s}	Transformer secondary inductance [H]
l_x	DEAP sheet length on the x-axis [m]
$l_x^{(0)}$	Undeformed DEAP sheet length on the x-axis [m]
l_y	DEAP sheet width on the y-axis [m]
$l_y^{(0)}$	Undeformed DEAP sheet width on the y-axis [m]
$l_z^{(0)}$	Undeformed DEAP generator thickness on the z-axis [m]
$L_{\mathrm{p_{lk}}}$	Transformer primary leakage inductance [H]
$L_{\mathrm{s_{lk}}}$	Transformer secondary leakage inductance [H]

m	DEAP generator mass [kg]
N	Number of Maxwell elements present in the Zener model [−]
n	Number of parallel-connected DEAP sheets [−]
n_{act}	Tapped-inductor actual turns ratio [−]
n_{eff}	Tapped-inductor effective turns ratio [−]
n_{st}	Number of serialized switches [−]
n_s	Number of acquired samples [−]
$p^{(0)}$	Zener model standalone spring Lagrange multiplier [−]
$p^{(j)}$	Zener model j-th spring Lagrange multiplier [−]
Q	DEAP generator internal charge [C]
$q^{(0)}$	Zener model standalone spring Lagrange multiplier [−]
$q^{(j)}$	Zener model j-th spring Lagrange multiplier [−]
R'_{g}	Total gate resistance [Ohm]
R_1	Snubber #1 resistor [Ohm]
R_2	Snubber #2 resistor [Ohm]
R_3	Snubber #3 resistor [Ohm]
R_{B}	Balancing resistor [Ohm]
R_{d}	Driver resistor [Ohm]
R_{g}	Gate resistor [Ohm]
R_{parallel}	DEAP generator shunt resistance [Ohm]
R_{serial}	DEAP generator series resistance [Ohm]
R_{probe}	Probe impedance [Ohm]
$t_{\mathrm{boost,on}}$	Boost transistor on-time [s]
$t_{\mathrm{buck,on}}$	Buck transistor on-time [s]
U_{probe}	Probe loss [J]
U_e	DEAP generator electric potential energy [J]
u_E	Electrostatic field energy density [Jm^{-3}]
U_m	DEAP generator mechanical potential energy [J]
$U_{e,\max}$	DEAP generator maximum electric potential energy during an energy harvesting cycle [J]

$U_{e,\text{net,DC-link}}$	DC-link net electric potential energy [J]
$U_{e,\text{net,DEAP}}$	DEAP generator net electric potential energy [J]
$U_{e,\text{net}}$	Capacitor net electric potential energy [J]
$U_{e,\text{post}}$	Capacitor electric potential energy post to a buck/boost function [J]
$U_{e,\text{prior}}$	Capacitor electric potential energy prior to a buck/boost function [J]
$U_{m,\text{eff}}$	DEAP generator effective mechanical potential energy [J]
$U_{m,\text{max}}$	DEAP generator maximum mechanical potential energy during an energy harvesting cycle [J]
$U_{m,\text{rel}}$	DEAP generator mechanical potential energy during the relaxation phase [J]
$U_{m,\text{str}}$	DEAP generator mechanical potential energy during the stretching phase [J]
V_{cc}	MOSFET driving pulse signal amplitude [V]
$V_{\text{DC-link}}$	DC-link voltage [V]
V_{DEAP}	DEAP generator electrical equivalent circuit input voltage [V]
V_{gs}	MOSFET gate-to-source voltage [V]
V_{max}	DEAP generator maximum voltage during a CV cycle relaxation phase [V]
V_{min}	DEAP generator minimum voltage during a CV cycle relaxation phase [V]
V_{ol}	DEAP sheet volume [m^3]
V_{pl}	MOSFET gate-to-source plateau voltage [V]
V_c	Voltage applied across the DEAP generator electrodes [V]
$V_{\text{T}_{\text{boost}}}$	Voltage stress across the converter boost switch [V]
$V_{\text{T}_{\text{buck}}}$	Voltage stress across the converter buck switch [V]
w	DEAP generator elastic energy density [Jm^{-3}]
x	DEAP displacement [m]
X_C	DEAP capacitance reactance [Ohm]
$\dot{A}_z$	Time derivative of the DEAP sheet area on the z-axis [m^2s^{-1}]
$\dot{C}$	Time derivative of the DEAP generator capacitance [Fs^{-1}]
$\dot{d}_z$	Time derivative of the DEAP sheet thickness on the z-axis [ms^{-1}]

$\dot{E}$	Time derivative of the DEAP sheet/generator electric field strength [$\mathrm{Vm^{-1}s^{-1}}$]
$\dot{Q}$	Time derivative of the DEAP generator internal charge [$\mathrm{Cs^{-1}}$]
$\tan\delta$	Loss angle tangent [−]
$\bar{U}_m$	DEAP generator mean mechanical potential energy [J]
$\bar{U}_{m,\mathrm{quad}}$	Quadruple rig mean mechanical input energy [J]
$\dot{U}_e$	Time derivative of the DEAP generator electric potential energy [$\mathrm{Js^{-1}}$]
$\bar{V}_{\mathrm{DC\text{-}link}}$	DC-link mean voltage [V]
$\dot{V}_{\mathrm{ol}}$	Time derivative of the DEAP sheet volume [$\mathrm{m^3s^{-1}}$]
$\dot{V}_c$	Time derivative of the voltage applied across the DEAP generator electrodes [$\mathrm{Vs^{-1}}$]
$\dot{V}_{\mathrm{ds_{off}}}$	Time derivative of the MOSFET drain-to-source voltage during turn-off [$\mathrm{Vs^{-1}}$]
$\dot{V}_{\mathrm{ds_{on}}}$	Time derivative of the MOSFET drain-to-source voltage during turn-on [$\mathrm{Vs^{-1}}$]
$\dot{V}_{C_{\mathrm{w}}}$	Time derivative of the transformer interwinding capacitance voltage [$\mathrm{Vs^{-1}}$]

Greek symbols

α	Geometrical deformation constant [−]
ΔT_{on}	Time delay [s]
ΔU	Energy gain [J]
ΔU_{abs}	Energy harvestng cycle absolute energy gain [J]
$\Delta U_{\mathrm{CC,abs}}$	Constant Charge cycle absolute energy gain [J]
$\Delta U_{\mathrm{CC,rel}}$	Constant Charge cycle relative energy gain [J]
$\Delta U_{\mathrm{CE,abs}}$	Constant E-field cycle absolute energy gain [J]
$\Delta U_{\mathrm{CE,rel}}$	Constant E-field cycle relative energy gain [J]
$\Delta U_{\mathrm{CV,abs}}$	Constant Voltage cycle absolute energy gain [J]
$\Delta U_{\mathrm{CV,rel}}$	Constant Voltage cycle relative energy gain [J]
δ	Loss angle [^{o}]
ε	Elastomer permittivity [$\mathrm{Fm^{-1}}$]

ε_0	Vacuum space permittivity [Fm^{-1}]
$\varepsilon_{\mathrm{rel}}$	Elastomer relative permittivity [−]
ζ	Damping ratio [−]
η_{boost}	Energy efficiency of converter boost function [%]
η_{buck}	Energy efficiency of converter buck function [%]
η_{con}	Energy conversion efficiency [%]
η_{cycle}	Energy harvesting cycle efficiency [%]
η_{DEAP}	DEAP generator mechanical efficiency [%]
κ	Constant reflecting the degree of anisotropy [−]
λ_{A}	Stretch amplitude [−]
λ_{B}	Stretch bias [−]
$\lambda_{\mathrm{x,max}}$	DEAP generator maximum stretch during an energy harvesting cycle [−]
$\lambda_{\mathrm{x,min}}$	DEAP generator pre-stretch [−]
λ_x	Stretch on the x-axis [−]
λ_y	Stretch on the y-axis [−]
λ_z	Stretch on the z-axis [−]
${\lambda_{\mathrm{e}}^{(j)}}_i$	Stretches of the spring in the j-th Maxwell element [−]
${\lambda_{\mathrm{v}}^{(j)}}_i$	Stretches of the dashpot in the j-th Maxwell element [−]
${\dot{\lambda}_{\mathrm{v}}^{(j)}}_i$	Time derivative of the j-th Maxwell element dashpot stretches [s^{-1}]
$\dot{\lambda}_x$	Time derivative of the stretch on the x-axis [s^{-1}]
$\dot{\lambda}_y$	Time derivative of the stretch on the y-axis [s^{-1}]
$\dot{\lambda}_z$	Time derivative of the stretch on the z-axis [s^{-1}]
$\mu_{\mathrm{e}}^{(j)}$	Shear modulus of the spring in the j-th Maxwell element [Pa]
$\mu_{\mathrm{v}}^{(j)}$	Viscosity of the dashpot in the j-th Maxwell element [$\mathrm{Pa}^{-1}\mathrm{s}^{-1}$]
$\xi_{\mathrm{v}}^{(1)}$	Rate dependency of the damping constant of the 1^{st} Maxwell element dashpot [Pa]
ρ	Density [gcm^{-3}]

σ	Stress [Pa]
σ_{diel}	Dielectric stress [Pa]
σ_x	Stress on the x-axis [Pa]
σ_y	Stress on the y-axis [Pa]
σ_z	Stress on the z-axis [Pa]
${\sigma_{\text{e}}^{(j)}}_i$	Stresses of the spring in the j-th Maxwell element [Pa]
τ	Torque [Nm]
τ_{e}	DEAP generator electrical equivalent circuit time constant [s]
τ_{v}	Time constant of the 1$^{\text{st}}$ Maxwell element dashpot [Pas]
ϕ	Phase [^{o}]
$\Phi^{(j)}$	Elastic energy density stored in the j-th spring of the Zener model [Jm^{-3}]
$\Phi_{\text{con}}^{(j)}$	Elastic energy density stored in the j-th spring of the Zener model satisfying the incompressibility constraint [Jm^{-3}]
$\Phi_{\text{sc}}^{(j)}$	Elastic energy density stored in the j-th spring of the Zener model due to the stretching/compressing mechanisms [Jm^{-3}]
Ψ	Elastic energy density stored in the standalone spring of the Zener model [Jm^{-3}]
Ψ_{con}	Elastic energy density stored in the standalone spring of the Zener model satisfying the incompressibility constraint [Jm^{-3}]
Ψ_{diel}	Dielectric elastic energy density stored in the standalone spring of the Zener model [Jm^{-3}]
Ψ_{sc}	Elastic energy density stored in the standalone spring of the Zener model due to the stretching/compressing mechanisms [Jm^{-3}]
ω	Angular velocity [rads^{-1}]

Subscript

b	Integer reflecting one of the three designed snubbers $b \in \{1, 2, 3\}$
i	Symbol reflecting one of the three coordinate axes $i \in \{x, y, z\}$
k	Integer reflecting the acquired sample number $k \in [1, n_s]$

Superscript

j	Integer corresponding to a Maxwell element $j \in (1, N)$

This page is intentionally left blank

This page is intentionally left blank

This page is intentionally left blank

Chapter 1

Introduction

1.1 Background

Scientists have long sought to develop smart materials, that alter some of their properties when subjected to an external stimuli like stress, temperature, pH, moisture and magnetic or electric fields, as these materials hold a lot of promise, as potential alternatives to several conventional technologies [**?**]. Indeed, the reversible and repetitive properties amendment exhibited by smart materials, qualifies them as highly attractive candidates for numerous modern transducer applications like actuators, sensors or even generators. In addition to that, their unparalleled capabilities have rekindled the interest of interdisciplinary scientists and engineers in the likelihood of another technological breakthrough.

Dielectric Elastomers (DEs) in particular, reflect one of the most prominent smart electroactive materials, as they have demonstrated several unique features against their competing electromagnetic and field-activated technologies; like superior low-speed performance, silent and direct energy conversion, large and rapid deformation under moderate forces, light-weight and pliable structure, high elastic energy density and relatively low-cost film fabrication [**?**, **?**]. As off today, (i.e. 10/05/2015), a search in google.com/patents [**?**][1] of the key-phrase '*ElectroActive Polymer*' yields more than hundred thousand (100.000) patents.

In 2008, and after more than ten (10) years of research, Danfoss PolyPower® A/S was established, as a separate company within the Danfoss® group, with the mandate to commercialize PolyPower® products, based on a new, smart and soft electroactive material titled Dielectric ElectroActive Polymer (DEAP).

[1] Google Patents database includes patents from the United States Patent and Trademark Office (USPTO) [**?**], European Patent Office (EPO) [**?**] and the World Intellectual Property Organization (WIPO) [**?**].

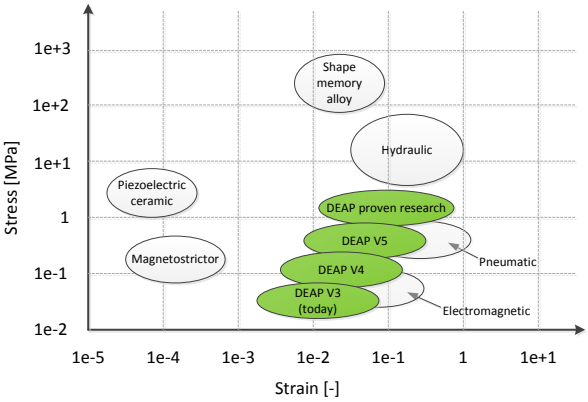

Figure 1.1: Typical stress-strain performance ranges for actuator technologies, including projected DEAP performance (content adapted from [?, ?] and figure reproduced from [?]).

Today, both a dedicated R&D department and a role-to-role film production process, capable of fabricating several kilometres of DEAP film per week, are in place at Danfoss PolyPower® A/S headquarters in Nordborg, Denmark [?].

The promising potential of DE actuators, the performance of which is likely to surpass, by means of stress-strain operational ranges, antagonistic pneumatic and electromagnetic actuators in the forthcoming years, cf. Fig. 1.1, has led many scientists to investigate their applicability to miscellaneous disciplines. Indicatively, already in 2003, a multifunctional roll, containing six (6) spring DE actuators, moving by combining bending and axial actuation mechanisms, was presented by SRI International [?, ?]. Later, in 2006, a novel, portable kinematic-free force feedback device, based on miniature spring roll DE actuators, was introduced by Zhang et al. for virtual reality and robotic applications [?].

Yet, it was not until 2008, until the first electroactive polymer core-free actuator was studied in detail by Kovacs et al. in [?]. Subsequently, in 2009, Danfoss PolyPower® A/S introduced their own core-free free-standing tubular push actuator, depicted in Figure 1.2(a), titled InLastor® [?, ?]. Since then, Danfoss PolyPower ® A/S has investigated the applicability of its actuators to other appliances as well, attaining an incremental actuator, a loudspeaker and a radiator thermostat [?, ?, ?]. In 2011, Artificial Muscle Inc. (AMI) [?], a subsidiary of Bayer Material LLC [?], released the ViViTouch™ haptic feedback mophie® pulse, revealing an entirely new market for DE actuators [?].

Besides actuator applications, DEs have lately infiltrated into the sensor market as well, with Danfoss PolyPower® A/S releasing their first unobtrusive and compliant wireless stretch sensor in 2012. StretchSense™ [?], a spin out from the Biomimetics Laboratory at the Auckland Bioengineering Institute,

(a) (b)

Figure 1.2: Illustration of (a) Danfoss PolyPower® A/S push InLastor® actuators with end caps and electrical connections (b) StretchSense™ versatile wireless stretch sensor installed on a human hand.

followed PolyPower's lead by releasing their version of a versatile and soft wireless stretch sensor, illustrated in Figure 1.2(b), in 2013. Although penetration of DEs into the energy generation market has been relatively belated, in regard to the actuator and sensor markets, a relevant state of the art analysis is conducted in the following section, to form the base upon which the scope, objectives and potential scientific contributions of this project will be defined.

1.2 State of the art

The great potential of DE generators was investigated by Koh et al. in [**?**], based on work-conjugate force versus strain and voltage versus charge planes. The latter ones were designed based on the stress-strain curve of the polymer material and all known failures mechanisms of it, i.e. electrical breakdown, electromechanical instability, loss of tension and material rupture. Based on experimental results, Koh et al. determined the maximum energy density of a polyacrylate VHB™ based generator as 1.7 J/g and that of a natural rubber based generator as 1.3 J/g, which are at least an order of magnitude higher than the respective energy of piezoelectric ceramics, electrostrictive polymers and electromagnetic generators [**?**, **?**].

Following Koh's work, several researchers focused on attaining tangible energy harvesting cycles, which could fulfill the predictions of [**?**, **?**]. Until present, three (3) main cycles have been considered; namely the Constant Charge (CC), the Constant Voltage (CV) and the Constant E-field (CE), rigorously analysed,

in terms of their absolute and relative energy gain, by Graf et al. in [**?**]. Furthermore, the parasitic elements contribution on the energy harvesting cycles was, among other limiting factors, presented in [**?**] and [**?**], while in [**?**] the effects imposed, on the energy harvesting cycles performance, by the finite efficiency of the employed power electronic converter were thoroughly investigated.

An experimental documentation of all three (3) fundamental energy harvesting cycles was achieved in [**?**], by coupling a bidirectional non-isolated power electronic converter to a standalone generator installed on a mechanical test rig. Later on, using the same setup, the energy harvesting cycles were experimentally outlined, by means of energy gain, energy harvesting efficiency and energy conversion efficiency [**?**]. Finally, in [**?**], an electromechanical model of a DEAP generator was presented, accounting for both the visco-hyperelastic characteristics of the polymer material as well as the latter one's experimentally determined stretch-capacitance dependence. The model was validated via merely mechanical experiments and electromechanical tests conducted under all three (3) distinct energy harvesting cycles.

Since 2001, when Pelrine et al. presented the fundamentals of DEAP generators, a lot of research has been conducted on identifying potential applications of their technology [**?**,**?**]. Hitherto, exploitation of DEAP generators for energy harvesting purposes has been considered in human-activity-based applications [**?**,**?**,**?**] and wave power infrastructures [**?**,**?**,**?**,**?**,**?**] demonstrating rather promising results. SBM holds the world record in harvested energy per cycle, with 4 J being extracted at 0.7 Hz, via a dual DEAP generator Power Take Off (PTO) unit, in a preliminary test of their patented standing wave tube electro active polymer Wave Energy Converter (WEC) S3 [**?**, **?**].

In other eminent endeavours, Wang et al. harvested energy via an acrylic elastomer, by realizing a charging-while-stretching at a low stretch rate cycle [**?**]. Kaltseis et al. on the other hand, managed to generate electric energy by inflating/deflating a similar acrylic DEAP membrane fixed on a chamber [**?**]. Yet, the largest energy densities documented so far were achieved by Huang and Shian in [**?**, **?**]. More specifically, in [**?**], they accomplished generation of 550 mJ/g, with an energy conversion efficiency equal to 22.1 %, by equi-biaxially stretching an acrylic elastomer, while in [**?**], they increased the energy generation to 780 mJ/g and the energy conversion efficiency to 30 %, by optimizing the selection of the energy-storing capacitor, in an effort to attain as much of the energy-profitable area defined in [**?**, **?**] as possible.

In most of these applications high-voltage relays and/or diodes were used to drive/harvest electric energy to/from the DEAP generators. These relatively simple and reliable passive concepts, allowed the generators to operate close to their maximum E-field strength boosting their energy gain. Howbeit, passive electronics are not only inefficient in terms of energy output and control, but in the mean time they restrict the operation of the DEAP generators to the

CC and/or CV energy harvesting cycles, which are less lucrative, in terms of absolute energy gain, than the CE cycle [**?**]. Besides, their limited degrees of freedom penalize the harvesting cycles' energy gain as the DEAP generator internal E-field remains relatively high even during the generator stretching phase [**?**]. Nevertheless in [**?**], a passive, integrated, self-priming charge pump circuit for miniaturized DEAP generators was proposed, alleviating the need for an external high-voltage direct-current power supply.

For substantially bigger generators, used in WECs, active power electronic converters have been considered as well, as not only do they promise higher energy gains, due to their superior performance in terms of energy efficiency, but they also utilize the DEAP generator energy harvesting cycles more effectively. Indeed, in 2010, Jens et. al introduced the first active power electronic concept, based on a typical bidirectional buck-boost converter, demonstrating energy generation of 26 mJ per cycle [**?**]. Later in [**?**], a similar converter was used to experimentally outline and compare the DEAP generator energy harvesting cycles achieving 256 mJ per cycle. Finally, in [**?**, **?**], a bidirectional tapped-inductor buck-boost converter manifested energy harvesting of 420 mJ per cycle; characterized by an energy density of 2 J per kg of active material.

1.3 Scope and Objectives

The prime scope of the project is to investigate the degree of high-efficient, cost-effective, large-scale, potential applicability of Danfoss PolyPower® A/S DEAP generators to energy harvesting applications. Focus is on abundant natural sources, like wave power, due to the technology's direct energy conversion feature and prominent low-speed performance. Undoubtedly, and as reported in the state of art analysis, the vast capacity of this novel technology may only be harnessed via a pertinent power electronic converter, the proper design of which relies on the deep understanding of the DEAP generator energy harvesting cycles and the polymer material behaviour during each one of them.

Indeed, the necessity for bidirectional energy flow in an energy harvesting cycle, under high step-up and high step-down voltage conversion ratios, accompanied by low-average but relatively high-peak currents, imposes great challenges on the design of the converter; not to mention that the effective operational range of the latter one is usually limited by the lack of commercially-available, high-efficient, high-voltage, low-power switches. To date, tangible power electronic solutions are limited to designs where the specifications focus on rapid charging/discharging times rather than on high-efficient, cost-effective operation, as for example radar modulators, X-ray generators and cathode ray tubes.

Hence, and in order to address all these issues, the main objectives of the PhD project were defined as follows:

- Design and validate an electromechanical model for a DEAP generator.
- Outline and compare the DEAP generator fundamental energy harvesting cycles, i.e CC, CV and CE, based on actual tangible experimental results.
- Optimize the serialization of a finite number of off-the-shelf non-matched non-thermally-coupled power-MOSFETs via a merely passive stacking technique.
- Design, assemble and assess the operation of a novel high-efficient power electronic converter enabling the energy harvesting process of a DEAP generator.

1.4 Scientific contributions

The scientific contributions of the PhD project are strongly correlated with the latter one's main objectives. Indeed, the outcome of the PhD project is:

- A meticulous and precise electromechanical model of a DEAP generator, accounting for both the visco-hyperelastic characteristics of the elastomer, as well as the latter one's stretch-dependent capacitance. Understanding the behaviour of the polymer material, during the steady-state and dynamic intervals of an energy harvesting cycle, is of paramount importance, to ensure operation within its Safe Operation Area (SOA); avoiding failure mechanisms like loss of tension or electrical breakdowns. Such a model, was lacking from the respective literature, with most efforts focusing on DEAP actuators, and thus its acquisition and experimental verification was considered crucial towards the deeper understanding of DEAP generators.
- A rigorous and comprehensive theoretical and experimental overview of the principal energy harvesting cycles of a DEAP generator, i.e. CC, CV and CE. In the past, several articles have demonstrated thorough and extensive analyses of the DEAP generator fundamental energy harvesting cycles, based on averaged theoretical models. Yet, until the commencement of this project it had not be possible to validate the outcome of those models via respective experimental results. In addition, various inquires, as for example the qualitative interaction of the DEAP generator, operating under any energy harvesting cycle, with the respective converter, were never attended.
- A new and simple passive technique for serializing off-the-shelf non-matched power-MOSFETs, towards the establishment of a high-efficient, high-voltage and fast-switching device. Indeed, the lack of akin commercially-available devices seems to limit the efficiency of high-voltage low/medium-power converters, as the semiconductor switches which are rated to block voltages in

the range of few kilovolts are in the same time rated for several hundred amperes, rendering their use in such converters inefficient. Alternatively, efficient stacking of switches is achieved via relatively expensive, complex, active techniques, which typically involve one or more feedback signals.

- A novel DC-DC power electronic converter, facilitating high-efficient bidirectional energy flow under high step-up and high step-down voltage conversion ratios, accompanied by low-average but relatively high-peak currents. Apart from enabling the DEAP generator energy harvesting process, the aforementioned converter provides valuable input to various power electronic disciplines; limited today by the lack of high-efficient, high-voltage devices.

1.5 Outline

The dissertation is divided into six (6) chapters and an appendix. Most chapters are based on a - at least - respective article and contribute with an extended summary of it, highlighting the most essential scientific findings. All papers are then annexed in the appendix and the outline of the dissertation is as follows:

CHAPTER 1 presents the scientific background of the PhD project, along with a thorough state of the art analysis on the up-to-date conducted research on DEAP generators. In addition, the fundamental objectives of the PhD project are formulated and its most essential scientific contributions are highlighted.

CHAPTER 2 delivers an introduction to the DEAP technology as well as a first insight into the DEAP generator fundamental energy harvesting cycles. More, an electromechanical model for a DEAP generator is presented, tuned via merely mechanical tests and assessed based on actual experimental data.

CHAPTER 3 introduces the first demonstrator, i.e. demo#0, build to facilitate the conduction of experimental work on DEAP generators. The latter one's energy harvesting cycles are experimentally outlined by means of energy gain, energy harvesting efficiency and energy conversion efficiency for the first time.

CHAPTER 4 describes the second demonstrator, i.e. demo#1, designed to enable the out-of-phase co-cycling of several DEAP generators, driven to high E-field strength values by a power electronic converter prototype; based on a string of three (3) off-the-shelf non-matched non-thermally-coupled MOSFETs.

CHAPTER 5 on the other hand, outlines the final demonstrator, i.e. demo#2, assembled to scale-up the energy harvesting system, by employing voluminous DEAP generators, driven to high E-field strengths via a pertinent tapped-inductor buck-boost converter; based on the revised gate balancing core technique.

CHAPTER 6 concludes the PhD dissertation, summarizing the project's main conclusions, while including a DEAP technology judicious perspective analysis.

1.6 List of Publications

Parts of the work presented in this dissertation have also been published in other sources. Indeed, in chronological order:

1. Emmanouil Dimopoulos, Ionut Trintis, Stig Munk-Nielsen, 'Energy Harvesting Cycles of Dielectric ElectroActive Polymer Generators', *38th Annual Conference on IEEE Industrial Electronics Society (IECON 2012)*, Montreal, Canada, 2012.

2. Emmanouil Dimopoulos, Ionut Trintis, Stig Munk-Nielsen, 'Comparison of the dielectric electroactive polymer generator energy harvesting cycles', *Proceedings of the SPIE Smart Structures and Materials / Nondestructive Evaluation and Health Monitoring: ElectroActive Polymer Actuators and Devices (EAPAD 2013)*, San Diego CA, USA, 2013.

3. Ionut Trintis, Emmanouil Dimopoulos, Stig Munk-Nielsen, 'Simple DCM or CCM analog peak current controller for HV capacitor charge-discharge applications', *15th European Conference on Power Electronics and Applications (EPE 2013)*, Lille, France, 2013.

4. Emmanouil Dimopoulos, Ionut Trintis, Stig Munk-Nielsen, Björn Rechenbach, Morten Willatzen, Benny Lassen, 'An Electromechanical Model of a Dielectric ElectroActive Polymer Generator', *15th European Conference on Power Electronics and Applications (EPE 2013)*, Lille, France, 2013.

5. Emmanouil Dimopoulos, Stig Munk-Nielsen, 'Serializing off-the-shelf MOSFETs by Magnetically Coupling Their Gate Electrodes', *15th European Conference on Power Electronics and Applications (EPE 2013)*, Lille, France, 2013.

6. Emmanouil Dimopoulos, Stig Munk-Nielsen, 'Scaling the serialization of MOSFETs by Magnetically Coupling Their Gate Electrodes', *Energy Conversion Congress and Exposition (ECCE 2013)*, Denver CO, USA, 2013.

7. Emmanouil Dimopoulos, Stig Munk-Nielsen, 'A Tapped-Inductor Buck-Boost Converter for a Dielectric ElectroActive Polymer Generator', *Applied Power Electronics Conference and Exposition (APEC 2014)*, Dallas TX, USA, 2014.

8. Emmanouil Dimopoulos, Stig Munk-Nielsen, 'A tapped-inductor buck-boost converter for a multi-DEAP generator energy harvesting system', *Proceedings of the SPIE Smart Structures and Materials / Nondestructive Evaluation and Health Monitoring: ElectroActive Polymer Actuators and Devices (EAPAD 2014)*, San Diego CA, USA, 2014.

9. Tahir Lağap, Emmanouil Dimopoulos, Stig Munk-Nielsen, 'An RCDD Snubber for a Bidirectional Flyback Converter', *17th European Conference on Power Electronics and Applications (EPE 2015)*, Geneva, Switzerland, Sep. 2015, accepted.

This page is intentionally left blank

Chapter 2

The DEAP Technology

2.1 Introduction

Prior to 2008, ElectroActive Polymer (EAP) films were produced either via common small-scale fabrication techniques like spin-coating, spray-coating and casting, or by employing pre-strained off-the-shelf materials, typically susceptible to dielectric impurities, like the VHB™ acrylic elastomer by 3M [**?**]. Large-scale industrial production of EAP films was, at the time, impractical, as it called for automated handling, at nearly zero strain, of a very thin, flexible and stretchable elastomer, during a highly stringent manufacturing process.

Admittedly, among the most compelling challenges towards the acquisition of an industrialized manufacturing process for large-scale EAP films, laid the need to design compliant electrodes, able to cope with moderate actuation forces and large strains for a plausible number of cycles, without acute fracturing. Indeed, numerous different solutions were investigated including greases, conductive fibers, carbon nanotubes, as well as silicones impregnated with conductive particles. Micro-machining and screen-printing industrial techniques were successfully practised to apply these electrodes in rather small-scale designs.

Yet, in 2008, Danfoss PolyPower® A/S revolutionized the field of EAPs, by establishing a pilot, unique and scalable roll-to-roll manufacturing process, capable of fabricating kilometres of metallized DEAP material per week, inspired by the web conveying industry [**?**]. In parallel, Danfoss PolyPower® A/S presented their patented compliant electrodes, known as '*smart metallic compliant electrodes*', which enabled the commercialization of PolyPower® film and large-scale actuators [**?**, **?**, **?**]. Today, as reported in [**?**, **?**], the manufacturing process can be classified into two stages; namely the DEAP single-layer film universal coating stage and the application-specific transducer assembling one.

2.2 Electromechanical Model

DEAP single-layer films, fabricated by Danfoss PolyPower® A/S, consist of a thin dielectric elastomer (silicone PDMS) sandwiched between a flat-back surface and a micro-embossed, corrugated front surface, upon which a highly conductive silver electrode has been deposited, determining the compliant and almost-stiff planar directions of the film, cf. Fig. 2.1 (a). Typically, two elastomer films are laminated, in an either back-to-back configuration as seen in Fig. 2.1 (b) or in a front-to-back configuration, to form a single DEAP sheet.

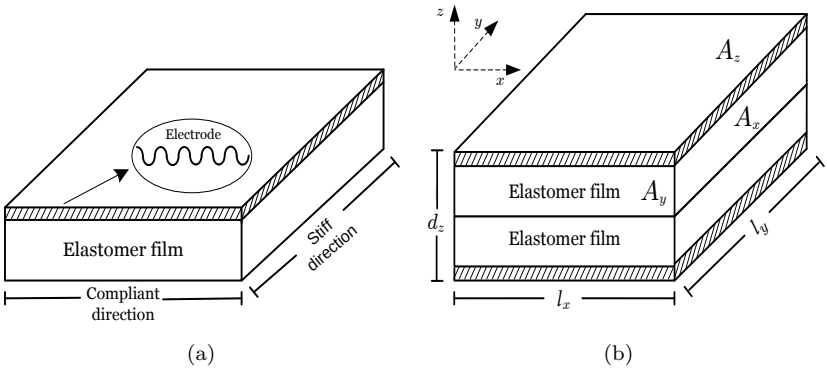

Figure 2.1: Structure of (a) the DEAP single-layer film (b) two laminated elastomer films forming a single DEAP sheet in a back-to-back configuration.

As aforementioned, the transducer assembling stage is an application-specific process and thus no general guidelines can be derived to describe its platform. Nevertheless, in the following sections, a cube-shaped DEAP generator is presented, alongside with an electromechanical model explicitly designed for it. The model parameters are identified via merely mechanical experiments and subsequently the model is verified under all distinct energy harvesting cycles.

2.2.1 DEAP generator description

The dimensions of a DEAP sheet are $A_x = l_y d_z$, $A_y = d_z l_x$ and $A_z = l_x l_y$, where l_x, l_y and d_z denote the sheet length, width and thickness respectively. The single sheet can be modelled as a parallel plate capacitor with capacitance

$$C_{\text{sheet}} = \varepsilon_0 \varepsilon_{\text{rel}} \frac{A_z}{d_z}, \tag{2.1}$$

where ε_0 and ε_{rel} reflect the vacuum and the elastomer relative permittivities. The DEAP generator, on the other hand, can be considered as the combination

of n parallel-connected single DEAP sheets and hence its capacitance is

$$C = nC_{\text{sheet}}. \tag{2.2}$$

Upon stretching, the measures of a single sheet alter according to

$$l_x = \lambda_x l_x^{(0)}, \quad l_y = \lambda_y l_y^{(0)}, \quad d_z = \lambda_z d_z^{(0)}, \tag{2.3}$$

where λ_x, λ_y and λ_z are the stretches in the three coordinate directions and $l_x^{(0)}$, $l_y^{(0)}$ and $d_z^{(0)}$ correspond to the respective measures of the undeformed sheet. Thus, the DEAP generator capacitance can be rewritten as

$$C = C^{(0)} \frac{\lambda_x \lambda_y}{\lambda_z}, \quad C^{(0)} = n\varepsilon_0 \varepsilon_{\text{rel}} \frac{l_x^{(0)} l_y^{(0)}}{d_z^{(0)}}, \tag{2.4}$$

where $C^{(0)}$ denotes the capacitance of the undeformed DEAP generator. The dependence of a DEAP generator capacitance on the stretch λ_x[1] has been studied by Danfoss PolyPower® A/S, resulting in the following empirical relation

$$C = C_{\text{exp}}^{(0)} \lambda_x^{\kappa}, \quad \kappa \in [1, 2], \tag{2.5}$$

where $C_{\text{exp}}^{(0)}$ denotes the empirical value of the undeformed DEAP generator capacitance. The actual value of the exponent κ, expressing the degree of anisotropy, is influenced by, among other factors, the stiff silver electrodes and the mechanical boundary conditions that the DEAP sheets are subjected to. Biaxial conditions, which ideally means that the sheets can elongate freely in both the x- and y- directions, correspond to $\kappa = 1$. Whereas $\kappa = 2$ implies that any elongation in the y-direction is prohibited by the stiff silver electrodes. Consistency of (2.4) and (2.5) requires that

$$C^{(0)} = C_{\text{exp}}^{(0)} \quad \text{and} \quad \frac{\lambda_x \lambda_y}{\lambda_z} = \lambda_x^{\kappa}. \tag{2.6}$$

Furthermore, the volume of the dielectric elastomer can be assumed, within reasonable approximation, to be constant [**?**], implying that

$$\lambda_x \lambda_y \lambda_z = 1. \tag{2.7}$$

During equi-biaxial loading the capacitance of the DEAP generator alters in proportion to the fourth power of the stretch. In addition, equi-biaxial loading of the polymer sheets results in relatively uniform deformations, thus preventing local stress accumulation and/or E-field concentration [**?**]. Yet, the need for pliable but also scalable electrodes penalizes the attractiveness of such designs.

[1] The x-direction is the direction along which the sheets are stretched in the experiments conducted within the framework of this PhD project.

2.2.2 Experimental setup

The experimental setup assembled to validate the electromechanical model was fundamentally a prime version of demo#0; thoroughly presented in Chapter 3. Concisely, the mechanical test rig consisted of an induction motor, coupled to the DEAP generator via a circular disc and a configurable arm, which set the pre-stretch of the DEAP sheets. To acquire real-time displacement and force data a Solarton Metrology® Linear Variable Differential Transformer (LVDT) (model S-Series AS/100/G) was installed in parallel with the DEAP generator, while mounted on top of the latter one laid a Tedea® load cell (model 615).

A typical non-isolated buck-boost converter, also presented in Chapter 3, was employed to enable the DEAP generator and to realize all energy harvesting cycles. The buck and boost functions of the converter were triggered based upon the real-time position feedback provided by the LVDT and the former one's main control loop was DEAP-voltage-based. Synchronized acquisition of displacement, force and voltage data was achieved via a National Instruments CompactDAQ (NI-cDAQ™) 9178 chassis and a measuring bundle installed on it.

2.2.3 Viscohyperelastic model

A DEAP generator exhibits viscoelastic properties and is, in practical applications, stretched beyond stretches where a linear material model would apply. Hence, a visco-hyperelastic model is needed for its description. The Zener model, a single elastic spring in parallel with N Maxwell elements is chosen here, cf. Fig. 2.2. The elastic energy density w of the DEAP generator is the sum of the elastic energy densities stored in the springs, i.e. Ψ for the standalone spring and $\Phi^{(j)}$ for each of the N springs,

$$w = \Psi + \sum_{j=1}^{N} \Phi^{(j)}. \tag{2.8}$$

Furthermore, it is assumed that the elastic energy density of each spring depends only on its stretch state. The stretches of the standalone spring on the coordinate axes are λ_x, λ_y and λ_z. The stretches of the spring in the j-th Maxwell element are denoted by ${\lambda_\mathrm{e}^{(j)}}_i$, where $i = x, y, z$ and $j = 1, \ldots, N$. According to the frequently used deformation tensor decomposition it is

$$\lambda_i = {\lambda_\mathrm{e}^{(j)}}_i {\lambda_\mathrm{v}^{(j)}}_i \quad \Leftrightarrow \quad {\lambda_\mathrm{e}^{(j)}}_i = \frac{\lambda_i}{{\lambda_\mathrm{v}^{(j)}}_i}, \tag{2.9}$$

where ${\lambda_\mathrm{v}^{(j)}}_i$ are the stretches of the j-th dashpot. All ${\lambda_\mathrm{v}^{(j)}}_i$ terms are treated as internal variables and it is further assumed that all springs and dashpots

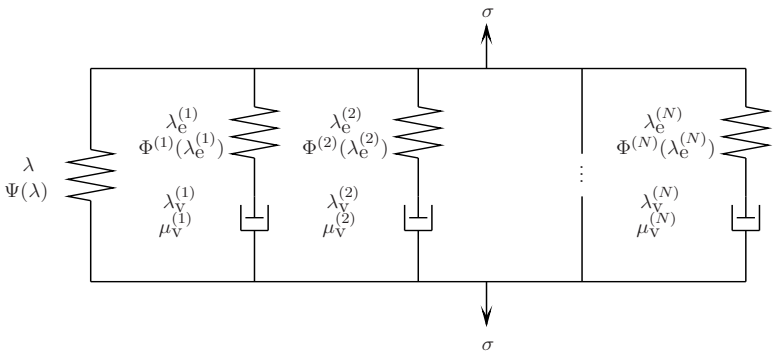

Figure 2.2: Zener model spring-dashpot diagram of visco-hyperelasticity.

undergo isochoric processes as well as an analogue process to (2.6)

$$\lambda_{\mathrm{e}}^{(j)}{}_x \lambda_{\mathrm{e}}^{(j)}{}_y \lambda_{\mathrm{e}}^{(j)}{}_z = 1, \tag{2.10}$$

$$\frac{\lambda_{\mathrm{e}}^{(j)}{}_x \lambda_{\mathrm{e}}^{(j)}{}_y}{\lambda_{\mathrm{e}}^{(j)}{}_z} = \lambda_{\mathrm{e}}^{(j)\,\kappa}{}_x. \tag{2.11}$$

The elastic energy density of the standalone spring constitutes of the energy density caused by stretching/compressing the DEAP sheets Ψ_{sc}, the dielectric energy density stored in the DEAP generator Ψ_{diel} and finally the term Ψ_{con}, which satisfies the constraints (2.6) and (2.7)

$$\Psi = \Psi_{\mathrm{sc}} + \Psi_{\mathrm{diel}} + \Psi_{\mathrm{con}}. \tag{2.12}$$

A Mooney-Rivlin model is employed for Ψ_{sc}

$$\Psi_{\mathrm{sc}} = C_{10}\left(\lambda_x^2 + \lambda_y^2 + \lambda_z^2 - 3\right) + C_{01}\left(\lambda_y^2\lambda_z^2 + \lambda_z^2\lambda_x^2 + \lambda_x^2\lambda_y^2 - 3\right) \tag{2.13}$$

where C_{10} and C_{01} denote the Mooney-Rivlin model material constants. The dielectric energy density stored in the DEAP generator is given by [**?**]

$$\Psi_{\mathrm{diel}} = -\frac{1}{2}\varepsilon_0\varepsilon_{\mathrm{rel}}\left(\frac{V_c}{d_z}\right)^2, \tag{2.14}$$

where V_c is the voltage applied across the DEAP electrodes. Furthermore, it is

$$\Psi_{\mathrm{con}} = p^{(0)}(\lambda_x\lambda_y\lambda_z - 1) + q^{(0)}\left(\frac{\lambda_x\lambda_y}{\lambda_z} - \lambda_x^{\kappa}\right), \tag{2.15}$$

where $p^{(0)}$ and $q^{(0)}$ are Lagrange multipliers which will be eliminated later on. Analogously, the elastic energy density of each of the N springs comprises of two energy density quantities; one reflecting the stretching/compressing of the

j-th Maxwell element spring, $\Phi_{\mathrm{sc}}^{(j)}$, and another one satisfying the constraints (2.10) and (2.11), $\Phi_{\mathrm{con}}^{(j)}$

$$\Phi^{(j)} = \Phi_{\mathrm{sc}}^{(j)} + \Phi_{\mathrm{con}}^{(j)}. \tag{2.16}$$

For $\Phi_{\mathrm{sc}}^{(j)}$, a Neo-Hookean model is employed

$$\Phi_{\mathrm{sc}}^{(j)} = \frac{1}{2}\mu_{\mathrm{e}}^{(j)} \left({\lambda_{\mathrm{e}}^{(j)}}_x^2 + {\lambda_{\mathrm{e}}^{(j)}}_y^2 + {\lambda_{\mathrm{e}}^{(j)}}_z^2 - 3 \right). \tag{2.17}$$

where $\mu_{\mathrm{e}}^{(j)}$ denotes the shear modulus of the viscoelastic spring in the j-th Maxwell element. Similar to (2.15), for $\Phi_{\mathrm{con}}^{(j)}$ it is

$$\Phi_{\mathrm{con}}^{(j)} = p^{(j)} \left({\lambda_{\mathrm{e}}^{(j)}}_x {\lambda_{\mathrm{e}}^{(j)}}_y {\lambda_{\mathrm{e}}^{(j)}}_z - 1 \right) + q^{(j)} \left(\frac{{\lambda_{\mathrm{e}}^{(j)}}_x {\lambda_{\mathrm{e}}^{(j)}}_y}{{\lambda_{\mathrm{e}}^{(j)}}_z} - {\lambda_{\mathrm{e}}^{(j)}}_x^{\kappa} \right), \tag{2.18}$$

where, again, $p^{(j)}$ and $q^{(j)}$ are Lagrange multipliers which will be eliminated later on.

2.2.4 Electromechanical coupling

Newton's second law implies

$$l_y^{(0)} l_z^{(0)} \frac{\partial w}{\partial \lambda_x} = F = \sigma \frac{l_y^{(0)} l_z^{(0)}}{\lambda_x}, \qquad \frac{\partial w}{\partial \lambda_y} = 0, \qquad \frac{\partial w}{\partial \lambda_z} = 0, \tag{2.19}$$

where F is the force measured in experiments, σ is the corresponding stress and $l_z^{(0)}$ is the undeformed thickness of the entire DEAP generator given by

$$l_z^{(0)} = n d_z^{(0)}. \tag{2.20}$$

The inertia of the DEAP has been neglected, as it has nearly no influence on the results, and Newton's second law is supplemented, due to the viscous behaviour of the DEAP generator, by the second law of thermodynamics. Undeniably, the viscoelastically dissipated power has to be positive

$$\frac{{\dot{\lambda}_{\mathrm{v}}^{(j)}}_i}{{\lambda_{\mathrm{v}}^{(j)}}_i} \lambda_i \frac{\partial \Phi^{(j)}}{\partial \lambda_i} \geq 0. \tag{2.21}$$

The following relation is imposed

$$\frac{{\dot{\lambda}_{\mathrm{v}}^{(j)}}_i}{{\lambda_{\mathrm{v}}^{(j)}}_i} = 2\mu_{\mathrm{v}}^{(j)} \lambda_i \frac{\partial \Phi^{(j)}}{\partial \lambda_i} \tag{2.22}$$

where the viscous parameter $\mu_{\mathrm{v}}^{(j)}$ of the j-th Maxwell element dashpot is considered positive and $\dot{\lambda}_{\mathrm{v}}^{(j)}{}_i$ denotes the time derivative of the j-dashpot stretches.

Elimination of the Lagrange multipliers yields

$$\sigma = -\sigma_{\mathrm{diel}} + \sigma_x + \left(\frac{\kappa}{2} - 1\right)\sigma_y - \frac{\kappa}{2}\sigma_z + \sum_{j=1}^{N}\left(\sigma_{\mathrm{e}}^{(j)}{}_x + \left(\frac{\kappa}{2} - 1\right)\sigma_{\mathrm{e}}^{(j)}{}_y - \frac{\kappa}{2}\sigma_{\mathrm{e}}^{(j)}{}_z\right), \tag{2.23}$$

$$\sigma_i = \lambda_i \frac{\partial \Psi}{\partial \lambda_i}, \quad \sigma_{\mathrm{e}}^{(j)}{}_i = \lambda_i \frac{\partial \Phi^{(j)}}{\partial \lambda_i}, \quad \sigma_{\mathrm{diel}} = \frac{\kappa}{2}\varepsilon_{\mathrm{rel}}\varepsilon_0 \lambda_x^{\kappa}\left(\frac{V_c}{d_z^{(0)}}\right)^2, \tag{2.24}$$

$$\frac{\dot{\lambda}_{\mathrm{v}}^{(j)}{}_x}{\lambda_{\mathrm{v}}^{(j)}{}_x} = 2\mu_{\mathrm{v}}^{(j)}\sigma_{\mathrm{e}}^{(j)}{}_x, \tag{2.25}$$

where σ_i denotes the stresses on the coordinate axes, $\sigma_{\mathrm{e}}^{(j)}{}_i$ reflects the stress of the spring in the j-th Maxwell element and finally σ_{diel} corresponds to the dielectric stress.

2.2.5 DEAP generator electrical equivalent

The electrical impedance of a DEAP generator can be modelled by the corresponding equivalent circuit diagram illustrated in Fig. 2.3. A serial resistance R_{serial}, reflecting the resistance of the electrodes and the driving circuit wiring assembly, is connected directly to the DEAP capacitance C [**?**]. More, a shunt resistance R_{parallel}, accounting for the leakage current of the DEAP generator, is also included in the schematic. Table 2.1 outlines the DEAP generator parameters where both resistances have been considered stretch-independent.

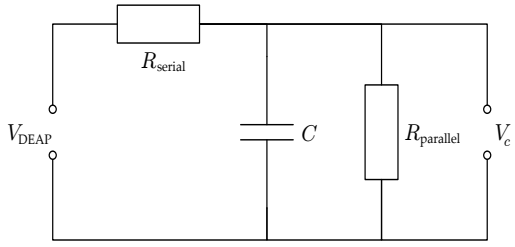

Figure 2.3: DEAP generator electrical equivalent.

Table 2.1: DEAP generator parameters.

Parameter	Value
κ	1.43
$\varepsilon_{\mathrm{rel}}$	3.1
$C^{(0)}$	1 uF
R_{serial}	4 Ohm
R_{parallel}	10 GOhm

Kirchhoff's circuit laws are applied, to formulate the governing equation of the voltage V_c across the DEAP electrodes in terms of the voltage V_{DEAP} applied across the equivalent circuit, resulting in

$$\frac{1}{R_{\mathrm{serial}}C^{(0)}}V_{\mathrm{DEAP}} = \left(\frac{1}{\tau_e} + \kappa\lambda_x^{\kappa-1}\dot{\lambda}_x\right)V_c + \lambda_x^{\kappa}\dot{V}_c, \tag{2.26}$$

where τ_e reflects the time constant of the circuit

$$\tau_e = \frac{R_{\mathrm{parallel}}R_{\mathrm{serial}}C^{(0)}}{R_{\mathrm{parallel}} + R_{\mathrm{serial}}}, \tag{2.27}$$

and $\dot{\lambda}_x$ and $\dot{V}_c$ denote the time derivative of the stretch in x-direction and voltage across the DEAP electrodes respectively.

2.3 Energy Harvesting Cycles

Allowing a charged pre-stretched DEAP generator to contract inevitably leads to an increase of its electric potential energy. Indeed, assuming an isotropic generator, as the area of the electrodes decreases, repelling charges are densely distributed, while as the elastomer thickness increases, attracting charges are remotely equilibrated, working oppositely to the electrostatic forces, thus converting mechanical energy into electrical energy. Differentiating (2.2)

$$\dot{C} = \frac{n\varepsilon}{d_z}\dot{A}_z - \frac{n\varepsilon A_z}{d_z^2}\dot{d}_z, \tag{2.28}$$

where ε is the elastomer permittivity, i.e. $\varepsilon = \varepsilon_0\varepsilon_{\mathrm{rel}}$. During the relaxation phase, the capacitance of the DEAP generator decreases, cf. (2.1). Neglecting leakage losses, the electrical charge of the generator may be considered constant

$$Q = CV_c \quad \text{and} \quad \dot{Q} = 0 \tag{2.29}$$

and hence the voltage across the generator electrodes increases equivalently. The analysis of the distinct energy harvesting cycles will be based upon the rate of change of the generator capacitance $\dot{C}$, voltage $\dot{V}_c$, electric field strength $\dot{E}$ and electric potential energy $\dot{U}_e$, as functions of the capacitor area rate of change $\dot{A}_z$.

Assuming an isochoric deformation, cf. (2.7),

$$V_{\mathrm{ol}} = nA_zd_z \quad \text{where} \quad \dot{V}_{\mathrm{ol}} = 0 \tag{2.30}$$

$$A_z\dot{d}_z = -d_z\dot{A}_z, \tag{2.31}$$

where V_{ol} is the elastomer volume. Equation (2.28) can now be simplified to

$$\dot{C} = 2\frac{n\varepsilon}{d_z}\dot{A}_z. \tag{2.32}$$

Respectively, the voltage formula can be derived as,

$$V_c = \frac{Qd_z}{n\varepsilon A_z}, \tag{2.33}$$

$$\dot{V}_c = \frac{Q}{n\varepsilon A_z}\dot{d}_z - \frac{Qd_z}{n\varepsilon A_z^2}\dot{A}_z, \tag{2.34}$$

$$\dot{V}_c = -2\frac{Qd_z}{n\varepsilon A_z^2}\dot{A}_z. \tag{2.35}$$

Accordingly, the electric field of a capacitor is defined as the ratio of the voltage across its electrodes to its thickness

$$E = \frac{V_c}{d_z}, \tag{2.36}$$

$$\dot{E} = \frac{1}{d_z}\dot{V}_c - \frac{V_c}{d_z^2}\dot{d}_z. \tag{2.37}$$

Substituting (2.31) and (2.35) into (2.37) leads to the simplified equation

$$\dot{E} = -\frac{V_c}{A_z d_z}\dot{A}_z. \tag{2.38}$$

Finally, the desired relation between the electric potential energy of the generator and its area rate of change can be attained by multiplying the electrostatic field energy density

$$u_E = \frac{1}{2}\varepsilon E^2, \tag{2.39}$$

with the generator volume. Indeed,

$$U_e = \frac{1}{2}\varepsilon V_{\text{ol}} E^2, \tag{2.40}$$

$$\dot{U}_e = \varepsilon V_{\text{ol}} E\dot{E}, \tag{2.41}$$

$$\dot{U}_e = -n\varepsilon E V_c \dot{A}_z. \tag{2.42}$$

Equations (2.32), (2.35), (2.38) and (2.42) can now be utilized to thoroughly unfold all aspects of the CC, CV and CE energy harvesting cycles. Evidently, a similar procedure can generate the respective equations for the capacitance $\dot{C}$, voltage $\dot{V}_c$, electric field strength $\dot{E}$ and electric potential energy $\dot{U}_e$ rates of change, as functions of the sheet thickness rate of change $\dot{d}_z$, instead of $\dot{A}_z$.

2.3.1 Constant Charge

The fundamental energy harvesting cycle, i.e. CC, depicted in Fig. 2.4, consists of four (4) transitions commencing/ending from/to point one (1); progressing in an ascending order. Assuming that a non-isolated power electronic converter has been employed to enable the DEAP generator and that the polymer sheets are pre-stretched, as this was shown to enhance their performance [**?**], neither the E-field strength, and thus the electric potential energy, nor the stretch, and thus the mechanical potential energy, of the material are zero at point one (1).

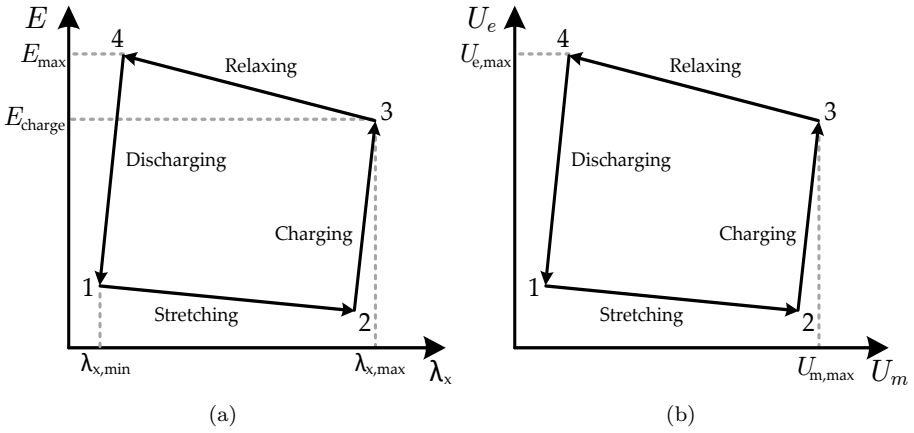

Figure 2.4: DEAP generator (a) E-field strength versus stretch (b) electric potential energy versus mechanical potential energy during a CC cycle.

The $\lambda_{\mathrm{x,min}}$ term denotes the amount of pre-stretch applied on the DEAP sheets, whereas E_{charge} reflects the boost function targeted E-field strength value. Notations $\lambda_{\mathrm{x,max}}$ and E_{max} on the other hand, correspond to the maximum applied stretch and maximum attainable E-field strength of the DEAP generator during the energy harvesting cycle. Accordingly, notations $U_{e,\mathrm{max}}$ and $U_{m,\mathrm{max}}$ reflect the DEAP maximum attainable electric potential energy and DEAP maximum attainable mechanical potential energy during the energy harvesting cycle.

Transition 1 $\rightarrowtail$ 2

Initially, an external energy source imposes stress on the electrically isolated DEAP generator. The polymer sheets elongate along the compliant direction, thus expanding in area, while converting a portion of their electric potential energy into mechanical potential energy. According to (2.32) the generator

capacitance increases, but its voltage (2.35), E-field strength (2.38) and electric potential energy (2.42) are all diminishing, as advancing towards point two (2).

Transition 2 $\rightarrowtail$ 3

At point two (2) a power electronic converter gets coupled to the DEAP generator boosting the electric potential difference across the latter one's electrodes. Consequently, the internal E-field of the polymer sheets increases and so do the compressing electrostatic forces, actuating the elastomer. As the cycle progresses towards point three (3) the polymer sheets will either experience a relative infinitesimal elongation or, in case their mechanical state is fixed, a reduction in the applied force necessary to retain them stretched at point (2).

Transition 3 $\rightarrowtail$ 4

When point three (3) is reached, the power electronic converter is decoupled from the DEAP generator and the applied strain is gradually reduced. The electrically isolated polymer sheets relax, contracting along the compliant direction, thus shrinking in area, converting a portion of their mechanical potential energy into electric potential energy. According to (2.32) the generator capacitance decreases, but its voltage (2.35), E-field strength (2.38) and electric potential energy (2.42) are all increasing, as advancing towards point four (4).

Transition 4 $\rightarrowtail$ 1

Lastly, at point four (4), the power electronic converter is re-coupled to the DEAP generator bucking the electric potential difference across the latter one's electrodes; harvesting the excess electric potential energy of it. Ergo, the internal E-field of the polymer sheets decreases and so do the compressing electrostatic forces actuating the elastomer. As the cycle progresses towards point one (1) the polymer sheets will either experience a relative infinitesimal contraction or, in case their mechanical state is fixed, an escalation in the applied force.

2.3.2 Constant Voltage

In a CV energy harvesting cycle the power electronic converter is not decoupled from the DEAP generator throughout the latter one's transition between points three (3) and four (4). Indeed, and as illustrated in Fig. 2.5(a) the converter ensures that during the generator relaxation phase the voltage across its electrodes does not exceed a predefined hysteresis band, i.e. $V_c \in [V_{\min}, V_{\max}]$.

2.3.3 Constant E-field

Similarly, in a CE energy harvesting cycle the power electronic converter maintains the DEAP generator internal E-field strength within a pre-defined hysteresis band i.e. $E \in [E_{\min}, E_{\max}]$, while the former one transits from point three (3) to point four (4), cf. Fig. 2.5(b). In practical CV and CE cycles E_{charge} may coincide with $V_{\min}$ and $E_{\min}$ to optimize the energy transfer within them.

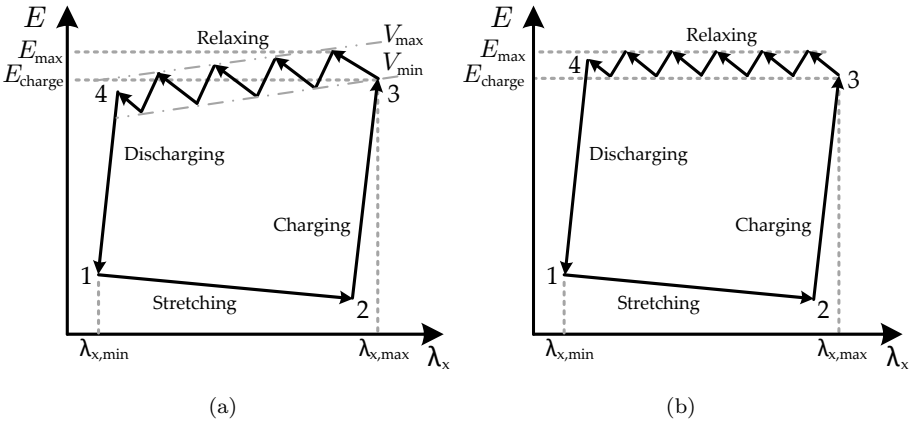

Figure 2.5: DEAP generator E-field strength versus stretch during a (a) CV (b) CE cycle.

Among the three (3) principal energy harvesting cycles the CC one was shown to offer the highest relative energy gain, expressing the ratio between the absolute energy gain and the energy fed into the DEAP generator at point three (3). The CV cycle, on the other hand, having comparable performance with CC in terms of absolute energy gain, demonstrates the least relative energy gain, but with direct control over the voltage swings of the DEAP generator. Finally, the CE energy harvesting cycle promises the highest absolute energy gain followed by an indirect control over the voltage swings of the DEAP generator [**?**, **?**].

2.4 Model verification

Prior to assessing the model performance during each of the energy harvesting cycles, by contrasting the DEAP generator predicted behaviour with the actual documented one, the mechanical parameters of the former one, in the examined frequencies, need to be experimentally identified via merely mechanical tests.

2.4.1 Identification of model parameters

The DEAP generator was subjected to a sinusoidal-like stretch. Synchronized data of force and displacement were acquired for various frequencies between 0.125 Hz and 1 Hz and the latter ones were used to extrapolate the DEAP generator stretch state. The expression

$$\lambda_x(t) = \lambda_A \sin(2\pi f t + \varphi) + \lambda_B \tag{2.43}$$

was then fitted to the extrapolated data, in order to determine the parameters λ_A, λ_B, f and φ corresponding to the stretch amplitude, bias, cycling frequency and phase respectively.

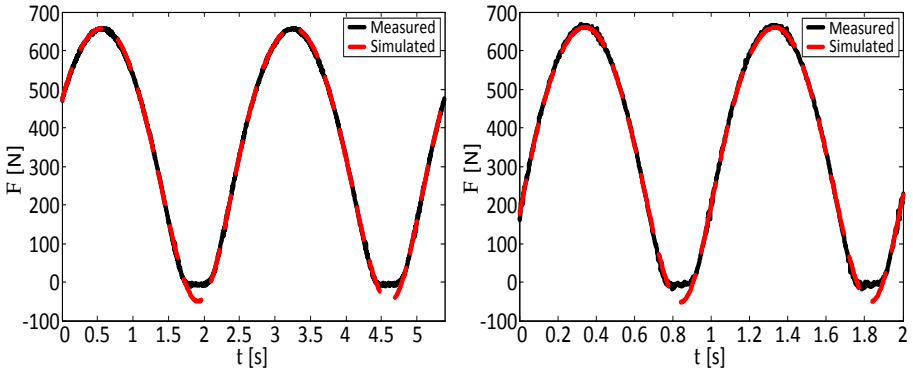

(a) (b)

Figure 2.6: Juxtaposition of the measured force and the model predicted one during a merely mechanical experiment at a (a) $f = 0.37$ Hz and (b) $f = 1.01$ Hz cycling frequency.

The visco-hyperelastic model predicted forces, at the exact time instances where experimental data were acquired, were juxtaposed to the measured forces. In total three (3) different models were employed. The first two (2), containing one ($N = 1$) and two ($N = 2$) Maxwell elements respectively, were characterized by constant damping parameters $\mu_{\mathrm{v}}^{(j)}$, while the third model, containing one ($N = 1$) Maxwell element, was characterized by a stretch and stretch rate dependent damping parameter given by [**?**]

$$\mu_{\mathrm{v}}^{(1)} = \frac{\xi_{\mathrm{v}}^{(1)} \sqrt{\left(\frac{\dot{\lambda}_x}{\lambda_x}\right)^2 + \left(\frac{\dot{\lambda}_y}{\lambda_y}\right)^2 + \left(\frac{\dot{\lambda}_z}{\lambda_z}\right)^2} + \frac{1}{\tau_{\mathrm{v}}^{(1)}}}{\sqrt{\lambda_x^4 + \lambda_y^4 + \lambda_z^4}}, \tag{2.44}$$

where $\xi_{\mathrm{v}}^{(1)}$ models the single dashpot damping constant rate dependency and $\tau_{\mathrm{v}}^{(1)}$ denotes its time constant. As seen in Fig. 2.6, the latter model, with

viscoelastic parameters $C_{10} = 5.33$ kPa, $C_{01} = 12$ kPa, $\mu_e^{(1)} = 95.8$ kPa, $\xi_v^{(1)} = 0.77$ Pa and $\tau_v^{(1)} = 1230$ Pas, demonstrated a nonpareil behaviour over the entire examined frequency range; prevailing over the other models. MATLAB® Nelder-Mead algorithm was deployed for the sake of comparison using a quadratic error function. Yet, all time instances where a negative force was measured were neglected, as the DEAP generator buckled instead of being further compressed under large negative force, due to its relatively low thickness compared to its length. Indeed, and as indicated in Figs. 2.6(a) and 2.6(b), the measured force, while the DEAP generator was at close proximity to its pre-stretched state, saturated around -10 N under all examined cycling frequencies.

2.4.2 Experimental results

In order to validate the electromechanical coupling of the proposed model, equation (2.26), modelling the electrical interaction between the DEAP generator and the DC-DC converter, and equations (2.23) - (2.25), modelling the electromechanical response of the DEAP generator, were included in a PLECS® model of the experimental setup. Experiments under all three (3) distinct energy harvesting cycles of a DEAP generator were conducted and the predicted forces were compared with the actual measured ones, during both static and transient charging/discharging intervals. In all experiments the DEAP generator was cyclicly deformed at a frequency of 0.3 Hz and a delta-strain of 40 %.

Table 2.2 illustrates the converter control settings during the energy harvesting cycles realization. The 'Boost' and 'Buck' columns indicate the buck-boost converter main control parameter at points two (2) and four (4) respectively.

Table 2.2: Converter control settings during the energy harvesting cycles realization.

Cycle	Boost	Buck	Hysteresis Band
CC	900 V	400 V	900 V - 1300 V
CV	900 V	400 V	950 V - 1000 V
CE	9 V/um	3 V/um	9.5 V/um - 10 V/um

The 'Hysteresis Band' column on the other side, indicates the variation of the control parameter during the relaxation phase of the DEAP generator. Indicatively, during a CC cycle the voltage of the DEAP generator was boosted up to 900 V at point two (2), reaching 1300 V before being bucked down to 400 V at the end of the relaxation phase. Contrary, during a CE cycle, the E-field strength of the DEAP generator was boosted up to 9 V/um at point two (2) and was afterwards sustained between 9.5 V/um and 10 V/um during the

transition between points three (3) and four (4). At the end of the relaxation phase, the E-field strength was decreased to just 3 V/um.

2.4.2.1 Constant Charge

The outcome of the CC experiment is displayed in Figure 2.7. More specifically, Fig. 2.7(a) illustrates the simulated and the measured DEAP voltages, while Fig. 2.7(b) depicts the DEAP model predicted force against the actual measured one, with extra focus being given, in the enclosed insets, on the charging and discharging instances and the respective forces response.

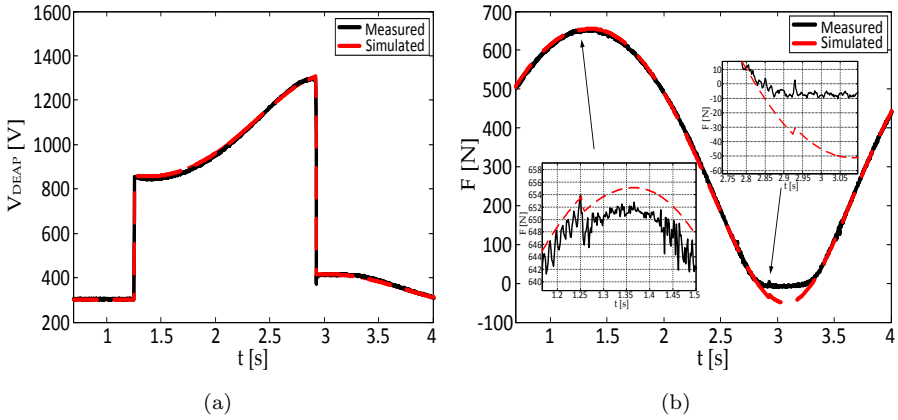

Figure 2.7: DEAP generator (a) simulated voltage versus measured voltage (b) model predicted force versus measured force during a CC experiment at $f = 0.3$ Hz cycling frequency.

The model predicted and measured forces are in agreement during steady-state conditions, as well as during the transient charging and discharging instances. Indeed, during the charging process, and for a DEAP voltage boost of +600 V, the DEAP force step reduction was correctly predicted close to −3 N, whilst during the discharging process, and for a DEAP voltage deviation of −900 V, the respective DEAP force escalation was found approximately equal to +5 N.

Besides the generally unreliable measurement of negative force, a small discrepancy between the model predicted force and the actual measured one can be attributed, among other factors, to mismatches between the simulated and the measured DEAP voltage, due to the customized PLECS® solver configurations. Nevertheless, both the force and voltage variance sign notations highlight the actuation mechanisms of the DEAP sheets during the charging and discharging instances. Indeed, a positive voltage variation acts in favour of the expanding forces, while a negative voltage variation acts in favour of the contracting forces.

2.4.2.2 Constant Voltage

The results of the CV experiment can be seen in Fig. 2.8. Similarly to Fig. 2.7, Fig. 2.8(a) illustrates the simulated and the measured DEAP voltages, while the model predicted force and the actual measured one can be appreciated in Fig. 2.8(b). In the enclosed insets of Fig. 2.8(b), a closer look of the force response during the charging and the multiple discharging instances is given.

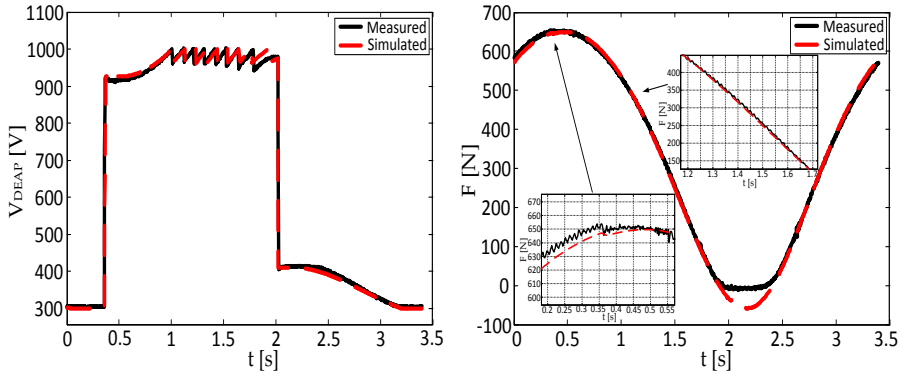

(a) (b)

Figure 2.8: DEAP generator (a) simulated voltage versus measured voltage (b) model predicted force versus measured force during a CV experiment at $f = 0.3$ Hz cycling frequency.

Consistently with the CC experiment, the force imposed on the DEAP generator decreased by approximately -3 N, as its voltage was boosted up to 900 V. Still, during the relaxation phase, and while the buck converter was triggered several times, in order to form the CV cycle, no significant change in either the model predicted force or the actual measured one could be appreciated, due to the rather narrow hysteresis band chosen for the DEAP voltage, cf. Table 2.2.

2.4.2.3 Constant E-field

The performance of the model, for the CE experiment is presented in Fig. 2.9. Customarily, Fig. 2.9(a) illustrates the simulated and the measured DEAP voltages, while Fig. 2.9(b) depicts the DEAP model predicted force against the actual measured one, with extra focus being given, in the enclosed insets, on the charging and discharging instances and the respective forces response.

Equivalently to the CC and CV experiments the model predicted force and measured one retain a good match in both static and transient states. Indeed,

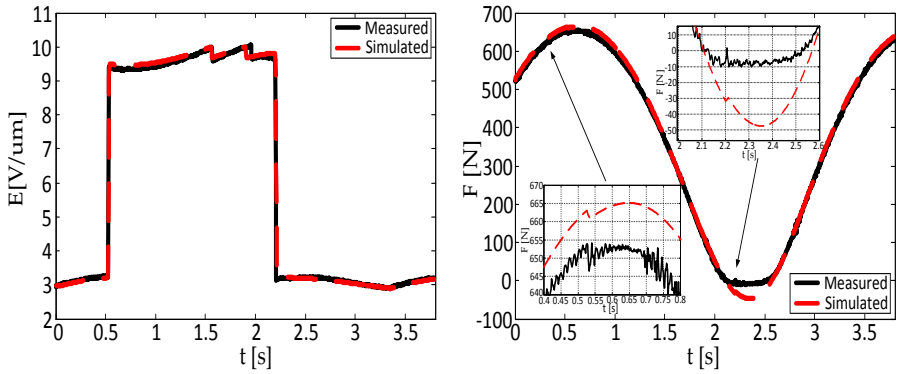

(a) (b)

Figure 2.9: DEAP generator (a) simulated voltage versus measured voltage (b) model predicted force versus measured force during a CE experiment at $f = 0.3$ Hz cycling frequency.

as in the CC and CV experiments, the model predicted force variation during the charging instance was equal to -3 N. However, the increase of the predicted force during the discharging instance in the CE cycle was less that the respective one in the CC cycle, as the voltage drop was approximately equal to -800 V. Finally, during the CE experiment, there was no significant force variation during the relaxation phase, like in the CV experiment, due to the rather narrow hysteresis band chosen for the DEAP E-field strength, cf. Table 2.2.

2.5 Summary

This chapter delivered a short introduction to the DEAP technology, highlighting the milestones that enabled Danfoss PolyPower® A/S to possess a pilot, unique and scalable roll-to-roll production process, capable of manufacturing kilometres of DEAP film per week. A first insight in the principal energy harvesting cycles of a DEAP generator was also given. An electromechanical model for a cube-shaped DEAP generator was designed and its parameters were identified via merely mechanical experiments. Finally, the model performance was assessed for all energy harvesting cycles via respective experiments, demonstrating a good match between the predicted force and the measured one.
.

This page is intentionally left blank

Chapter 3

Experiences with Demo#0

3.1 Introduction

This chapter introduces demo#0 and highlights all key-points of the accumulated experience associated with its use; in the period set by the PhD project commencement in 2012 and the design of the subsequent demo#1 in mid-2013. The kick-off goal of demonstrator#0 was to provide ample experimental data in order to verify the electromechanical model of the cube-shaped DEAP generator presented in Chapter 2 and to form the actual platform upon which the energy harvesting cycles of the latter one would be experimentally outlined.

3.2 Demo#0 description

Demo#0 consisted of a mechanical test rig enabling the cycling of the polymer sheets under various frequencies and stretch configurations and of a power electronic converter appointed to charge and discharge the DEAP generator(s). Indeed, demo#0 supported the in-phase co-cycling of up to four (4) DEAP generators, mechanically/electrically connected in parallel. A 3D CAD design of the demonstrator is illustrated in Fig. 3.1(a), while an actual picture of it standing within Aalborg University's laboratory facilities is displayed in Fig. 3.1(b).

3.2.1 Mechanical test rig

The mechanical test rig was enclosed by an aluminium weldment frame with dimensions $200 \times 66 \times 74$ cm. The mechanical setup consisted of a Bauer® induction motor (model BG20-11/D09SA4-TF) coupled to the DEAP generator

(a) (b)

Figure 3.1: Demo#0 (a) 3D CAD design (b) in Aalborg University laboratory premises.

via a circular disc and a configurable arm, which set the pre-stretch of the DEAP sheets. Virtually, both the circular disc and the top frame of the rig had three (3) different setting points, forming a total of nine (9) different delta-strain configurations between 40 % and 80 %. The induction motor velocity and direction was controlled via a Danfoss® VLT® micro drive (model 132F 0022).

In order to acquire real-time displacement and force data a Solartron Metrology® LVDT (model S-Series AS/100/G) was installed in parallel with the generator, while mounted on top of the latter one laid a Tedea® load cell (model 615). Prior to driving the transducers output to the National Instrument (NI) CompactDAQ (NI-cDAQ™) 9178 chassis, and in order to utilize the 16-bit resolution of the measuring bundle installed in it (model NI-9222), use of two (2) RDP® amplifiers was made (models S7AC and S7DC) to magnify their low-amplitude output signals. All data were then fetched to a computer, where a LabVIEW™ Virtual Instrument (VI) was designed to process them on the fly.

3.2.2 DEAP generator

Danfoss PolyPower® A/S supplied AAU with four (4) DEAP generators, to be used with demo#0, with relaxed-state dimensions $l_x^{(0)} = 0.25$ m, $l_y^{(0)} = 0.23$ m, $d_z^{(0)} = 130$ um and $l_z^{(0)} = 6.24$ mm. Figure 3.2(a) presents the generators technical drawing and Fig. 3.2(b) depicts two of them installed in demo#0, forming the cube-shaped generator modelled in Chapter 2. Demo#0 allowed for a wide range of configurations, being able to cycle one (1), two (2), three

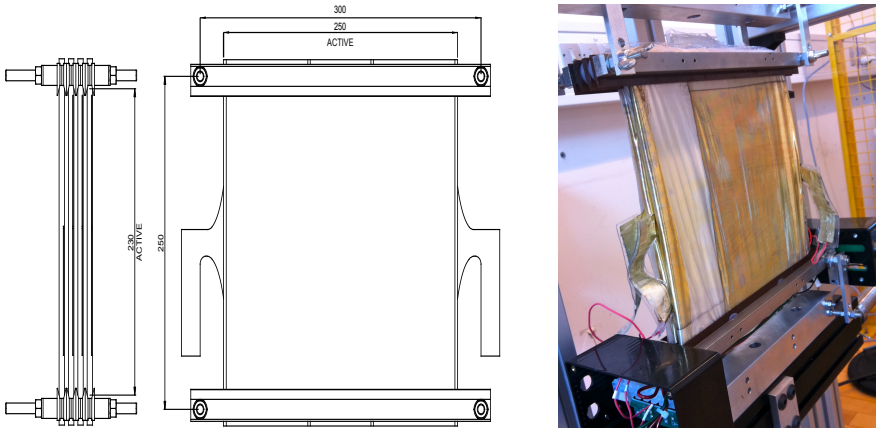

(a) (b)

Figure 3.2: DEAP generator (a) technical drawing (b) installed on demo#0 (2 pieces installed in parallel).

(3) or even all four (4) DEAP generators at 40 %, 60 % or even 80 % delta-strain. Table 3.1 outlines each DEAP generator relaxed-state characteristics.

Table 3.1: Demo#0 DEAP generators relaxed-state characteristics.

Characteristic	Value
Mass m	0.395 kg
Density ρ	1.1 g/cm^3
Capacitance $C^{(0)}$	500 nF
Rel. permittivity ε_{rel}	3.1
Serial resistance R_{serial}	10 Ohm
Parallel resistance R_{parallel}	40 GOhm
Rated E-field strength E_{rated}	30 V/um

Measurements conducted on all four (4) DEAP generators via a Wayne Kerr® precision magnetics analyser (model 3260B), reported slight mismatches among their expected and their actual capacitance values, due to imperfections in the film fabrication process and/or misalignments of the DEAP layers during their lamination. The overall mismatch for the case where all four (4) DEAP generators are connected in parallel was found approximately equal to 70 nF.

3.2.3 Power electronic converter

A typical non-isolated bidirectional half-bridge buck-boost converter, frequently found, among other applications, in hybrid and electric vehicles with regenerative braking mechanisms [**?**, **?**, **?**, **?**], renewable energy systems with energy storage capabilities [**?**, **?**], and other high-power-density designs [**?**, **?**], was employed to enable the DEAP generator on demo#0 and to form the CC, CV and CE energy harvesting cycles. The converter consisted of a custom-made toroidal inductor (Kool Mu® core), two high-voltage IXYS IGBTs (model IXGF25N300), i.e. T_{buck} and T_{boost} and two high-voltage VMI Inc. diodes (model K50UF), i.e. D_{boost} and D_{buck}, respectively installed across T_{buck} and T_{boost} and its schematic can be appreciated in Fig. 3.3. The top layer of the non-isolated bidirectional half-bridge buck-boost converter is graphically illustrated in Fig. 3.4.

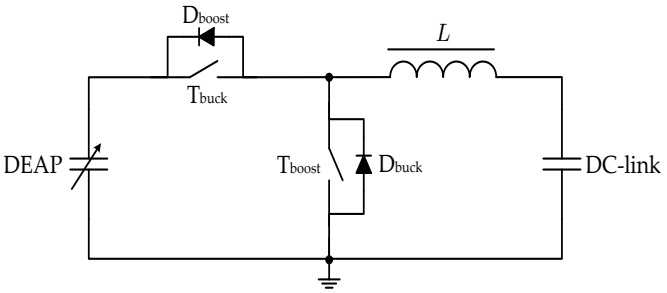

Figure 3.3: Schematic of the non-isolated bidirectional half-bridge buck-boost converter.

The non-isolated half-bridge buck-boost converter is highly attractive for bidirectional applications, due to its simple control, low component count and high efficiency in low and medium power designs. However, it does not offer galvanic isolation and it necessitates for a floating driver for the high-side switch. Furthermore, as both T_{buck} and T_{boost} switches need to be rated to the full voltage of the converter, the high-efficient operational range of the latter one in high-voltage low and medium power applications is significantly narrowed.

The operation of the converter was based upon the real-time position feedback provided by the LVDT and its control comprised of two interrelated loops. The main control loop was monitoring the DEAP voltage, during both buck and boost converter functions, while the ancillary control loop was configuring the peak-value of the current flowing through the toroidal inductor. Besides IGBT desaturation control, several auxiliary protection circuits were also designed, latching the converter into fault mode, including DEAP and DC-link overvoltage, DEAP and DC-link overcurrent and IGBT case temperature monitoring.

3.2.3.1 Analogue peak-current control

Current conduction modes in DC-DC converters can be distinguished in the Continuous Conduction Mode (CCM), Boundary Conduction Mode (BCM) and the Discontinuous Conduction Mode (DCM); differentiated based on the magnetization state of the main magnetic element during each switching period. Indeed, during CCM the core is never entirely demagnetized during a switching period, as current continuously flows through the magnetic element windings. In BCM, on the other hand, the core is completely demagnetized at the end of each switching period, as the current flowing through the magnetic element windings is reduced to zero. Lastly, in DCM, and during each switching period, the core is sustained demagnetized for a relatively short period of time [**?**].

CCM is well-known to offer the lowest current ripple through the magnetic element thus favouring its design. Yet, CCM is also characterized by relatively high turn-on loss in the main transistor, due to both the operating current and the hard turned-off freewheeling diode recovery. In addition, converters operating in CCM have limited transient response bandwidths, due to an inherent zero present in their control-to-output transfer function right half-plane [**?**].

During BCM, on the other hand, there is no zero in the right half-plane of the converter control-to-output transfer function and the freewheeling diode and the main transistor are respectively turned off and on softly thus reducing the switching loss. Howbeit, the inductor/transformer ripple current is increased to the peak-value of the respective current perplexing the former one's design.

Finally, in DCM, even though the turn-on loss of the main transistor is essentially eliminated, switch-node ringing occurs, leading to radiated and conducted ElectroMagnetic Interference (EMI). More, the design of the magnetic element is further penalized, as not only is the inductor/transformer ripple current equal to the peak-value of the corresponding current, but also the peak-to-average current ratio and Root Mean Square (RMS) current are relatively high [**?**].

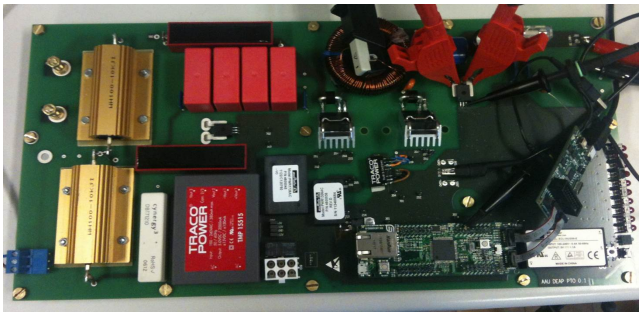

Figure 3.4: Graphical illustration of the bidirectional half-bridge buck-boost converter.

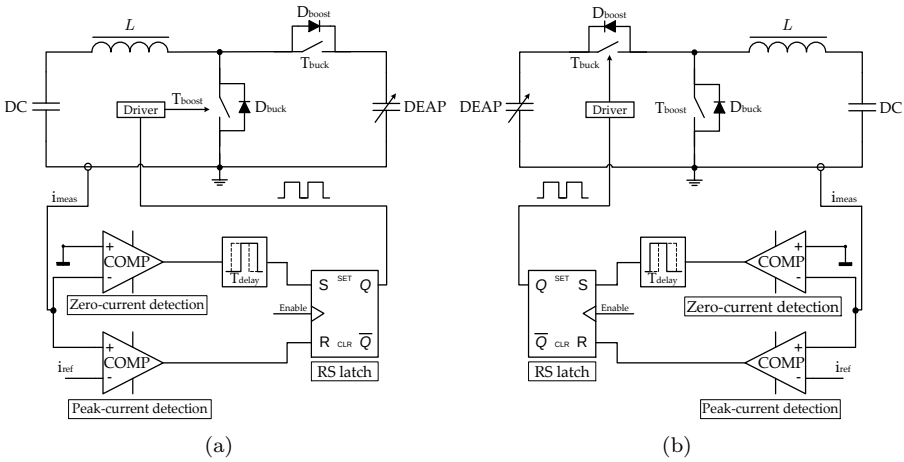

Figure 3.5: Analogue peak-current controller schematic for the (a) boost (b) buck function.

Figure 3.5 depicts the analogue peak-current controller designed to accommodate the operation of the half-bridge converter buck and boost functions [**?**]. An Allegro® Hall effect-based current sensor (model ACS756) was placed in the return path of the converter sensing the current flow during both buck and boost functions. The measured current was subsequently driven through two Microchip® comparators (model MCP6564) invoked to detect the zero-current and peak-current instances. The zero-current detection circuit was used to provide the *'set'* pulse to a Texas Instrument (TI) RS latch (model CD4043BD), while the peak-current detection circuit was used to provide the *'reset'* pulse. The RS latch output was enabled/disabled by the DEAP voltage control, which was coded in the TI microcontroller (model LM3S9B92) using one of its ADCs.

A simple RC circuit, in low-pass filter configuration, was installed between the zero-current detection circuit and the RS latch, introducing a fixed-time delay in the driving pulse thus configuring the operation mode of the converter between BCM and DCM. In either case, the converter operates with variable switching frequency as IGBTs turn-on and turn-off times are operational point dependent. Finally, the output of the RS latches was directly connected to the Avago drivers (model HCPL-316J) employed to drive both converter IGBTs.

Figure 3.6 illustrates the operation of the converter under both BCM and DCM as it was recorded via a Tektronix® oscilloscope (model DPO2014). Figs. 3.6(a) and 3.6(b) present the operation of the converter boost function under BCM and DCM, while the load voltage was boosted from 500 V to 2500 V by 10 A current pulses. Accordingly, Figs. 3.6(c) and 3.6(d) depict the operation of the converter buck function under BCM and DCM, while the load voltage was

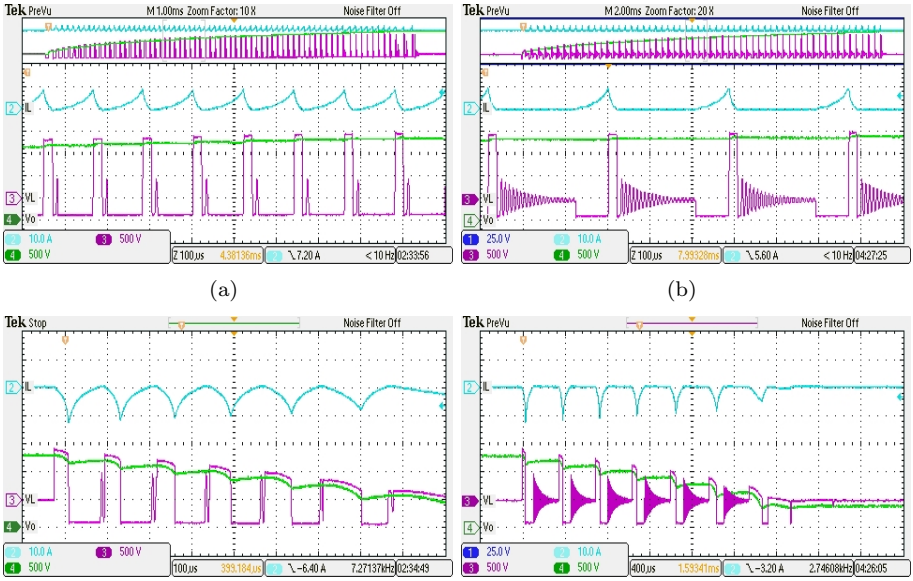

Figure 3.6: Boosting load voltage to 2500 V by 10 A current pulses (a) BCM (b) DCM. Bucking load voltage from 1250 V by 10 A current pulses (c) BCM (d) DCM.

bucked from 1250 V to 500 V by 10 A current pulses. In all cases, the inductor current is displayed on channel two (2), the half-bridge midpoint connection voltage on channel three (3) and the load voltage on channel four (4).

The peak-current controller operation during the boost function of the converter is highly effective, as the low DC-link voltage, i.e. 400 V, and the inductance of the magnetic element, i.e. 7 mH, result in relative long turn-on times for the T_{boost} transistor, minimizing the influence of the integrated circuits propagation delays on the peak-current controller accuracy. During the buck function, on the other hand, and as seen in Figs. 3.6(c) and 3.6(d), the large input-output voltage ratio, results in shorter turn-on times for the T_{buck} transistor, challenging the peak-current controller precision at the first pulses.

Indeed, assuming similar peak-current references, while omitting voltage drops in the converter active/passive components, the ratio between the boost and buck functions turn-on times, respectively denoted by $t_{boost,on}$ and $t_{buck,on}$ is

$$\frac{t_{boost,on}}{t_{buck,on}} = \left(\frac{V_{DEAP}}{V_{DC\text{-}link}} - 1 \right) \tag{3.1}$$

where $V_{DC\text{-}link}$ corresponds to the DC-link voltage.

3.3 Experimental results

In the following subsections the DEAP generator, comprising of all available elements, and the bidirectional half-bridge buck-boost converter are independently characterized. More, an appropriate comparative benchmark is established prior to the experimental outline of the distinct energy harvesting cycles.

3.3.1 DEAP generator characterization

The DEAP generator was installed in demo#0 and its relaxed-state capacitance was measured equal to 1.93 uF. In order to attain a sinusoidal-like deformation curve the DEAP generator was pre-stretched by 3 %, increasing its capacitance to 2 uF; indicating that $\kappa = 1.4$. Demo#0 transducers were configured to report zero force and zero displacement at the 3 % pre-stretch position. At the 40 % delta-strain position the DEAP capacitance was measured equal to 3.15 uF.

The NI-cDAQ$^{\text{TM}}$ 9178 chassis was configured to record synchronized data of DEAP force F and displacement x, at a sampling rate equal to 2500 S/s. Figures 3.7(a) and 3.7(b) illustrate the progression of the acquired force and displacement signals for a 40 % delta-strain cycle at 0.25 Hz, while Figure 3.7(c) on the other hand, depicts the mechanical potential energy of the DEAP generator. The latter one's arithmetic mean,

$$\bar{U}_m = \frac{1}{n_\text{s}} \sum_{k=1}^{n_\text{s}} F[k]x[k], \tag{3.2}$$

results in the average mechanical potential energy of the DEAP generator; found as 43 J per 40 % delta-strain cycle[1]. Yet, as the DEAP film exhibits viscoelastic properties, the two sinusoidal-like waves of DEAP force and displacement, had a frequency-dependent, relative phase difference i.e. angle δ. Plotting the force and displacement data against one another, as in Fig. 3.7(d), forms a hysteresis loop analogous to the stress-strain hysteresis loop of a viscoelastic material. In a merely mechanical experiment, the area enclosed by this loop can be attributed to viscous loss, or in other words, to the part of the DEAP mechanical potential energy that was dissipated internally as heat. Indeed, according to [**?**], the loss tangent tanδ is equal to the ratio of the tensile loss modulus $E^{''}$ to the tensile storage modulus $E^{'}$

$$\tan\delta = \frac{E^{''}}{E^{'}} = \frac{\text{energy loss}}{\text{energy stored}}. \tag{3.3}$$

[1]The small data set of negative force documented in Fig. 3.7(a) had an infinitesimal effect on the calculation of $\bar{U}_m$. Nevertheless, and in consistency with Chapter 2, it was disregarded as it was of an ambiguous nature.

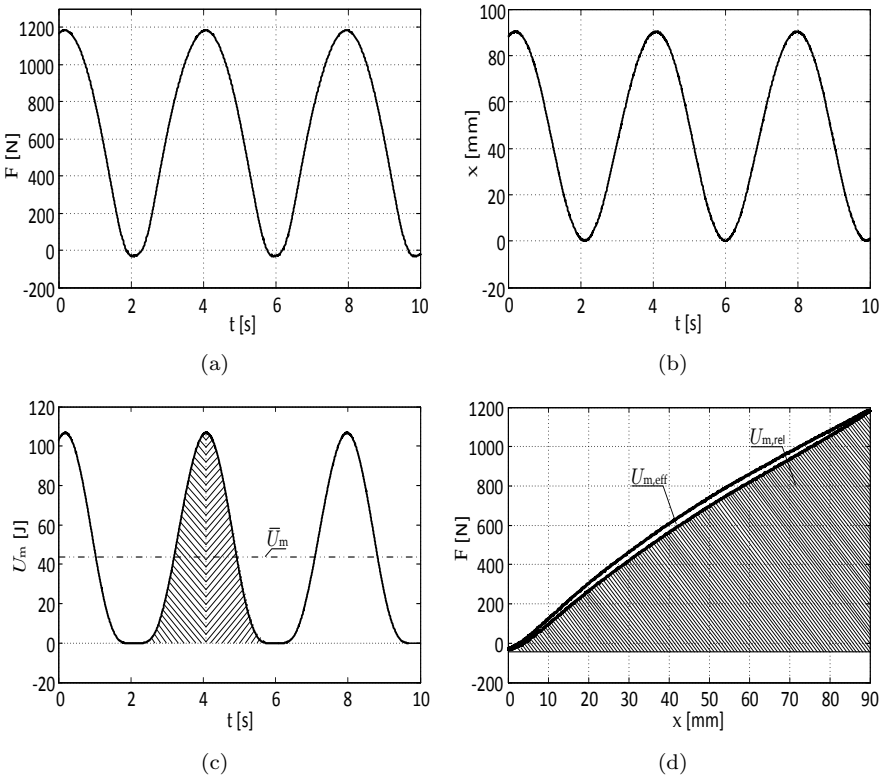

Figure 3.7: DEAP generator progression of (a) force (b) displacement (c) mechanical potential energy over time and (d) force-strain curve for a 40 % delta-strain cycle at 0.25 Hz.

Therefore, the DEAP mechanical efficiency, expressing the percentage of the DEAP mechanical potential energy that was used to cycle the DEAP generator, can be calculated via

$$\eta_{\text{DEAP}} = \frac{1}{1 + \tan\delta}. \tag{3.4}$$

Table 3.2 illustrates the DEAP mechanical efficiency for various cycling frequencies. As expected for a material demonstrating viscoelastic behaviour, the DEAP mechanical efficiency is decreasing as the cycling frequency increases. Indicatively, for a cycling frequency equal to 1 Hz, approximately 6 %, i.e. 3 J, of the DEAP mechanical potential energy needed to stretch and relax the DEAP sheets at 40 % delta-strain, is dissipated as heat. In a practical, non-merely mechanical application, however, the area enclosed by the hysteresis loop reflects the summation of the material viscous loss and the amount of mechanical energy converted into electrical one. Hence, and as several DEAP

Table 3.2: DEAP generator mechanical efficiency.

f	0.2 Hz	0.4 Hz	0.6 Hz	0.8 Hz	1 Hz
δ	2.75 ^{o}	3.08 ^{o}	3.37 ^{o}	3.64 ^{o}	3.84 ^{o}
η_{DEAP}	95.4 %	94.9 %	94.4 %	94.0 %	93.7 %

generators may be installed out-of-phase in the same circular disk, in order for their expanding/contracting forces to cancel-out, maximizing the effective utilization of the infrastructure input mechanical energy, only the remainder of the subtraction between the DEAP mechanical potential energy during the stretching phase i.e. $U_{m,\text{str}}$, and the DEAP mechanical potential energy during the relaxation phase, i.e. $U_{m,\text{rel}}$, may be considered as effective mechanical potential energy for the DEAP generator

$$U_{m,\text{eff}} = U_{m,\text{str}} - U_{m,\text{rel}}. \tag{3.5}$$

As highlighted in Fig. 3.7(d) $U_{m,\text{str}}$ and $U_{m,\text{rel}}$ were, in all experiments, calculated using MATLAB® trapezoidal numerical integration function *'trapz'*.

3.3.2 Power electronic converter characterization

High-precision power analysers are commonly employed to estimate the energy efficiency of power electronic converters. However, as DEAP generator typical cycling frequencies lie within $f \in (0, 10]$ Hz, the need to precisely measure high-peak but relatively low-average currents arises. In addition, as the DEAP generator can be considered as a purely capacitive load, i.e. the capacitor reactance is orders of magnitude less than its respective shunt resistance in the examined switching frequency range ($X_C \ll R_{\text{parallel}}$), measuring the converter efficiency with a power analyser would demand loading the converter resistively. Thus, the energy efficiency of the bidirectional half-bridge buck-boost converter was mapped by loading its input and output ports capacitively and monitoring the energy exchange between them using high-impedance voltage probes.

More specifically, an external Delta Elektronika DC power supply with power sink option (model SM 400-AR-4) was initially coupled to the converter DC-link ports in parallel with a large film capacitance. To avoid futile stress on the available DEAP generators, a similarly-sized fixed polypropylene film capacitor (1.5 uF) was used as pseudo-DEAP, as Andersen et al. in [**?**] demonstrated that polypropylene film capacitors can realistically emulate DEAP generators, since they both have a voltage independent capacitance characteristic. After granting the converter adequate time to reach thermal steady-state, the DC

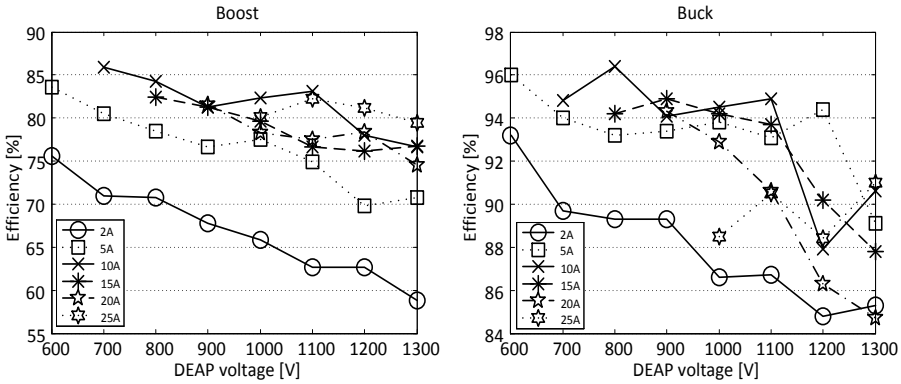

(a) (b)

Figure 3.8: Energy efficiency map of the non-isolated bidirectional half-bridge buck-boost converter (a) boost and (b) buck functions for various DEAP voltages and peak-current references.

power supply was decoupled from the system, allowing for real-time monitoring of the energy transfer between the two gradually discharging capacitors.

Estimating the energy efficiency of a power electronic converter by loading its ports capacitively is a straightforward process, as any mismatch between the amount of energy drawn from one capacitor and the energy finally stored to the other one can be unequivocally attributed to converter loss. In addition, the absence of current sensors, not only simplifies the experimental setup design and downscales cost, but it also eliminates the inevitable voltage drop across the former ones, which may lead to efficiency underestimation/overestimation. Yet, this simple and straightforward technique provides only a fairly accurate estimation of the energy efficiency of the converter and only at a specific operating point. Indeed, the accuracy of the energy efficiency estimation depends, among else, on the amount of energy transferred in respect to the capacitors sizes as well as on the oscilloscope resolution. Averaging, as to increase the reliability of the measurement, may result in a tedious and protracted process.

The net electric potential energy of either of the capacitors after the termination of a buck or boost function is given by,

$$U_{e,\text{net}} = U_{e,\text{post}} - U_{e,\text{prior}}, \tag{3.6}$$

where $U_{e,\text{net}} > 0$ reflects accumulation of charge while $U_{e,\text{net}} < 0$ attribution of it. Hence, the efficiency of the two distinct converter functions could be straightforwardly assessed via

$$\eta_{\text{boost}} = \left| \frac{U_{e,\text{net,DEAP}}}{U_{e,\text{net,DC-link}}} \right| \qquad \eta_{\text{buck}} = \left| \frac{U_{e,\text{net,DC-link}}}{U_{e,\text{net,DEAP}}} \right|. \tag{3.7}$$

where η_{boost} and η_{buck} denote the energy efficiency of the boost and buck converter functions respectively. Fig. 3.8 illustrates the experimentally documented energy efficiency maps of the boost and buck functions of the converter under a wide spectrum of different DEAP voltages and peak-current references. To improve the converter performance the high-voltage VMI diodes were replaced with CREE® SiC diodes (model C3D10170H). The DC-link voltage was set to 300 V and the DEAP voltage after every buck function was 400 V.

It is evident that the buck function of the converter is more energy efficient than the respective boost function. Indeed, the converter operates with energy efficiency above 94 % for a wide range of operational voltages and peak-currents while bucking, whilst during boosting the converter efficiency lies around 85 %. However, it is clear that during the boost function of the converter, the losses of the latter one, have to be compensated for, leading to larger amounts of energy being transferred in comparison with the respective buck operating point.

3.3.3 Comparative benchmark

Prior to the experimental testing, and in order to effectively compare the distinct energy harvesting cycles of a DEAP generator by means of energy gain, energy harvesting efficiency and energy conversion efficiency, an appropriate comparative benchmark must be established. According to [**?**], the absolute energy gain of the three (3) distinct energy harvesting cycles is given by

$$\Delta U_{\text{CC,abs}} = U_{e,\max}\left(1-\alpha^2\right), \tag{3.8}$$

$$\Delta U_{\text{CV,abs}} = U_{e,\max}\left(1-\alpha^2\right), \tag{3.9}$$

$$\Delta U_{\text{CE,abs}} = 2U_{e,\max}\ln\left(\frac{1}{\alpha}\right). \tag{3.10}$$

where $U_{e,\max}$ can be calculated, in accordance with eq. (2.40), by

$$U_{e,\max} = \frac{1}{2}\varepsilon V_{\text{ol}} E_{\max}^2, \tag{3.11}$$

while the geometric constant α, expressing the deformation characteristics of the generator, can be respectively evaluated as

$$\alpha = \left(\frac{C^{(0)}}{C^{(\lambda_x)}}\right)^{1/2}, \quad \alpha \in (0,1), \tag{3.12}$$

where $C^{(\lambda_x)}$ reflects the DEAP generator capacitance at λ_x stretch. Equations (3.8), (3.9) and (3.10) indicate that for any α satisfying (3.12)

$$\Delta U_{\text{CE,abs}} > \Delta U_{\text{CC,abs}} = \Delta U_{\text{CV,abs}}. \tag{3.13}$$

It is thus straightforwardly concluded that in order to ensure the applicability and the validity of the conducted comparative analysis, the latter one should be based upon a common maximum E-field strength value, attained by the DEAP generator during each energy harvesting cycle. Indeed, for a common maximum E-field strength value, each harvesting cycle relative energy gain, expressing the ratio between their absolute energy gain and the energy stored in the DEAP generator during the boost function, can be assessed via

$$\Delta U_{\mathrm{CC,rel}} = \frac{1-\alpha^2}{\alpha^2} \tag{3.14}$$

$$\Delta U_{\mathrm{CV,rel}} = \left(1-\alpha^2\right), \tag{3.15}$$

$$\Delta U_{\mathrm{CE,rel}} = 2\ln\left(\frac{1}{\alpha}\right). \tag{3.16}$$

Equations (3.14), (3.15) and (3.16) indicate that for any α satisfying (3.12)

$$\Delta U_{\mathrm{CC,rel}} > \Delta U_{\mathrm{CE,rel}} > \Delta U_{\mathrm{CV,rel}}. \tag{3.17}$$

3.3.4 Energy harvesting cycles outline

The experimental setup used to outline the DEAP generator energy harvesting cycles was similar to the one used to characterize the bidirectional half-bridge buck-boost converter. Indeed, promptly after the disconnection of the external DC power supply, all energy harvested was stored in the DC-link capacitor thus increasing its voltage. The latter one's progression over time was monitored via a high-voltage Teledyne LeCroy$^{\mathrm{TM}}$ probe (model PPE2KV) and a Tektronix® oscilloscope (model DPO2014). The probe energy loss was estimated as

$$U_{\mathrm{probe}} = \int_0^t \frac{\bar{V}^2_{\mathrm{DC\text{-}link}}}{R_{\mathrm{probe}}}\mathrm{d}t, \tag{3.18}$$

where $\bar{V}_{\mathrm{DC\text{-}link}}$ corresponds to the mean value of the DC-link voltage, after the disconnection of the DC power supply, and R_{probe} reflects the impedance imposed by the high-voltage probe. The energy harvesting efficiency of a cycle can be defined as the ratio of its energy gain ΔU, accounting for the probe loss, to its absolute energy gain ΔU_{abs}, reflecting the percentage of the maximum theoretical energy gain of the respective cycle that was actually harvested

$$\eta_{\mathrm{cycle}} = \frac{\Delta U}{\Delta U_{\mathrm{abs}}}, \tag{3.19}$$

for the given values of E_{max} and α. The DEAP generator energy conversion efficiency on the other hand, is defined as the ratio of its energy gain to its

effective mechanical potential energy,

$$\eta_{\text{con}} = \frac{\Delta U}{U_{m,\text{eff}}}. \tag{3.20}$$

Table 3.3 illustrates the converter control settings during the energy harvesting cycles outline. Analogously to Table 2.2, the 'Boost' and 'Buck' columns indicate the buck-boost converter main control parameter at the energy harvesting cycles points two (2) and four (4) respectively, while the 'Hysteresis band' column on the other side, indicates the variation of the control parameter during the relaxation phase of the DEAP generator. In all experiments the latter one was cyclicly deformed at a frequency of 0.85 Hz and a delta-strain of 40 %. Consequently, the geometric constant α was also invariable and equal to 0.8.

Table 3.3: Converter control settings during the energy harvesting cycles outline.

Cycle	Boost	Buck	Hysteresis Band
CC	700 V	500 V	700 V - 1100 V
CV	750 V	500 V	750 V - 950 V
CE	8 V/um	5 V/um	8 V/um - 10 V/um

The outcome of the energy harvesting experiments is summarized in Table 3.4. The CC cycle demonstrated the highest energy gain, scavenging 106.6 mJ per cycle, characterized by the highest energy harvesting efficiency, i.e. 20.6 %, and the highest energy conversion efficiency, i.e. 3.5 %, as well. Figure 3.9 depicts the DC-link voltage progression over time during the CC experiment. Alongside the CE field cycle, which reported comparable energy gain per cycle, i.e. 87.6 mJ, followed by a 15.3 % energy harvesting efficiency and a 2.9 % energy conversion efficiency. Last, the CV cycle which documented inferior performance to both CC and CE cycles with only 42.5 mJ being gained per cycle, corresponding to the lowest energy harvesting efficiency, i.e. 10.9 % and the lowest energy conversion efficiency, i.e. 1.6 %.

Table 3.4: DEAP generator energy harvesting experiments outcome.

Cycle	ΔU_{abs}	ΔU	$\Delta U_{\text{per cycle}}$	$\Delta P_{\text{per cycle}}$	η_{cycle}	η_{con}
CC	16.57 J	3.41 J	106.6 mJ	90.6 mW	20.6 %	3.5 %
CV	14.25 J	1.55 J	50 mJ	42.5 mW	10.9 %	1.6 %
CE	18.87 J	2.89 J	87.6 mJ	74.5 mW	15.3 %	2.9 %

The DEAP generator maximum E-field strength during the CC cycle, was estimated as 8.5 V/um, which according to Table 3.1 corresponds to approximately

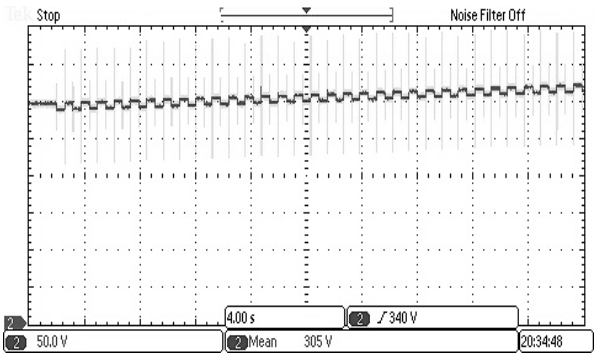

Figure 3.9: DC-link voltage time progression during the CC energy harvesting experiment.

30 % of the generator rated E-field strength. Driving the DEAP generator with its rated E-field, should boost its energy gain by more than ten (10) times, as the latter one is proportional to the maximum E-field strength attained squared, cf. (3.8). Such operation, however, would demand for a high-efficient bidirectional buck-boost converter, whilst Figs. 3.8(a) and 3.8(b) indicate that the energy efficiency of the buck and boost functions of the bidirectional half-bridge buck-boost converter decreases with the increasing operating voltages.

Nevertheless, it is now evident, that the CV cycle should not be considered as a CC counterpart, as not only does it offer less relative energy gain, cf. (3.17), but in the same time it is characterized by less energy gain and thus less energy conversion efficiency as well. Indeed, even if theoretically a CV cycle can offer comparable absolute energy gain to a CC cycle, cf. (3.13), in practical applications it will demonstrate inferior performance, due to the converter finite energy efficiency. Yet, and as indicated in Table 3.3 'Hysteresis Band' column, a CV cycle offers direct control on the DEAP generator voltage swings during its relaxation phase, leading to less voltage stress on the power electronic converter components, in regard to an absolute-energy-gain-wise equivalent CC cycle.

Even though the CC cycle proved to be the most energy efficient one during the experimentation with demo#0, conflicting with cf. (3.13), that should not be considered as a paradox. Rather than that, what the DEAP generator energy harvesting experiments outcome indicates is that for the CE cycle to be considered a strong competitor to the CC cycle, a high-efficient power electronic converter, driving the DEAP sheets close to their operational limits, should be designed. Indeed, in the absence of such high-efficient power electronic converter, the CC cycle demonstrated superior performance to the CE cycle as it made less use of the most lossy component of the energy harvesting system.

Indicatively, reassessing the data for the CC cycle, by taking into account the converter losses for a peak-current reference of 7.5 A for both buck and

boost functions, yields 256.2 mJ energy gain per cycle, which corresponds to 217.8 mW per cycle, 49.5 % energy harvesting efficiency and 8.5 % energy conversion efficiency. Hence, it is now clear that, in the most energy efficient experiment, 58.4 % of the generator absolute energy gain was dissipated in the converter as heat during the latter one's inefficient buck and boost functions.

3.4 Summary

This chapter introduced the first complete DEAP generator energy harvesting system, i.e. demo#0. The DEAP generator installed in the demonstrator and the power electronic converter employed to drive it were independently characterized and a comparative benchmark was established, prior to the experimental outline of the former one's energy harvesting cycles. Last, mechanical energy was successfully converted into electrical one, under all distinct energy harvesting cycles, with documented peak energy conversion efficiency of 3.5 %.

This page is intentionally left blank

This page is intentionally left blank

Chapter 4

Experiences with Demo#1

4.1 Introduction

This chapter introduces demo#1 and summarizes all acquired knowledge and experience associated with its use during the period from mid-2013 to mid-2014. The kick-off goal of demo#1 was to display higher energy gain in regard to demo#0, by driving a single DEAP generator at high E-field strengths, via a pertinent power electronic converter. At the same time, demo#1 aimed at increasing the infrastructure input mechanical energy utilization factor, by enabling the co-cycling of a number of DEAP generators installed out-of-phase.

4.2 Demo#1 description

Demo#1 consisted of a mechanical test rig enabling the out-of-phase co-cycling of four (4) DEAP generators under various frequencies and stretch configurations and of a power electronic converter appointed to charge and discharge one of them. Side-view and front-view 3D CAD designs of the mechanical test rig, are respectively illustrated in Figs. 4.1(a) and 4.1(b), while an actual picture of it, within Aalborg University's laboratory facilities, is depicted in Fig. 4.1(c).

4.2.1 Mechanical test rig

The mechanical test rig was enclosed by a metallic frame with dimensions $93 \times 80 \times 152$ cm. The mechanical setup consisted of a Lönne induction motor (model 7AA100L04) coupled to a 45:1 step-down gearbox and a belt drive, transmitting the angular kinetic energy of the motor crankshaft to the main

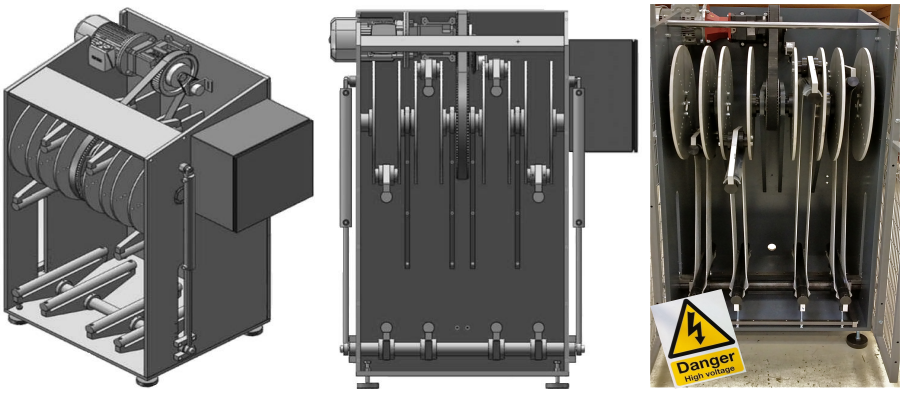

(a) (b) (c)

Figure 4.1: Quadruple mechanical test rig (a) side-view (b) front-view 3D CAD designs and (c) within Aalborg University laboratory premises.

crankshaft, upon which, and in between of two (2) disks, all four (4) DEAP generators were sequentially installed with a 90 ^{o} phase shift. In addition to the Raven induction motor (model 80a4), which was used to drive a pneumatic cylinder, setting the position of the bottom frame of demo#1, each of the disks supporting the DEAP generators had three different (3) setting points; forming a total of nine (9) different delta-strain configurations between 40 % and 80 %. In order to acquire real-time angular position and moment of force data, an incremental SICK encoder (model DFS60) and a LORENZ® torque transducer (model MR12) were installed in the gearbox output. Both sensors were connected to an NI-cDAQ™ 9178 chassis, housing a 16-bit resolution NI-9222 measuring bundle, and a VI was designed to process the acquired data.

A standalone mechanical test rig, enclosed by an aluminium weldment frame with dimensions 200 × 66 × 74 cm, offering similar strain configurations as demo#1, was used to independently characterize each of the generators prior to their installation in the quadruple demo. A 3D CAD design of the test rig is illustrated in Fig. 4.2(a), whilst an actual picture of it standing within Aalborg University laboratory premises, can be seen in Fig. 4.2(b). This new test rig consisted of a Bauer® induction motor (model BG20-11/D09SA4-TF) coupled to the DEAP generator via a circular disc and a configurable arm, which set the pre-stretch of the DEAP sheets; exactly as in demo#0. Both the circular disc and the top frame of the rig had three (3) difference setting points, forming a total of nine (9) different delta-strain configurations, analogously to demo#1.

The new mechanical test rig was, in a number of preliminary energy harvesting tests, coupled to a bidirectional tapped-inductor buck-boost converter, first introduced in section 4.2.3, forming the henceforth cited *'horizontal demo#0'*.

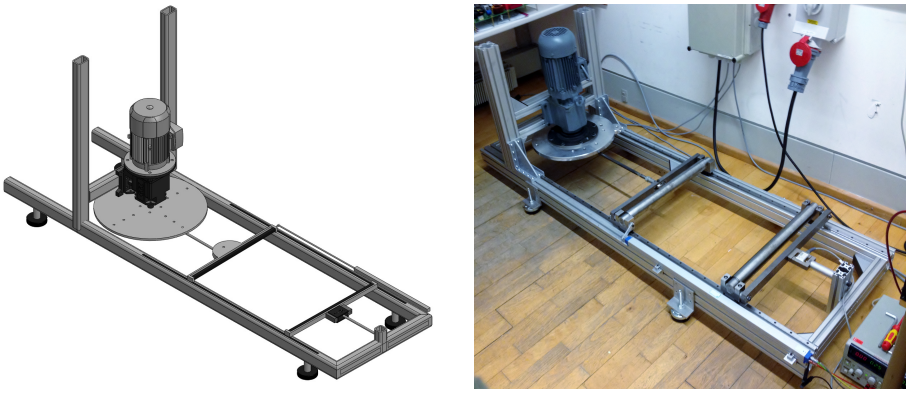

(a) (b)

Figure 4.2: Standalone mechanical test rig (a) 3D CAD design (b) within Aalborg University laboratory premises.

In order to acquire real-time displacement and force data a Vishay® LVDT (model 115L) was installed in parallel with the generator, while mounted on top of the latter one laid a Tedea® load cell (model 615). Prior to driving the force transducer output to the NI-cDAQ™ 9178 chassis, and in order to utilize the 16-bit resolution of the measuring bundle installed in it (model NI-9222), use of an RDP® amplifier was made (model S7DC) to magnify its low-amplitude output signal. All data were then fetched to a computer, where another VI was designed in LabVIEW™ to process and display them on the fly.

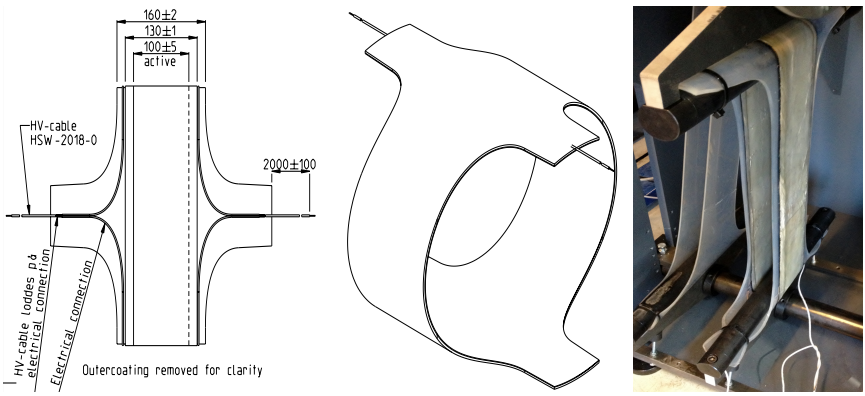

(a) (b) (c)

Figure 4.3: DEAP generator (a) technical drawing (b) schematic (c) installed in demo#1.

4.2.2 DEAP generator

Danfoss PolyPower® A/S supplied AAU with four (4) DEAP generators to be used with demo#1. The DEAP generators detailed technical drawing is presented in Fig. 4.3(a). Each generator comprised of two (2) front-to-back laminated elastomer films, which were rolled-up forming a ring-shaped structure as seen in Fig. 4.3(b). Each single-layer film relaxed-state dimensions were $l_x^{(0)} = 54$ m, $l_y^{(0)} = 60$ mm and $d_z^{(0)} = 60$ um. Figure 4.3(c) depicts one of the DEAP generators installed in demo#1, side-by-side with a dummy element, used to emulate the mechanical performance of another DEAP generator.

Table 4.1: Demo#1 DEAP generators relaxed-state characteristics.

Characteristic	Value
Mass m	0.21 kg
Capacitance $C^{(0)}$	1 uF
Serial resistance R_{serial}	5.2 Ohm
Parallel resistance R_{parallel}	10 GOhm
Rated E-field strength E_{rated}	60 V/um

Table 4.1 outlines the DEAP generators relaxed-state characteristics; elastomer density and relative permittivity are omitted as they remain as in Table 3.1.

4.2.3 Power electronic converter

The bidirectional half-bridge buck-boost converter, introduced in Chapter 3, is formed by integrating the conventional buck and boost converter designs and thus it is inevitably characterized by the same inherent shortcomings as them. Indicatively, the half-bridge converter buck function is acutely degenerating, by the demand of a very narrow duty cycle, at high step-down voltage conversion ratios, as modern Pulse Width Modulation (PWM) drivers have restrictions in their rising and falling times and they further require a minimum pulse width. The half-bridge converter boost function, on the other hand, is severely penalized, at high step-up voltage conversion ratios, by parasitic components, which diminish the former one's efficacy and efficiency under wide duty cycles.

The isolated equivalent of the bidirectional half-bridge buck-boost converter, i.e. the bidirectional flyback, opposes a good alternative at low-power designs, extending the effective duty cycle of the converter, while alleviating the high-side gate driver demands. Yet, the inclusion of a transformer, in applications

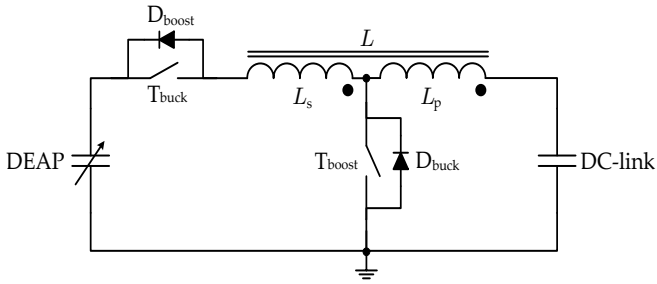

Figure 4.4: The bidirectional switch-to-tap tapped-inductor buck-boost converter schematic.

where galvanic isolation is not a prerequisite, increases inanely the complexity, cost and volume of the system, whilst suppression of overvoltages, caused by its parasitic inductances, demands for passive snubber or active clamping circuits.

Other means of extending the effective duty cycle of the converters are the quadratic and cascaded topologies, which successfully extend the duty cycle by utilizing more components, leading to inefficient and rather complex designs with limited degrees of freedom [**?**]. A new family of converters, extending the effective duty cycle of the buck and boost ones, is acquired by tapping the latter ones' magnetic components. Classification schemes for all tapped-inductor converters were proposed in [**?**] and [**?**]. Figure 4.4 illustrates the bidirectional switch-to-tap tapped-inductor buck-boost converter [**?**, **?**, **?**], used in numerous applications like high-brightness LEDs and PFC rectifiers [**?**, **?**, **?**, **?**].

The bidirectional tapped-inductor buck-boost converter extends the effective duty cycle of the bidirectional half-bridge buck-boost converter by utilizing two separate inductances during the switches on- and off- states. Indeed, high step-up as well as high step-down voltage conversion ratios can be achieved with moderate duty cycles and therefore with increased efficiency. In addition, the bidirectional tapped-inductor buck-boost converter leads to reduced switching losses across the semiconductor switches as it lightens the voltage stress of the boost switch $\mathrm{T_{boost}}$ and the current stress of the buck switch $\mathrm{T_{buck}}$, for the expense of a relatively low increase in the voltage stress of the latter one and relatively low increase in the current stress of the former one. Indeed,

$$V_{\mathrm{T_{buck}}} = V_{\mathrm{DEAP}} + (n_{\mathrm{eff}} - 1)V_{\mathrm{DC\text{-}link}}, \tag{4.1}$$

$$V_{\mathrm{T_{boost}}} = \frac{V_{\mathrm{DEAP}} - V_{\mathrm{DC\text{-}link}}}{n_{\mathrm{eff}}} + V_{\mathrm{DC\text{-}link}}, \tag{4.2}$$

where n_{eff} is the effective turns ratio given by

$$n_{\mathrm{eff}} = n_{\mathrm{act}} + 1 \tag{4.3}$$

and n_{act} is the actual turns ratio.

It is now evident that the boost switch may be selected as a low-voltage device even for high-voltage applications. On the other hand, the increased voltage stress across the buck switch renders the selection of a high-voltage device for its realization inevitable. Selecting such a device for a high-voltage low-average current application, as a typical DEAP energy harvesting system, would quickly prove to be inefficient and thus impractical. Therefore, and in order to alleviate the need for a high-voltage switch, serialization of three (3) off-the-shelf 1200 V IXYS HiPerFET$^{\text{TM}}$MOSFETs (model IXFK20N120) was implemented using the revised gate balancing core technique introduced in a following subsection.

4.2.4 Serialization of switches

Several disciplines of modern power electronics necessitate for novel, fast-switching power semiconductor devices, which should be rated for high voltages while sustaining acceptable conduction losses. High-Voltage Direct-Current (HVDC) transmission networks, Flexible Alternating Current Transmission Systems (FACTS), high-voltage power supplies installed in radar modulators and X-ray generators, as well as propulsion inverters for high-speed rails and locomotives, are only few indicative applications leading that trend. Besides, commercially-available switches for such high-voltage, high-frequency applications are today limited to the relatively fast power-MOSFETs, rated up to few hundred volts, and the relatively slow IGBTs, rated up to few thousand volts.

Serialization of commercially-available solid-state devices has in several designs been proven to be an advantageous alternative in order to obtain such prominent switches. Unfortunately though, obtaining such a fast and high-efficient high-voltage switch is a laborious task. Indeed, stochastic deviations in the devices dynamic parameters, mismatches in their driving signals or - more realistically - a concurrence of both, will inevitably lead to an unequal transient as well as steady-state voltage sharing among the stacked switches. Additional design effort is thus required to balance the voltage distribution among the serialized devices during both their dynamic and static operational states.

Balancing resistors have been widely adopted to compensate for the unequal voltage distribution under steady-state operation, mainly due to their superior performance, in terms of cost, size and effectiveness. The transient voltage distribution on the other hand, has attracted a significant part of the scientific interest, due to the far more challenging mechanisms associated with its nature. Numerous stacking techniques have been proposed in the past, in order to overcome the dynamic voltage unbalance and thus render the efficient serialization of solid-state switches feasible. A primal classification of the fundamental stacking approaches separates them into two (2) major classes; namely the

load-side and the gate-side techniques.

The load-side class constitutes of the active and the passive techniques, which will either actively slow-down/speed-up and clamp the voltage of the fastest/slowest switch during turn-off/turn-on, or will passively control the voltage rate of change of each switch during both turn-on and turn-off transitions. Typically, the load-side active techniques demonstrate an acceptable dynamic performance, while protecting the switches from overvoltages, followed by an inevitable compromise between effectiveness and increased energy loss [**?**, **?**, **?**].

The load-side passive techniques on the other hand, reflect a highly attractive approach, as they only consist of few passive components; rendering their design relatively simple, adaptable and highly reliable. However, even though passive snubbers are robust circuits, demonstrating good transient voltage distribution, they experience high energy losses at high operating voltages, diminishing the energy efficiency of the converter [**?**, **?**, **?**]. An interesting hybrid technique, combining an active voltage clamp circuit with a passive snubber, in an effort to minimize both the device switching and snubber losses, was proposed in [**?**].

Contrarily, the gate-side techniques, further classified into the open-loop and the closed-loop techniques, will attempt to form the gate charge profile of the serialized devices, in order to effectively control their switching performance. The gate-side closed-loop techniques demonstrate very good transient voltage distribution among the stacked switches, without significantly increasing the overall energy loss, but they do so while increasing the cost and the complexity of the apparatus, as they introduce some high-speed, high-precision analogue/digital circuitry per stacked device [**?**, **?**].

The gate-side open-loop techniques are relatively simple approaches, compensating for mismatches in the driving signals caused by asynchronous delays, false triggering, EMI and/or unequal driver-gate impedance paths, based on a passive, magnetic or capacitive, coupling between the gate electrodes. Many of the gate-side open-loop techniques have demonstrated good dynamic performance, ensuring the transient voltage balancing among the stacked switches, without lengthening their commutation times and hence without introducing any kind of significant additional loss in the circuit [**?**, **?**].

Their main disadvantage however, is that they typically don't cope with the deviating parameters of the devices, which may affect their switching times without imposing an effect on the driving signals, as for example an unequal junction temperature distribution among the stacked devices. Among the predominant gate-side open-loop approaches lies the gate balancing core technique, which has demonstrated superior performance in high-power IGBT modules, by magnetically coupling their gate electrodes [**?**]. Furthermore, the gate balancing core technique has been successfully used to reduce the switching losses in high-voltage inverters [**?**] and auxiliary power supply systems [**?**].

4.2.4.1 The gate balancing core technique

The gate balancing core technique introduces $(n_{\mathrm{st}} - 1)$ transformers for n_{st} stacked switches, which form a magnetic coupling among all the power semiconductor devices gate electrodes. The primary and secondary windings of the cores, respectively denoted by L_{p} and L_{s}, characterized by a 1:1 turns ratio, are antithetically coupled and balancing resistors R_{B} are employed to achieve equal voltage sharing under steady-state conditions. A simplified schematic of the gate balancing core scheme, for the case of three (3) serialized MOSFETs is illustrated in Fig. 4.5, where it becomes apparent that the cores balance the currents flowing towards/against the gate electrodes, charging/discharging the input capacitances of the switches, ensuring a matched gate profile among them.

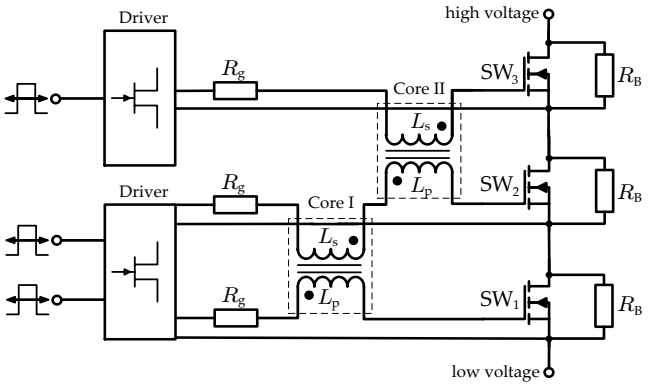

Figure 4.5: Simplified schematic of the gate balancing core technique for a MOSFET-based stacked string comprising of three (3) serialized devices.

According to [**?**], two are the main design specifications of the gate balancing core technique. The magnetizing inductance of the cores L_{m}, that should be designed based on the worst case scenario driving signals time delay ΔT_{on} that should be compensated for

$$L_{\mathrm{m}} \geq \frac{\Delta T_{\mathrm{on}}^2}{0.02 C_{ies}} \tag{4.4}$$

and the transformers leakage inductances, which should be designed to limit the damping ratio of the series RLC circuits, formed by the gate resistors R_{g}, the transformer leakage inductances L_{lk} and the input capacitance of the devices C_{ies}

$$\zeta = \frac{R_{\mathrm{g}}}{2}\sqrt{\frac{C_{ies}}{L_{\mathrm{lk}}}} \quad \text{for} \quad \zeta \leq 0.7 \tag{4.5}$$

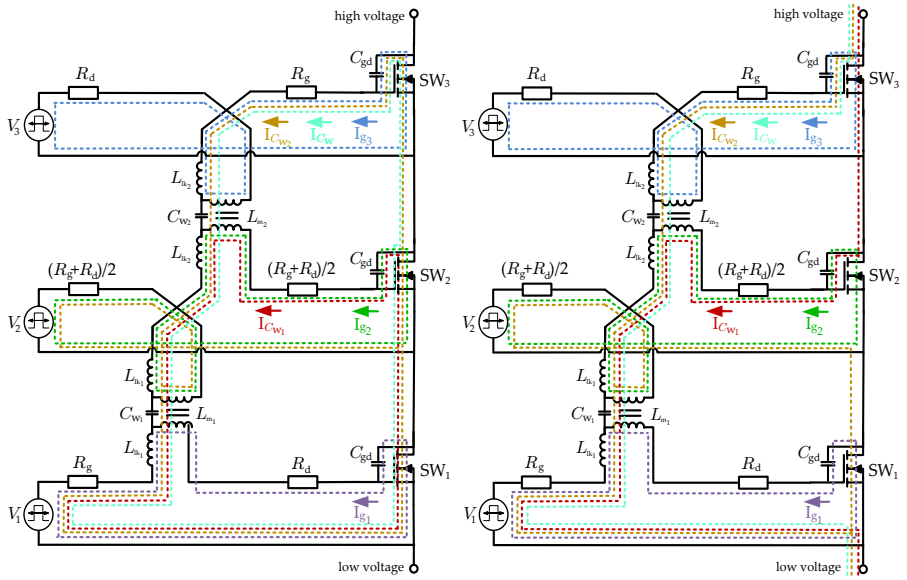

Figure 4.6: Interwinding capacitances and gate currents during (a) turn-on (b) turn-off for the case of three (3) stacked switches and two (2) non-identical gate balancing cores. Colour notation: I_{g_1} - magenta, I_{g_2} - green, I_{g_3} - blue, $I_{C_{w_1}}$ - red, $I_{C_{w_2}}$ - gold and I_{C_w} - light blue.

$$L_{lk} = \frac{R_g^2 C_{ies}}{1.96}. \tag{4.6}$$

However, as demonstrated in [?, ?] even if those two (2) design specifications proved sufficient for high-power IGBT modules driven by gate currents of several amperes, they are not adequate for low- and medium- power switches driven by few hundred milliamperes or less.

4.2.4.2 The revised gate balancing core technique

Distributed along each gate balancing core windings lies an interwinding capacitance, reflecting the inevitable parasitic capacitive coupling between them. These capacitances are, for illustration purposes, drawn in Fig. 4.6[1] as distinct lumped components, respectively denoted by C_{w_1} and C_{w_2}, within the transformers equivalent circuits. The MOSFETs gate currents, I_{g_1}, I_{g_2} and I_{g_3} are also drawn, side-by-side with the interwinding capacitance currents $I_{C_{w_1}}$ and $I_{C_{w_2}}$, for the general case of a serialized string comprising of three (3) serialized switches and two (2) non-identical gate balancing cores.

[1] For more information on the resistive components R_g and R_d placing consult [?, ?].

As straightforwardly concluded via Fig. 4.6 the interwinding capacitances C_{w_1} and C_{w_2} are effectively connected between the gate electrodes of two sequential MOSFETs and thus during the turn-off transition interval, depicted in Fig. 4.6(b) their are charged-up to approximately 33 % of the entire chain blocking voltage. Indeed, when the declining gate to source voltages of the serialized switches get clamped to the plateau voltage, the drain-to-source voltages across the MOSFETs start to built up charging the interwinding capacitances.

Afterwards, and whilst the devices are turned-off, the interwinding capacitances of the transformers remain charged until the turn-on transition of the MOSFETs commences. Eventually, when the respective plateau voltage is reached, the drain-to-source voltages of the switches start decaying and the interwinding capacitances get discharged through the newly formed paths, illustrated in Fig. 4.6(a). It is thus evident that the charging and discharging processes of the interwinding capacitances distort the gate current balance of the stacked MOSFETs during the switching transitions and thus they also distort their dynamic voltage distribution. Simulations of the schematic illustrated in Fig. 4.6, in Linear Technology Simulation Program with Integrated Circuit Emphasis (LTspiceIV®) verified that the interwinding capacitances current paths depend on the relation between the cores interwinding capacitances. Indicatively, during the turn-off switching transition three (3) different cases may occur:

$C_{\mathrm{w}_1} > C_{\mathrm{w}_2}$: A current $I_{C_{\mathrm{w}}}$ enters the chain via its high-voltage node, flows through the Miller capacitance C_{gd} of the upper switch SW_3 and subsequently charges both interwinding capacitances C_{w_2} and C_{w_1}, before exiting through the low-voltage node of the string. The current $I_{C_{\mathrm{w}}}$ is denoted in Fig. 4.6(b) by light blue colour. In addition, an extra current component $I_{C_{\mathrm{w}_1}}$ enters the string through the Miller capacitance of the intermediate switch SW_2, charges the interwinding capacitance C_{w_1} and exits through the low-voltage node of the string as well. The current $I_{C_{\mathrm{w}_1}}$ is depicted in Fig. 4.6(b) in red.

$C_{\mathrm{w}_1} < C_{\mathrm{w}_2}$: A current $I_{C_{\mathrm{w}_2}}$ enters the chain via its high-voltage node, flows through the interwinding capacitance C_{w_2} and then splits into one component flowing through the interwinding capacitance C_{w_1} and another component flowing through the driving circuit loop of the intermediate switch, before exiting the string through the bottom switch SW_1. The current $I_{C_{\mathrm{w}_2}}$ is denoted in Fig. 4.6(b) by golden colour.

$C_{\mathrm{w}_1} = C_{\mathrm{w}_2} = C_{\mathrm{w}}$: The current flow $I_{C_{\mathrm{w}_1}}$ and $I_{C_{\mathrm{w}_2}}$, through the interwinding capacitances C_{w_1} and C_{w_2} respectively, is a function of the capacitances themselves and their respective voltage rate of change $\dot{V}_{C_{\mathrm{w}_1}}$ and $\dot{V}_{C_{\mathrm{w}_2}}$

$$I_{C_{\mathrm{w}_1}} = C_{\mathrm{w}_1}\dot{V}_{C_{\mathrm{w}_1}}, \tag{4.7}$$

$$I_{C_{\mathrm{w}_2}} = C_{\mathrm{w}_2}\dot{V}_{C_{\mathrm{w}_2}}. \tag{4.8}$$

Assuming a synchronized string, consistency of (4.7) and (4.8) dictates that

$$I_{C_{w_1}} = I_{C_{w_2}} = I_{C_w} = C_w \dot{V}_{C_w}. \tag{4.9}$$

A similar analysis may be conducted for the turn-on transition of the serialized chain and the respective current paths are drawn in Fig. 4.6(a). As thoroughly described in [**?**], while the gate-to-source voltage V_{gs} of a switch is being clamped, its entire gate current flows through the device Miller capacitance. Hence, denoting with V_{pl} the level of the plateau voltage, with V_{cc} the amplitude of the synchronized driving signals and with $\dot{V}_{ds}$ the time derivative of the switches drain-to-source voltage, the balanced gate current I_g of the stacked devices, when it is $V_{gs} = V_{pl}$, can be approximated by

$$I_{g_{\text{on-off}}} = \frac{V_{cc} - V_{pl}}{R_g} = C_{gd_{\text{on-off}}} \dot{V}_{ds_{\text{on-off}}}. \tag{4.10}$$

Therefore, the interwinding capacitances C_w of the transformers can be designed with respect to the MOSFET Miller capacitance C_{gd} for an aimed relation between their current I_{C_w} and the balanced gate current I_g

$$I_{C_{w,\text{on-off}}} \leq x\ \%\ I_{g_{\text{on-off}}} \iff \frac{C_w}{C_{gd_{\text{on-off}}}} \leq x\ \%. \tag{4.11}$$

The top layer of the non-isolated bidirectional tapped-inductor buck-boost converter prototype, with direct emphasis on the serialized chain and its gate balancing core driving circuit components, is graphically illustrated in Fig. 4.7.

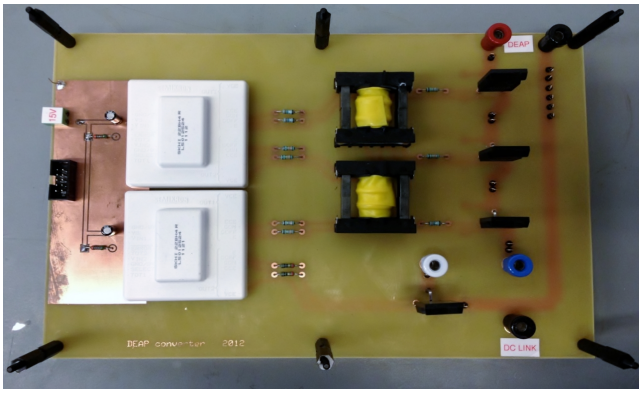

Figure 4.7: Graphical illustration of the tapped-inductor buck-boost converter prototype.

4.3 Experimental results

In the following subsections a set of essential, towards a comprehensive characterization of demo#1, experiments is presented. At first, all DEAP generators are installed and independently characterized on the mechanical test rig of horizontal demo#0. Subsequently, the bidirectional tapped-inductor buck-boost converter is characterized by means of energy efficiency, following the procedure described in subsection 3.3.2. The performance of its serialized chain is assessed separately. Finally, all DEAP generators are installed in demo#1 and numerous energy harvesting experiments are conducted. Focus is given on the experiments that illuminate the most essential scientific findings.

4.3.1 DEAP generator characterization

All DEAP generators were individually characterized using the standalone test rig depicted in Fig. 4.2. In order to attain a sinusoidal-like deformation curve every DEAP generator was pre-stretched by 5.5 %, leading to a capacitance increase from 1.0 uF to 1.07 uF; indicating that $\kappa = 1.2$. The Vishay® LVDT was calibrated to report zero displacement at the 5.5 % position, while the Tedea® load cell was configured to report zero force when no element was installed in the rig. In that way, both the DEAP generator buckling effect and the respective force signal saturation at relatively low strains were overcome.

The NI-cDAQ™ 9178 chassis was configured to record synchronized data of DEAP force and displacement at a 500 S/s sampling rate. Figures 4.8(a) and 4.8(b) illustrate the progression of a DEAP generator acquired force and displacement signals under a 60 % delta-strain cycle at 0.5 Hz. On the other hand, Figs. 4.8(c) and 4.8(d) respectively display the DEAP generator mechanical potential energy and its hysteresis loop. The DEAP generator capacitance, at maximum strain position, was measured equal to 1.85 uF. The test rig average mechanical input energy, coinciding with the average mechanical potential energy of the DEAP generator, whose characteristics are seen in Fig. 4.8, was found equal to 104 J. The latter one's effective mechanical potential energy however was only 5.7 J and its mechanical efficiency was found equal to 94.2 %.

All examined DEAP generators demonstrated similar force-displacement characteristics and thus they were subsequently installed in the quadruple test rig. The NI-cDAQ™ 9178 chassis was configured to record synchronized data of the angular position and moment of force at the gearbox output at a 5 kS/s sampling rate. Figures 4.8(e) and 4.8(f) illustrate the respective data, as they were recorded during a 0.5 Hz and 60 % delta-strain experiment, during which all four (4) similarly-sized DEAP generators were installed in the quadruple rig.

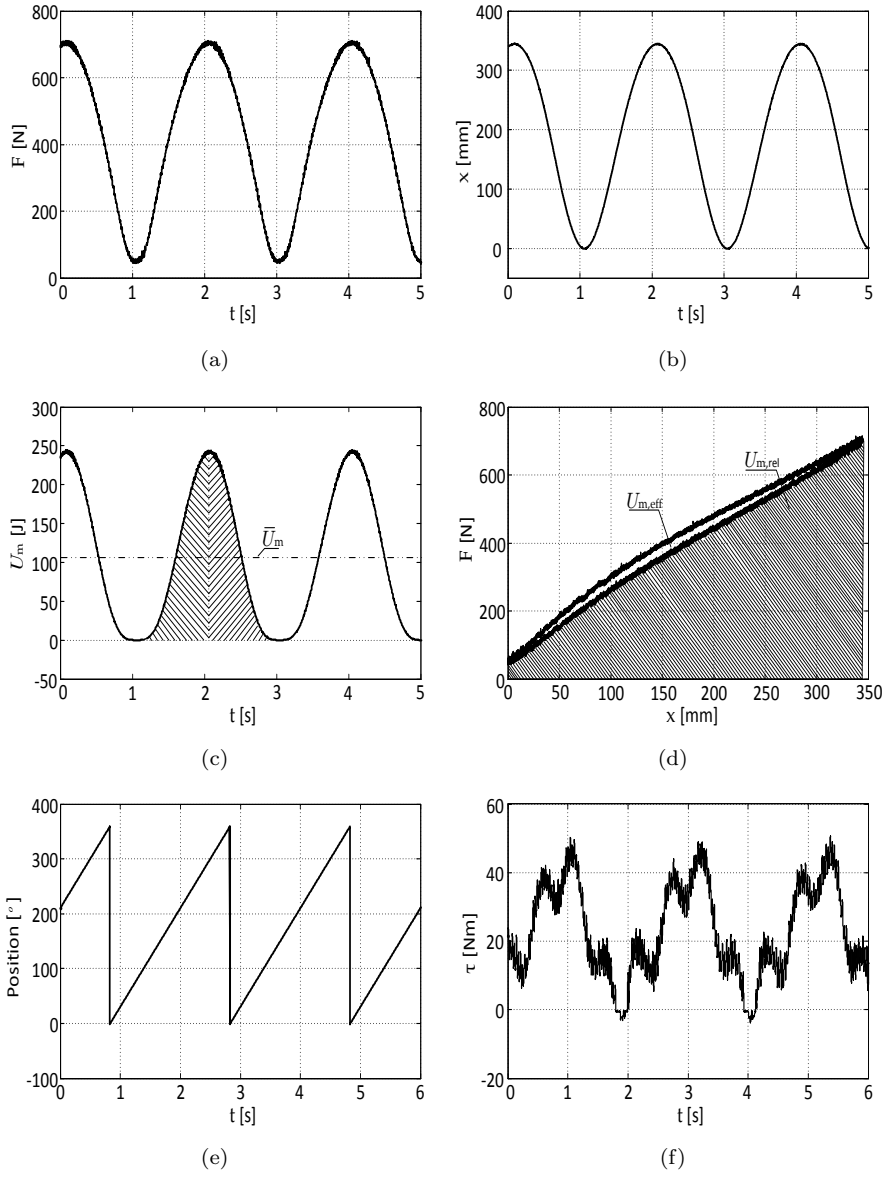

Figure 4.8: DEAP generator progression of (a) force (b) displacement (c) mechanical potential energy over time and (d) force-strain curve for a 60 % delta-strain cycle at 0.5 Hz. Recorded data of the (e) relative angular position and (f) torque signal in the gearbox output during a 0.5 Hz and 60 % delta-strain experiment conducted on the quadruple test rig.

Assuming n_s samples for an entire cycle, the average mechanical input energy of the quadruple test rig is determined by,

$$\bar{U}_{m,\mathrm{quad}} = \frac{1}{n_\mathrm{s}} \sum_{k=1}^{n_\mathrm{s}} \tau[k]\omega[k] \tag{4.12}$$

where τ and ω denote the torque and angular velocity data respectively.

For the 60 % delta-strain experiment, described by Figs. 4.8(e) and 4.8(f), the quadruple test rig average mechanical input energy was found equal to 54.9 J. It is thus evident, that even though 416 J would be needed to individually cycle all DEAP generators using four (4) standalone mechanical test rigs, as the one seen in Fig. 4.2, doing so on the quadruple DEAP generator system, depicted in Fig. 4.1, where all elements are sequentially installed with a 90 ^{o} phase shift, would only demand 54.9 J; reflecting an 86.8 % decrease in the mechanical input energy of the system, or seen from a different perspective, a respective increase in the utilization factor of the infrastructure input mechanical energy.

4.3.2 Power electronic converter characterization

Serialization of three (3) off-the-shelf 1200 V IXYS HiPerFET$^{\mathrm{TM}}$MOSFETs (model IXFK20N120) was realized, using the revised gate balancing core technique, leading to the converter schematic seen in Fig. 4.9. Three (3) different snubbers (S_b where $b = 1, 2, 3$) were designed to enhance the operation of the converter. The RCD snubber S_1 (R_1 = 11 MOhm, C_1 = 1 uF) suppresses the overvoltages across the boost switch T_{boost}, caused by the interrupted current flowing through the primary leakage inductance $L_{\mathrm{p_{lk}}}$. Similarly the second RCD snubber S_2 (R_2 = 6.5 MOhm, C_2 = 1 nF) suppresses the overvoltages across the stacked MOSFETs, due to the interrupted current flowing through the secondary leakage inductance $L_{\mathrm{s_{lk}}}$. Finally, the RC snubber S_3 (R_3 = 1 kOhm, C_3 = 1 nF) absorbs the oscillations between the overall tapped

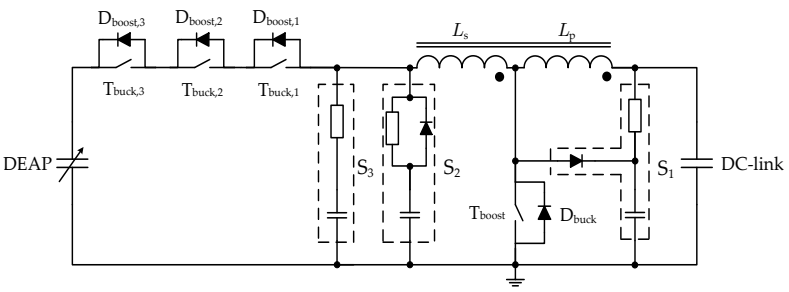

Figure 4.9: Schematic of the bidirectional tapped-inductor buck-boost converter.

inductance, denoted by L, and the serialized chain equivalent off-capacitance. Table 4.2 summarizes all fundamental parameters of the custom-made inductor. Four (4) Powerlite® C-cores (part AMCC-400), manufactured with iron-

Table 4.2: Tapped-inductor parameters.

Parameter	Value
Effective turns ratio n_{eff}	3
Primary inductance L_{p}	15 mH
Primary leakage $L_{\text{p}_{\text{lk}}}$	70 uH
Secondary inductance L_{s}	60 mH
Secondary leakage $L_{\text{s}_{\text{lk}}}$	270 uH
Overall tapped-inductance L	130 mH

based Metglas® amorphous alloy SA1, were used to form the tapped-inductance core. Furukawa® triple-insulated wire (TEX-E series) was employed to form both tapped-inductance windings.

4.3.2.1 Energy efficiency mapping

The prototype operated in open-loop mode and therefore a precise model of its buck and boost functions was designed in MATLAB®, from which the duty cycle, switching frequency and number of pulses could be determined, based

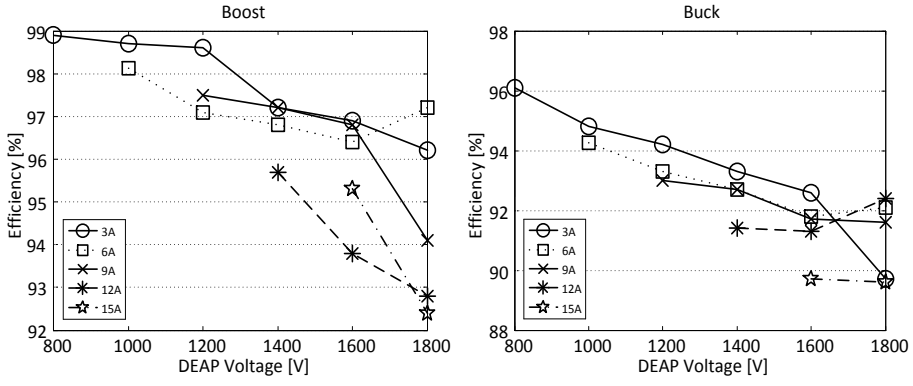

(a) (b)

Figure 4.10: Energy efficiency map of the tapped-inductor buck-boost prototype (a) boost and (b) buck functions for various DEAP voltages and primary-side peak-current references.

on the desired DEAP voltage level and primary-side peak-current value. The energy efficiency map of the prototype was estimated by loading both its input and output ports capacitively, redesigning the pseudo-DEAP capacitance as 2.26 uF. Figure 4.10 illustrates the energy efficiency maps of the buck and boost functions of the prototype as functions of the pseudo-DEAP voltage for different primary peak-current values. The DC-link voltage was set to 400 V and the pseudo-DEAP load was discharged to 500 V after every buck function.

It is now evident that the boost function of the prototype is more efficient than the respective buck function. Yet, as the converter operated with fixed duty cycle and fixed switching frequency, it is also clear that the primary-side peak-current reference for the buck function was only valid for the first pulse; leading to an inefficient surplus of pulses. On the other hand, during the boost function, and as the DC-link voltage remained relatively constant, the primary-side peak-current reference was practically met by all prescribed driving pulses.

4.3.2.2 Serialized switches

Aiming towards the effective serialization of the three (3) off-the-shelf 1200 V IXYS HiPerFET^{TM}MOSFETs (model IXFK20N120) in the prototype seen in Fig. 4.7, two (2) gate balancing transformers were winded, using ETD29 cores (N97 material) and Furukawa® triple-insulated wire (TEX-E series). Table 5.3 displays the main parameters of the prototype driving circuit, where R'_{g} denotes the overall gate resistance, i.e. $R'_{\mathrm{g}} = R_{\mathrm{g}}+R_{\mathrm{d}}$.

Table 4.3: Prototype driving circuit parameters.

Parameter	Value
Total gate resistance R'_{g}	27 Ohm
Leakage inductance L_{lk}	2.5 uH
Magnetizing inductance L_{m}	160 uH
Interwinding capacitance C_{w}	0.1 pF
MOSFET input capacitance C_{ies}	7.4 nF
Steady-state balancing resistor R_{B}	6.8 MOhm

During the prototype energy efficiency mapping the primary-side peak-current was limited to 15 A for both buck and boost functions to avoid saturation of the tapped-inductance core. The pseudo-DEAP voltage, on the other hand, was limited by the breakdown voltage of the serialized switches. Indeed, as seen in Fig. 4.11(a)[2], during the buck function, and while the pseudo-DEAP

[2]For more information on the revised gate balancing core performance consult [?, ?].

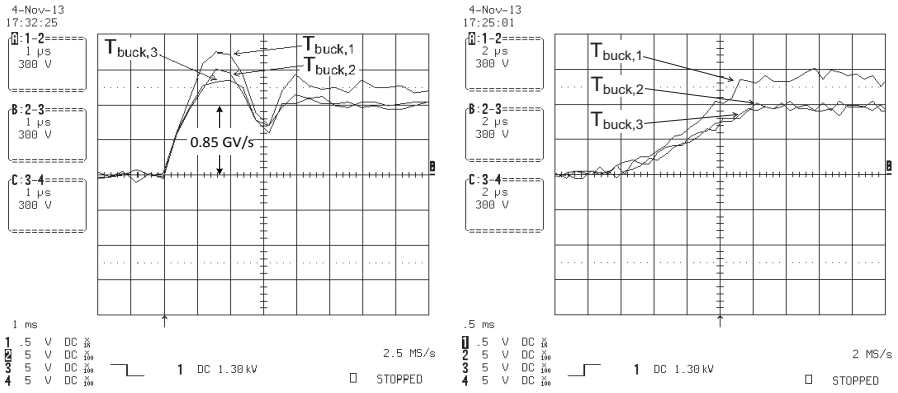

(a) (b)

Figure 4.11: Blocking voltages of the serialized switches at their (a) turn-off transient period during a buck function (b) diode turn-off transient period during a boost function, as they were recorded by pseudo-differential measurements conducted via high-bandwidth high-voltage PPE LeCroy$^{\mathrm{TM}}$ probes ($V_{\mathrm{DEAP}} = 1800$ V and $I_{L_{\mathrm{s,peak}}} = 4$ A).

voltage was 1800 V and the secondary peak-current was 4 A, the drain-to-source voltage across the switch turning-off faster, i.e. $\mathrm{T}_{\mathrm{buck},1}$, approached the detrimental 1200 V. Yet, according to (4.1) the overall steady-state blocking voltage across the stacked switches was 2600 V and the transient overvoltage can be estimated, by Fig. 4.11(a), as 2900 V, verifying the string effectiveness.

Figure 4.11(b) illustrates that during the respective boost operation the drain-to-source voltage across the switch turning-off faster, i.e. $\mathrm{T}_{\mathrm{buck},1}$, did not exceed 900 V. The transient voltage overshoot during the turn-off transition is thereby time-dependent, indicating that it may be caused by parasitic capacitances formed between the switches drain electrodes and the common ground. The effects imposed by parasitic capacitances, plausibly-placed in the driving and the power circuits, were thoroughly investigated, in [**?**], and a self-powering technique for the driving circuit, along with a vertical power circuit design structure, was proposed to attenuate them. Nonetheless, as the recorded overshoot between the fastest and the slowest switch, during the buck function, reflected only 10 % of the steady-state blocking voltage, and all drain-to-source voltages seemed to ascent synchronously, no further design effort was considered necessary prior to conducting demo#1 energy harvesting experiments.

4.3.3 Energy harvesting

Numerous energy harvesting experiments were conducted in both horizontal demo#0 and demo#1. As the prototype operated in open-loop mode, only CC

cycles were able to be formed, using as a triggering source either the Vishay® LVDT or the SICK encoder. In either case, and in consistency with Fig. 4.11(a), all experiments were terminated when the DEAP voltage, monitored via a very high-impedance voltage divider, reached 1800 V at relaxed-state, i.e. 30 V/um. The primary-side peak-current reference was set to 9 A during both buck and boost converter functions. The energy gain formula was now updated to account, besides the probe loss, the voltage divider loss as well. Table 4.4 summarizes demo#0 and demo#1 key energy harvesting experiments parameters.

Table 4.4: Demo#0 and demo#1 key energy harvesting experiments parameters.

Parameter	Demo#0	Demo#1
Delta-strain	60 %	60 %
Cycling frequency f	0.75 Hz	0.5 Hz
Geometrical constant α	0.76	0.76
Maximum attainable E-field $E_{\max}$	29 V/um	29.7 V/um

Figure 4.12 illustrates the progression of the DEAP generator voltage over time during a 60 % delta-strain at 0.75 Hz experiment conducted on horizontal demo#0. As anticipated for an isolated DEAP energy harvesting system, the converter of which operated with fixed switching frequencies and duty cycles for a prescribed number of pulses, the average voltage of the DEAP generator in a number of consecutive CC cycles increased; as so did the DC-link voltage.

Indeed, the respective progression of the DC-link voltage is depicted in Fig. 4.13.

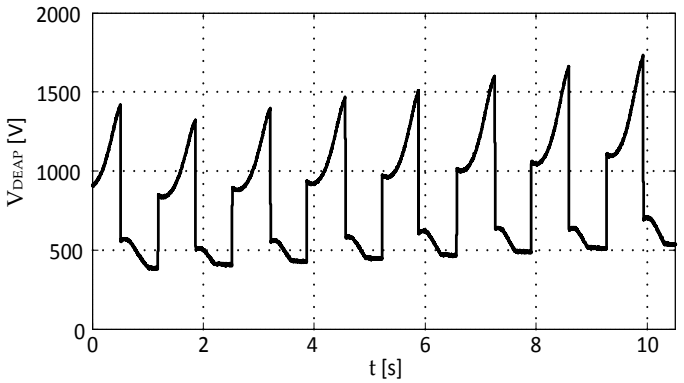

Figure 4.12: DEAP voltage time progression during a 60 % delta-strain at 0.75 Hz energy harvesting experiment conducted on horizontal demo#0.

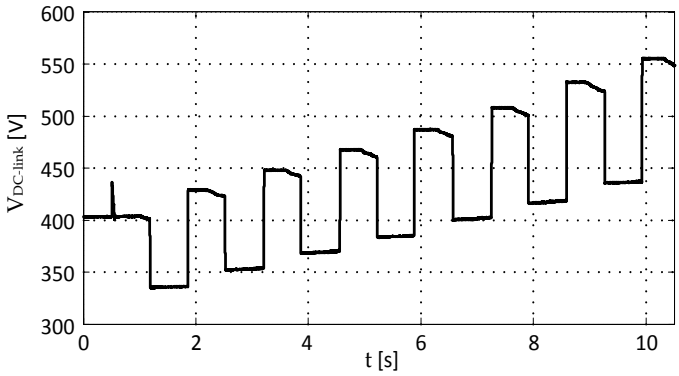

Figure 4.13: DC-link voltage time progression during a 60 % delta-strain at 0.75 Hz energy harvesting experiment conducted on horizontal demo#0.

As it is straightforwardly concluded energy was successfully harvested after the completion of every cycle as the DC-link voltage increased gradually over time. On the other hand, as the DC-link capacitance was relatively low, i.e. 24.2 uF, to increase the sensitivity of (3.6), a small voltage drop during the DEAP stretching phase can also be appreciated. More importantly though, the DEAP generator appears to have been leaking, during its relaxation phase, to the DC-link, as the voltage of the latter one during that period was slightly increased.

Table 4.5: Demo#0 and demo#1 energy harvesting experiments outcome.

Parameter	Demo#0	Demo#1
Energy gain ΔU	0.42 J	0.26 J
Absolute energy gain $\Delta U_{\mathrm{CC,abs}}$	0.94 J	0.99 J
Energy conversion efficiency η_{con}	7 %	4.6 %
Energy harvesting cycle efficiency η_{cycle}	44.7 %	27 %
Effective mechanical potential energy $U_{\mathrm{m,eff}}$	6 J	5.7 J

Assuredly, as seen in both Figs 4.12 and 4.13, after the boost function of the converter and while the DEAP sheets were relaxing, the generator was leaking through the steady-state balancing resistors to the DC-link; the voltage of which was slightly increasing. This DC-leakage, reflecting an inherent limitation, of the bidirectional tapped-inductor buck-boost converter, based on a serialized chain of off-the-shelf MOSFETs, which demand the installation of balancing resistors across their terminals to equalize the steady-state voltage

distribution among them, diminishes the potential energy gain of the DEAP generator, for the given amount of energy being transferred during the boost function of the converter. Nevertheless, maximization of the steady-state balancing resistors led to the results presented in Figs 4.12 and 4.13. Table 4.5 summarizes the best documented results of a single cycle during the energy harvesting experiments conducted on both horizontal demo#0 and demo#1.

Even though the tapped-inductor buck-boost converter is characterized by high energy efficiency, cf. Fig. 4.10, still the need of cycling great amounts of reactive energy during a CC cycle renders the power electronic converter a rather lossy component of the energy harvesting system. Indeed, as the boost function of the converter, during the horizontal demo#0 experiment, stepped-up the voltage of the stretched generator from 510 V to 1100 V with 93 % energy efficiency and the buck function of the converter stepped-down the voltage of the relaxed DEAP generator from 1730 V to 690 V with 95.5 % energy efficiency, the overall converter loss can be estimated to have been equal to 0.12 J; indicating the importance of a very high energy efficient power electronic converter. Yet, the energy density of the respective experiment can be estimated as 2 J per kilogram of active material, which was - at date - a world-first for an active power electronic converter coupled to such a sizeable DEAP generator.

4.4 Summary

This chapter introduced the second complete DEAP generator energy harvesting system, i.e. demo#1, as well as an auxiliary one, i.e. horizontal demo#0. All DEAP generators were independently characterized using the mechanical test rig of horizontal demo#0, prior to their installation in demo#1 rig. The power electronic converter was assessed by means of energy efficiency, while the performance of its MOSFET-based string was evaluated separately. Finally, numerous energy harvesting experiments were conducted in both demonstrators achieving maximum energy generation of 2 J/kg of active material.

This page is intentionally left blank

This page is intentionally left blank

Chapter 5

Experiences with Demo#2

5.1 Introduction

This chapter introduces demo#2 and outlines all acquired knowledge and experience associated with its use during the period from mid-2014 to mid-2015. The prime kick-off goal of the demonstrator was to display higher energy gain in regard to demo#1, by driving a voluminous DEAP generator at high E-field strengths, via an updated bidirectional tapped-inductor buck-boost converter. The secondary goal of demo#2 was to reassess all distinct energy harvesting cycles, by means of energy gain, energy harvesting efficiency and energy conversion efficiency; capitalizing the accumulated experience from demonstrator#0.

5.2 Demo#2 description

Demo#2 consisted of the same mechanical test rigs as demo#1, enabling the individual cycling of a standalone generator as well as the out-of-phase co-cycling of up to four (4) DEAP generators under various frequencies and stretch configurations. On the power electronics side, demo#2 employed a new bidirectional tapped-inductor buck-boost converter, integrating the highly efficient design of demo#1 with the highly reliable control platform of demo#0. The converter SOA was enhanced, by replacing the 1200 V IXYS HiPerFET^{TM}IXFK20N120 MOSFETs with the 1500 V IXTX20N150 High Voltage Power MOSFETs with extended SOA, which allowed the selection of larger steady-state balancing resistors, attenuating the inherent DC-leakage limitation of the serialized chain.

5.2.1 DEAP generator

Danfoss PolyPower® A/S supplied AAU with two (2) DEAP generators to be used with demo#2. The DEAP generators detailed technical drawing is presented in Fig. 5.1(a). Each generator comprised of two (2) front-to-back laminated elastomer films, which were rolled-up forming a ring-shaped structure as seen in Fig. 5.1(b). Each single-layer film relaxed-state length and width dimensions were $l_x^{(0)} = 100$ m and $l_y^{(0)} = 160$ mm respectively. The relaxed-state thickness, however, was $d_z^{(0)} = 53$ um for one of the designs and $d_z^{(0)} = 74$ um for the other, resulting into two (2) different relaxed-state capacitance values.

Table 5.1: Demo#2 DEAP generators relaxed-state characteristics (1st iteration).

Characteristic	Value
Mass m	0.93 kg / 1.3 kg
Capacitance $C^{(0)}$	9 uF / 5.25 uF
Serial resistance R_{serial}	5 Ohm / 1 Ohm
Parallel resistance R_{parallel}	10 GOhm
Rated E-field strength E_{rated}	60 V/um

Table 5.1 outlines the DEAP generators relaxed-state characteristics; elastomer density and relative permittivity are omitted as they remain as in Table 3.1.

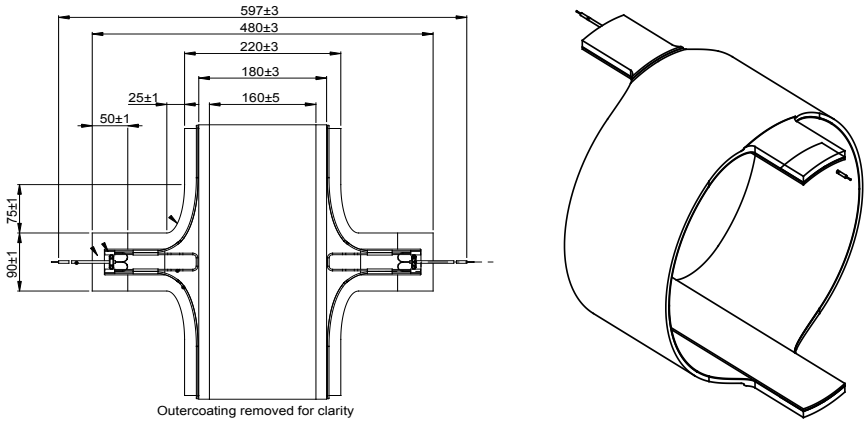

(a) (b)

Figure 5.1: DEAP generator (a) technical drawing and (b) schematic (1st iteration).

Unfortunately, both these voluminous generators experienced destructive electrical breakdowns, in relatively low operating E-field strengths, i.e. ≈ 20 V/um, and they were thus rendered inoperative. Extensive research showed that the probability of an electrical breakdown within the polymer material increases along with the area of the active film and thus new, smaller scale and back-to-back laminated DEAP generators were designed to be used with demo#2 [**?**]. The new generators technical drawing and schematic are respectively illustrated in Figs. 5.2(a) and 5.2(b). Each single-layer film relaxed-state dimensions were $l_x^{(0)} = 25$ m, $l_y^{(0)} = 160$ mm and $d_z^{(0)} = 87$ um.

Table 5.2: Demo#2 DEAP generators relaxed-state characteristics (2^{nd} iteration).

Characteristic	Value
Mass m	0.46 kg
Capacitance $C^{(0)}$	450 nF
Serial resistance R_{serial}	4 Ohm
Parallel resistance R_{parallel}	10 GOhm
Rated E-field strength E_{rated}	60 V/um

Table 5.2 outlines the DEAP generators relaxed-state characteristics; elastomer density and relative permittivity are omitted as they remain as in Table 3.1.

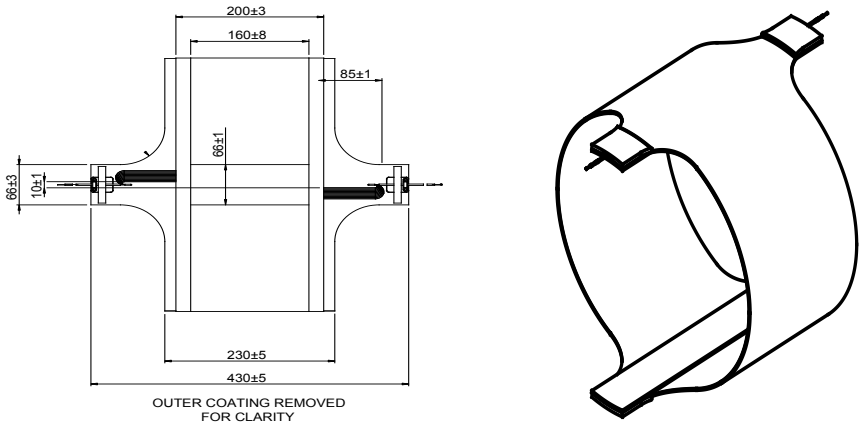

(a) (b)

Figure 5.2: DEAP generator (a) technical drawing and (b) schematic (2^{nd} iteration).

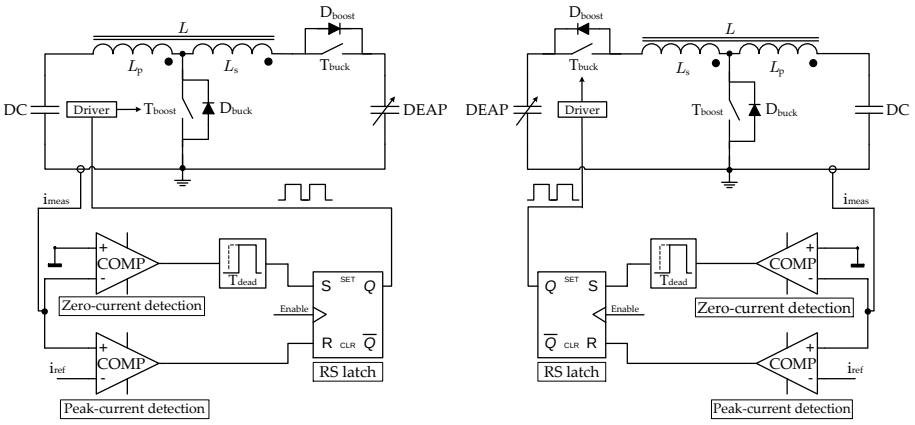

Figure 5.3: Analogue peak-current controller schematic for the (a) boost (b) buck function.

5.2.2 Power electronic converter

The highly reliable control platform of the half-bridge buck-boost converter designed in demo#0 was integrated with the highly efficient tapped-inductor buck-boost converter designed in demo#1 leading to the converter design used in demo#2. In an effort to extend the operational voltage range of the demo#2 converter, the 1200 V IXYS HiPerFET^{TM}IXFK20N120 MOSFETs employed in demo#1 were substituted by the 1500 V IXTX20N150 High Voltage Power MOSFETs, which in turn allowed for the steady-state balancing resistors to be stepped-up, attenuating the inherent DC-leakage limitation of the serialized chain which penalized the potential energy gain of a DEAP generator.

The operation of the converter was based upon the real-time position feedback provided by the LVDT/encoder and its control comprised of two interrelated loops. The main control loop was monitoring the DEAP voltage, during both buck and boost converter functions, while the ancillary control loop was configuring the peak-value of the current flowing through the tapped-inductor. Several auxiliary protection circuits were designed, latching the converter into fault mode, including DEAP and DC-link overvoltage, DC-link undervoltage, DEAP and DC-link overcurrent and MOSFET case temperature monitoring.

5.2.2.1 Analogue peak-current control

Figure 5.3 depicts the analogue peak-current controller designed to accommodate the operation of the tapped-inductor converter buck and boost functions.

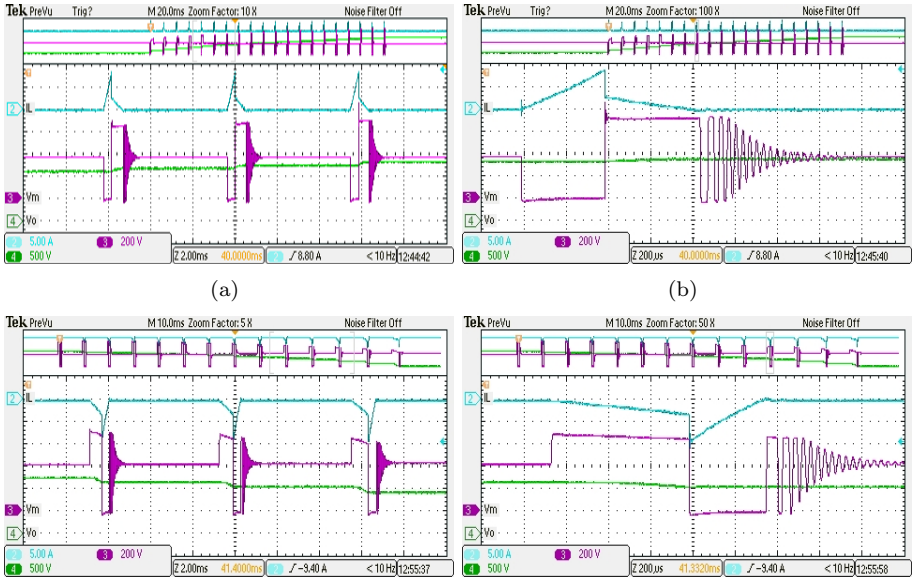

Figure 5.4: Boosting load voltage to 2000 V by 9 A current pulses (a) normal (b) zoomed view. Bucking load voltage from 2000 V by 3 A current pulses (c) normal (d) zoomed view.

The operational principle is identical to the one presented in subsection 3.2.3.1. To increase the robustness of the controller, the RC circuit used in demo#0, introducing a fixed-time delay in the driving pulses, was replaced, in demo#2, by a dead time insertion circuit, comprising of an RC branch, in high-pass filter configuration, and a TI XOR logical gate (model SN74LVC1G86DBVR). Alternation between DCM and BCM was achieved by bypassing the XOR gate.

Figure 5.4 illustrates the operation of the converter under DCM as it was recorded via a Tektronix® oscilloscope (model DPO2014). More specifically, Figures 5.4(a) and 5.4(b) present the operation of the converter boost function, while the load voltage was boosted from 500 V to 2000 V by 9 A primary-side current pulses. Accordingly, Figs. 5.4(c) and 5.4(d) depict the operation of the converter buck function, while the load voltage was bucked from 2000 V to 500 V by 3 A secondary-side current pulses. In all cases, the tapped-inductor current is displayed on channel two (2), the drain-to-source voltage of the T_{boost} switch on channel three (3) and the load voltage on channel four (4).

The peak-current controller operation is now proficient during both buck and boost functions of the converter, as the DC-link voltage, i.e. 400 V, and the inductances of the magnetic element, i.e. $L_p = 15$ mH and $L = 130$ mH result in relative long turn-on times for both T_{boost} and T_{buck} transistors, minimizing

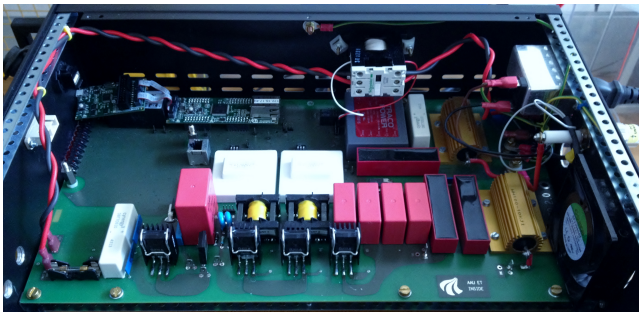

Figure 5.5: Graphical illustration of the bidirectional tapped-inductor buck-boost converter.

the influence of the integrated circuits propagation delays on the peak-current controller accuracy. Indeed, the ratio between the boost and buck functions turn-on times, assuming similar peak-current references, while omitting voltage drops in the converter active/passive components as in (3.1), is now

$$\frac{t_{\text{boost,on}}}{t_{\text{buck,on}}} = \frac{L_p}{L}\left(\frac{V_{\text{DEAP}}}{V_{\text{DC-link}}} - 1\right). \tag{5.1}$$

Figure 5.5 illustrates the top layer of the tapped-inductor buck-boost converter.

5.3 Experimental results

In the following subsections, and in proportion to section 4.3, a set of essential, towards the complete characterization of demo#2, experiments is presented. At first, all DEAP generators are independently characterized in the horizontal demo#0 mechanical test rig. Subsequently, the tapped-inductor buck-boost converter is characterized, following the procedure described in subsection 3.3.2. The performance of the redesigned serialized chain is assessed separately. Finally, numerous energy harvesting experiments are conducted in demo#2 on a viable DEAP generator and their most significant findings are duly highlighted.

5.3.1 DEAP generator characterization

All DEAP generators were individually characterized using the standalone test rig depicted in Fig. 4.2. In order to attain a sinusoidal-like deformation curve every DEAP generator was pre-stretched by 5.5 %, leading to a capacitance increase from 395 nF to 420 nF; indicating that κ is again 1.2. The Vishay® LVDT was calibrated to report zero displacement at the exact 5.5 % position, while the Tedea® load cell was once more configured to report zero force when

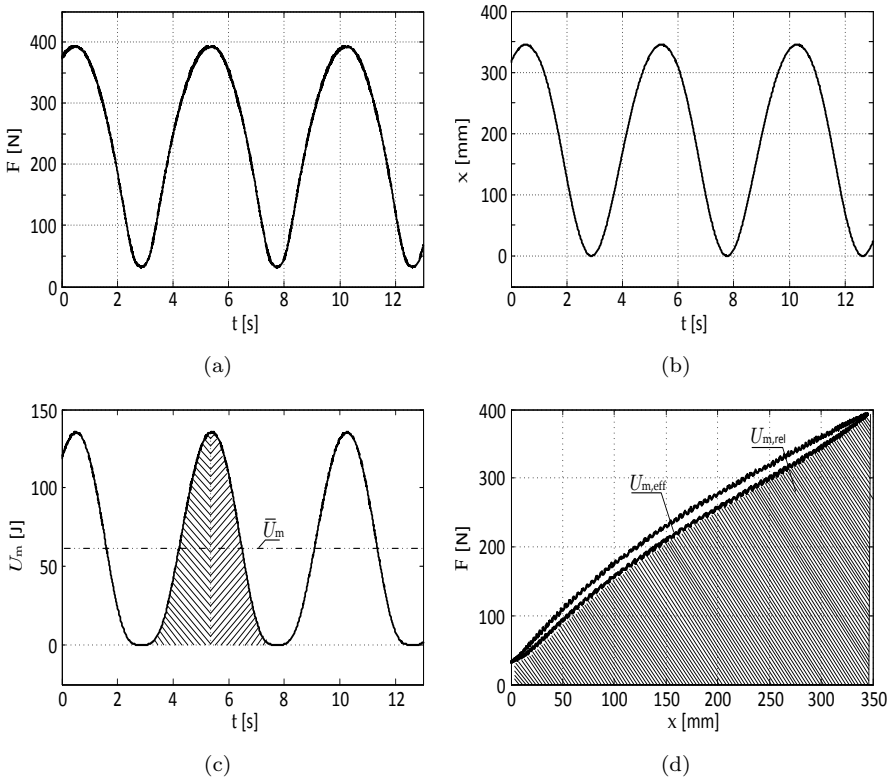

Figure 5.6: DEAP generator progression of (a) force (b) displacement (c) mechanical potential energy over time and (d) force-strain curve for a 60 % delta-strain cycle at 0.2 Hz.

no element was installed in the rig, following the standards of demonstrator#1. The NI-cDAQ™ 9178 chassis was again configured to record synchronized data of DEAP force and displacement at a 500 S/s sampling rate. Figures 4.8(a) and 4.8(b) illustrate the progression of the acquired force and displacement signals of a DEAP generator for a 60 % delta-strain cycle at 0.2 Hz. Figure 4.8(c) depicts the corresponding mechanical potential energy of that DEAP generator and Fig. 4.8(d) displays its hysteresis loop. As anticipated, the two (2) similarly-sized DEAP generators, reported identical force-displacement characteristics.

At maximum strain position the DEAP generator capacitance was measured equal to 780 nF. The test rig average mechanical input energy, coinciding with the average mechanical potential energy of the DEAP generator, whose characteristics are seen in Fig. 5.6, was found equal to 60 J. The latter one's effective mechanical potential energy, during this merely mechanical test at 60 % delta-strain and 0.2 Hz, was 5.7 J corresponding to a 93.3 % mechanical efficiency.

5.3.2 Power electronic converter characterization

Demo#2 tapped-inductor buck-boost converter was originally designed to drive the voluminous DEAP generators presented in Table 5.1. Upon the latter ones' defectiveness however, the converter was reconfigured to drive the viable DEAP generators presented in Table 5.2 instead. Yet, and as during the reconfiguration of the converter its operational current range was significantly penalized, as the tapped-inductor was not redesigned, the converter was characterized by means of energy efficiency assuming an available voluminous DEAP generator.

5.3.2.1 Energy efficiency mapping

The energy efficiency map of the converter was estimated by loading both its input and output ports capacitively, just as in subsection 3.3.2, redesigning the pseudo-DEAP capacitance as 9 uF. A 12-bit HDO6104 LeCroy^{TM} oscilloscope was employed to increase the accuracy of the energy efficiency estimation. Figures 5.7(a) and 5.7(b) illustrate the energy efficiency maps of the boost and buck functions of the converter respectively, as functions of the pseudo-DEAP voltage for different primary-side peak-current values. The DC-link voltage was 400 V and the pseudo-DEAP was discharged to 500 V after every buck function.

It is once more evident that the buck function of the converter is more energy efficient than the respective boost function. Indeed, while bucking, the converter operates with energy efficiency above 94 % for a wide range of operational voltages and primary-side peak-current references, whilst during boosting the converter efficiency lies around 92 % in the corresponding operational points.

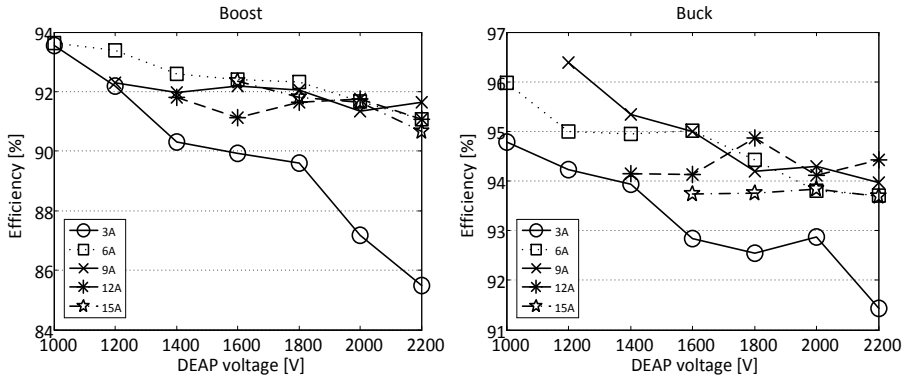

Figure 5.7: Energy efficiency map of the tapped-inductor buck-boost converter (a) boost and (b) buck functions for various DEAP voltages and primary-side peak-current references.

5.3.2.2 Serialized switches

Aiming towards the effective serialization of three (3) off-the-shelf 1500 V IXTX20N150 MOSFETs, two (2) gate balancing transformers were winded, using ETD29 cores (N87 material) and Furukawa® triple-insulated wire (TEX-E series). Table 5.3 displays the main parameters of the converter driving circuit.

Table 5.3: Demo#2 converter driving circuit parameters.

Parameter	Value
Total gate resistance R'_{g}	60 Ohm
Leakage inductance L_{lk}	4 uH
Magnetizing inductance L_{m}	285 uH
Interwinding capacitance C_{w}	0.3 pF
MOSFET input capacitance C_{ies}	7.8 nF
Steady-state balancing resistor R_{B}	10 MOhm

The low drain-to-source leakage current of the IXTX20N150 MOSFETs, tailor-made for capacitor discharge applications, in regard to the leakage current of the IXFK20N120 MOSFETs, allowed for the steady-state balancing resistors to be increased by 33 %. Indeed, at rated drain-to-source voltage and with their gate and source electrodes short-circuited, the IXFK20N120 MOSFETs report

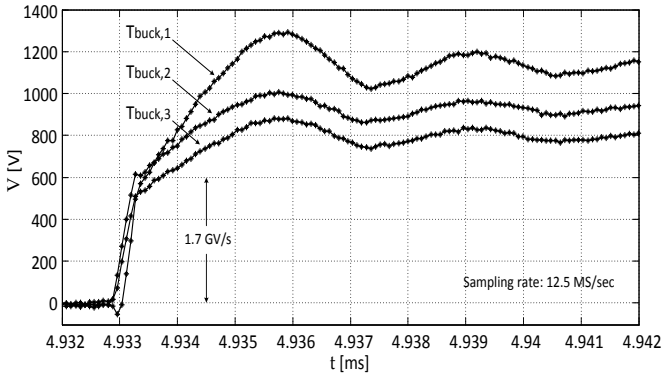

Figure 5.8: Blocking voltages of the serialized switches at their turn-off transient period during a buck function, as they were recorded by pseudo-differential measurements conducted via high-bandwidth high-voltage PPE LeCroy$^{\mathrm{TM}}$ probes for a 9 uF pseudo-DEAP load (V_{DEAP} = 2200 V and $I_{L_{\mathrm{s,peak}}}$= 3 A).

100 uA leakage current at 25 °C and 2 mA at 125 °C, while the IXTX20N150 MOSFETs report only 50 uA and 750 uA at the respective junction temperatures. Yet, and apart from the actual MOSFETs employed, in either demo#1 or demo#2, all serialized switches were driven in their off-state by −7 V pulses limiting their drain-to-source leakage current further more [**?**].

During the converter energy efficiency mapping the primary-side peak-current was limited to 15 A for both buck and boost functions to avoid saturation of the tapped-inductance core. The pseudo-DEAP voltage, on the other hand, was limited by the breakdown voltage of the serialized switches, considering a 15 % safety margin. Indeed, as seen in Fig. 5.8, during the buck function and while the pseudo-DEAP voltage was 2200 V, the drain-to-source voltage across the switch turning-off faster, i.e. $T_{buck,1}$, approached the 1300 V threshold. According to (4.1) the overall steady-state blocking voltage across the stacked switches was 3000 V and the transient overvoltage can be estimated as 3200 V. Hence, the recorded overshoot between the fastest and the slowest switch during the buck function reflected only 13 % of the steady-state blocking voltage, thus verifying the effectiveness of the serialized string when driving a 9 uF load.

Various experiments were conducted in an effort to assess the converter reconfiguration effect on the performance of the serialized chain. Indicatively, Fig. 5.9 illustrates the blocking voltages of the serialized switches, during the buck function and while the pseudo-DEAP voltage was 1800 V and the secondary-side peak-current was 1 A, for the case of a 9 uF and a 500 nF load. Although, in both experiments the overall steady-state blocking voltage across

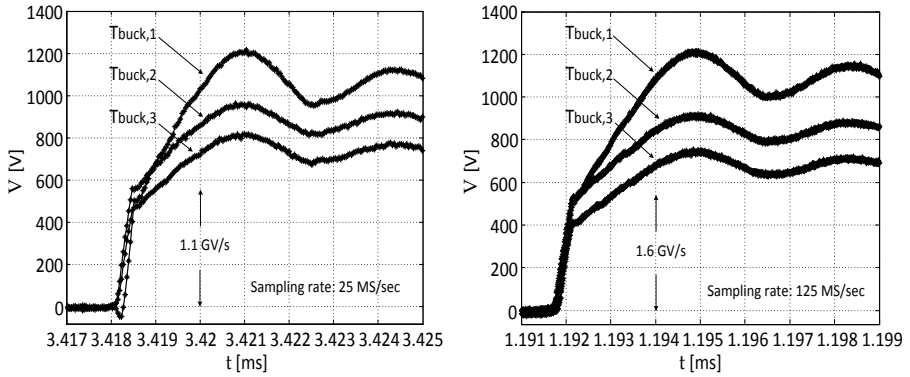

(a) (b)

Figure 5.9: Blocking voltages of the serialized switches at their turn-off transient period during a buck function, as they were recorded by pseudo-differential measurements conducted via high-bandwidth high-voltage PPE LeCroy^{TM} probes for a (a) 9 uF (b) 500 nF pseudo-DEAP load (V_{DEAP} = 1800 V and $I_{L_{s,peak}}$= 1 A).

the stacked switches can be calculated as 2600 V, the recorded overshoot between the fastest and the slowest switch was approximately 50 V higher in the case of the 500 nF load. Evidently though, and as highlighted in Figs. 5.9(a) and 5.9(b), the effectiveness of the serialized string was aggravated in the corresponding experiment by an approximately 50 % higher voltage rate of change.

Nevertheless, as in all conducted experiments and regardless of the load in use, the recorded overshoot between the fastest and the slowest switch during the buck function reflected less than 20 % of the steady-state blocking voltage, and all drain-to-source voltages seemed to ascent synchronously, no further design effort was considered necessary prior to conducting demo#2 energy harvesting experiments. Besides, an inevitable trade-off had to be made while sizing the RCD snubber S_2 capacitance C_2, between a non-destructive voltage overshoot across the serialized string and a wide-range energy efficient converter operation.

5.3.3 Energy harvesting

Several energy harvesting experiments were successfully conducted in demo#2 employing one of the viable generators described in Table 5.2. In all experiments, and in order to protect the DEAP generator in use, the operating E-field strength was sustained below 25 V/um and the converter peak-current reference was set to 1 A during both buck and boost functions. Yet, even though the peak-current reference was well-sustained in relatively low values, the driven load substantial size reduction challenged the accuracy of the converter DEAP voltage control loop severely; rendering the formation of antagonistic CV and CE cycles unrealistic. Hence, only CC energy harvesting experiments were successfully conducted in demo#2 and Table 5.4 summarizes their key parameters.

Table 5.4: Demo#2 key energy harvesting experiment parameters.

Parameter	Value
Delta-strain	60 %
Cycling frequency f	1 Hz
Geometrical constant α	0.73
Maximum attainable E-field $E_{\max}$	25 V/um

Figure 5.10 illustrates the progression of the DEAP generator voltage over time during a 60 % delta-strain at 1 Hz experiment, while the tapped-inductor buck-boost converter was programmed to boost the voltage of the stretched DEAP generator to 1200 V and subsequently buck it to 700 V when at the

5.5 % pre-stretch position. Undoubtedly, the external DC power supply abrupt disconnection at $t = 0.25$ sec followed a non-periodic DEAP voltage pattern; highlighting the converter DEAP voltage control loop impaired operation.

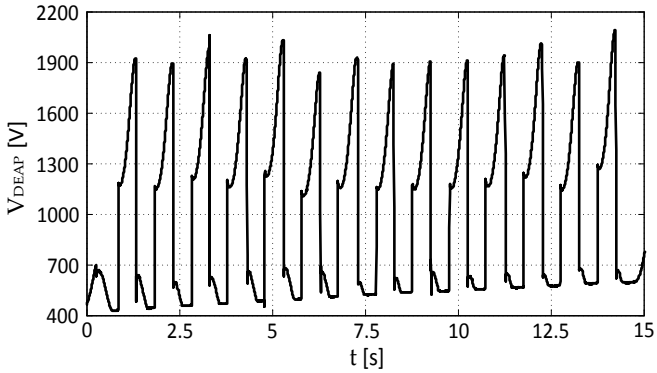

Figure 5.10: DEAP voltage time progression during a 60 % delta-strain at 1 Hz energy harvesting experiment conducted on the mechanical test rig of the horizontal demo#0.

The respective progression of the DC-link voltage is depicted in Figure 5.11, where it is once more straightforwardly concluded that energy was successfully harvested after the completion of every cycle, as the DC-link voltage increased gradually over time. Furthermore, it is also clear, considering the DEAP generators relative size, that the inherent DC-leakage limitation of the bidirectional tapped-inductor buck-boost converter, first appreciated in Fig. 4.3, was, in this experiment, significantly attenuated by both the increase of the DEAP generator cycling frequency and the increase of the steady-state balancing resistors.

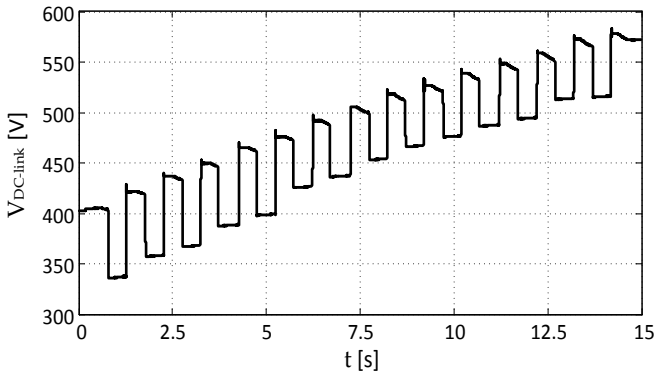

Figure 5.11: DC-link voltage time progression during a 60 % delta-strain at 1 Hz energy harvesting experiment conducted on the mechanical test rig of the horizontal demo#0.

Indeed, neglecting probe and DEAP generator internal loss, in the 60 % delta-strain at 0.75 Hz demo#1 experiment presented in Figs. 4.12 and 4.13 the DEAP voltage progressed from 1100 V up to 1730 V, during the relaxation phase, indicating that the DEAP generator leaked 335 mJ towards the converter, while during the 60 % delta-strain at 1 Hz demo#2 experiment presented in Figs. 5.10 and 5.11 the DEAP voltage progressed from 1170 V up to 1900 V, during the respective phase, indicating that the corresponding DEAP generator leaked only 235 mJ. Table 5.5 summarizes the best documented results of a single CC cycle during demo#2 energy harvesting experiments.

Table 5.5: Demo#2 energy harvesting experiments outcome.

Parameter	Demo#2
Energy gain ΔU	0.28 J
Absolute energy gain $\Delta U_{\mathrm{CC,abs}}$	1.16 J
Energy conversion efficiency η_{con}	3.7 %
Energy harvesting cycle efficiency η_{cycle}	23.6 %
Effective mechanical potential energy $U_{\mathrm{m,eff}}$	7.4 J

During the demo#2 experiment presented in Table 5.5 the boost function of the converter stepped-up the voltage of the stretched generator from 580 V to 1170 V with 90 % energy efficiency, while the buck function of the converter stepped-down the voltage of the relaxed DEAP generator from 1900 V to 695 V with 93 % energy efficiency, indicating that the overall converter loss was equal to 94 mJ; 33 % of the energy gain. Yet, demo#2 tapped-inductor buck-boost converter was indisputably overdesigned for the viable DEAP generator at hand.

5.4 Summary

This chapter introduced demo#2, a third complete DEAP generator energy harvesting system. Unfortunately though, primarily due to the early breakdowns of the corresponding voluminous DEAP generators, the demonstrator primary and secondary kick-off goals were not met. Nonetheless, the demonstrator effectiveness was validated by employing new smaller scale generators. Finally, both the operation of the power electronic converter employed in demo#2 and the performance of its serialized chain were extensively characterized, verifying the former one's applicability to DEAP energy harvesting systems.

This page is intentionally left blank

Chapter 6

Conclusions & Perspective

This chapter highlights the fundamental conclusions of the PhD project and outlines a short perspective of the DEAP technology, based on the accumulated experience of the three (3) complete energy harvesting systems designed, assembled and thoroughly tested within the former one's three-years framework.

6.1 Conclusions

The major conclusions of the PhD project are strongly bonded to its primary objectives and as such they are correspondingly delineated.

⋆ *Design and validate an electromechanical model for a DEAP generator.*

A meticulous and highly accurate electromechanical model of a cube-shaped DEAP generator was thoroughly presented in Chapter 2. The designed model accounted for both the visco-hyperelastic characteristics of the elastomer as well as for the latter one's stretch-dependent capacitance. Concisely, a Zener model, comprising of a single elastic spring in parallel with a Maxwell arm, characterized by a stretch and stretch rate dependent damping parameter, was employed to model the visco-hyperelastic properties of the elastomer, while the stretch-dependence of the latter one's capacitance was experimentally identified.

Chapter 2 outlined results demonstrate a strong match between the actual measured force imposed on the DEAP generator and the one predicted by the model, during both the steady-state interval and the transient charging and discharging instances of the DEAP generator, under all energy harvesting cycles, thus validating the effectiveness and the applicability of the designed model.

Future work includes, but is not restricted to, in-depth modelling of the DEAP generator energy harvesting system, thus forecasting the actual energy gain, energy harvesting efficiency and energy conversion efficiency, for different energy harvesting cycles and various delta-strain and cycling frequency configurations.

⋆ *Outline and compare the DEAP generator fundamental energy harvesting cycles, i.e. CC, CV and CE, based on actual tangible experimental results.*

The DEAP generator energy harvesting cycles were for the first time experimentally outlined in Chapter 3 on the first complete DEAP energy harvesting system, i.e. demo#0. The outcome of the CV experiment highlighted the fact that the respective energy harvesting cycle should not be considered as a counterpart for the CC cycle, as the respective literature indicates, as in practical applications besides less relative energy gain it offers less energy gain as well. In addition, the CC cycle appeared to offer higher energy gain than the CE cycle, in contrast with the respective theory, highlighting the importance of a high-efficient power electronic converter in a DEAP energy harvesting system.

Unfortunately, even though additional investigation on the energy harvesting cycles of a DEAP generator was one of the kick-off goals of demo#2, the analogous experimentation was rendered impossible after the early breakdown of demo#2 voluminous DEAP generators. Yet, given the successful design of such generators, further practical experimentation on their energy harvesting cycles, may consist of performance monitoring when driven at high operating E-field strength values, where the generated dielectric stress will not be several orders of magnitude less in regard to the mechanical stress cycling the elastomer sheets.

⋆ *Optimize the serialization of a finite number of off-the-shelf non-matched non-thermally coupled power-MOSFETs via a merely passive stacking technique.*

An old passive stacking approach, known as the gate balancing core technique, was in Chapter 4 revisited, and a new design specification for its transformers interwinding capacitance was derived, leading to the revised gate balancing core technique; a new and simple passive approach for serializing off-the-shelf non-matched non-thermally coupled power-MOSFETs. The latter one's effectiveness was first tested on demo#1 tapped-inductor buck-boost prototype, where three (3) 1200 V IXYS HiPerFET™ serialized MOSFETs (model IXFK20N120) demonstrated proficient performance, while driving a steady-state blocking voltage of 2600 V, with just a 10 % overshoot between the fastest and slowest switch transient drain-to-source voltages; ascending at 850 MV/s.

The revised gate balancing core technique was also employed in Chapter 5, where three (3) 1500 V IXYS HiPerFET™ MOSFETs (model IXYX20N150) were serialized to extend the operational voltage range of the tapped-inductor buck-boost converter associated with demo#2. Indeed, an experiment on a 3000 V steady-state blocking voltage verified the effectiveness of the serial-

ized string, with just a 13 % overshoot between the fastest and slowest switch transient drain-to-source voltages; the rate of change of which was 1.7 GV/s.

Related future work may focus on assessing the performance of stacked, via the revised gate balancing core technique, switches, while the former ones are driven under different operating conditions, as for example various junction temperatures. Further research may also engage the transformer(s) design, aiming at optimizing the serialized devices switching characteristics and associated loss.

⋆ *Design, assemble and assess the operation of a novel high-efficient power electronic converter enabling the energy harvesting process of a DEAP generator.*

A typical non-isolated half-bridge buck-boost converter, incorporating - among else - an analogue peak-current controller, was employed in demo#0, to enable the DEAP generator and to form the CC, CV and CE energy harvesting cycles. Indeed, mechanical energy was successfully converted into electrical one, under all three (3) distinct energy harvesting cycles, with the CC cycle demonstrating superior performance to the CV and CE ones, harnessing 106.6 mJ at 40 % delta-strain and 0.85 Hz, characterized by a 3.5 % energy conversion efficiency.

A novel tapped-inductor buck-boost prototype, facilitating both high-efficient bidirectional energy flow as well as high step-up and high step-down voltage conversion ratios, by employing a serialized chain of three (3) off-the-shelf 1200 V IXYS MOSFETs (model IXFK20N120) based on the revised gate balancing core technique, was subsequently designed in demo#1. The open-loop prototype was used to drive a 1 uF DEAP generator, achieving energy generation of 0.42 J, at a 60 % delta-strain and 0.75 Hz CC cycle, characterized by a 7 % energy conversion efficiency and a 2 J/kg of active material energy density.

Finally, the highly reliable control platform of the half-bridge buck-boost converter designed in demo#0 was integrated with the highly efficient tapped-inductor buck-boost prototype designed in demo#1, leading to the converter design used in demo#2. Indeed, demo#2 converter boost function operated with energy efficiency in the vicinity of 92 %, for a wide range of operational voltages and primary-side peak-current references, while its buck function reported energy efficiency above 94 % in the corresponding operational points. Yet, as all voluminous DEAP generators reported early breakdowns, the converter was only used to drive a 450 nF generator, reporting energy generation of 0.28 J, at a 60 % delta-strain and 1 Hz CC cycle, characterized by a 3.7 % energy conversion efficiency and a 0.7 J/kg of active material energy density.

Apart from enabling the DEAP generator energy harvesting process, demo#2 converter provided a valuable input to various modern power electronic disciplines, such as radar modulators, X-ray generators and propulsion inverters, which, up until today, are rather limited by the lack of high-efficient, high-voltage and fast-switching devices, as its prominent operation was based on a

well-synchronized string of three (3) off-the-shelf non-matched non-thermally coupled 1500 V IXYS HiPerFET™ MOSFETs (model IXYX20N150). Future work on demo#2 converter may focus on increasing its efficiency further more, either by optimizing the tapped-inductance design, or by employing smart driving techniques as synchronous rectification and quasi-resonant Valley switching.

6.2 Perspective

The DEAP technology perspective analysis is classified into three (3) main research areas; namely the DEAP Material Research and Development, the DEAP Film Production and last but no least the Power Electronic Converters.

DEAP Material Research and Development

The project's kick-off goal in 2011, regarding the DEAP material research and development phase, was the continuous upgrade of the former one's characteristics - especially its rated E-field strength value - starting from material Version#1 (V1) and ending to material Version#5 (V5). Unfortunately, all WP7 DEAP generators were for practical reasons restricted to material Version#2 (V2) and material Version#3 (V3). As a figure of merit, Table 6.1, summarizes the main electrical characteristics of V3 and V5 DEAP materials.

Table 6.1: DEAP material V3 and V5 main electrical characteristics.

Characteristic	V3	V5
Rel. Permittivity ε_{rel}	3.1	≥ 10
Single-layer film thickness d_z	$60 - 80$ um	$20 - 30$ um
Rated E-field strength E_{rated}	60 V/um	≥ 100 V/um

Nonetheless, multiple types of candidate elastomers have already been identified towards future high-performance DEAP films [**?**]. However, the electrical specifications of these prominent elastomers have been reconceptualized. Indeed, targeted research indicated that even though commercialisation of today's DEAP generators demands for electrical characteristics in the proximity of V5, still, in order to achieve a commercially-wise reasonable lifetime, such performance should be accompanied by relatively low operating voltages [**?**]. Hence, further research should mainly focus on increasing the elastomer relative permittivity rather than its rated E-field strength; a misconceived fact in 2011.

Yet, when high-permittivity elastomers were designed in the framework of this project, static hysteresis turned-out to be an important parameter, which could not be any more neglected as the dielectric loss increased dramatically. Undeniably, one of the biggest challenges towards the commercialization of DEAP generators is the design of very high-permittivity materials ($\varepsilon_{\text{rel}} > 50$), which will at the same time be characterized by sufficiently low dielectric loss.

DEAP Film Production

Upon the project's commencement in 2011 all DEAP film production processes and associated line machinery were subjected to rigorous re-evaluation, in an effort to overcome the limitations of the DEAP film prototype production line. Indeed, most of the DEAP film processing practices were significantly altered. Indicatively, a new coating process, capable of handling silicone with nanoparticles and a solvent, was implemented and integrated in Danfoss PolyPower® A/S coating line, enabling the production of a 20 um thick DEAP-coated film.

Generally speaking, all processes associated with the production of unmetallized DEAP film were upgraded. Concepts for improving the performance of the metallization process were also addressed, even though the respective machinery was excluded from any radical enhancement due to budget limitations. Yet, DEAP generators, based on segmented film laminations, as such a structure increases the overall unit redundancy and lifetime in regard to a similarly rated monolithic design, may even be manufactured by today's production line [**?**].

Hence, not only was the already capable of producing several kilometres of DEAP film per week roll-to-roll production process, significantly improved within the framework of this project, leading to a nearly seamless electroactive elastomer, but that improvement did not impose any limitations in the segmentation of DEAP film laminations for future generator designs as well. Thus, considering that no cost estimation was made due to the early phase of the development, the DEAP film production process may not - at date - be considered as a bottleneck towards the commercialization of the technology.

Power Electronic Converters

Back in 2011, the design of a pertinent power electronic converter seemed to be one of the main hindrances prior to the establishment of the DEAP generator as a marketable product, due to the challenging necessity for bidirectional energy flow, under high step-up and high step-down voltage conversion ratios, accompanied by low-average but relatively high-peak currents. However, three (3) years of experience within the project's WP7 have ascertained that such a high-efficient converter may be attained by serializing a number of MOSFETs.

Howbeit, the upcoming restriction of the DEAP generator operating voltages in the range of few hundred volts, in order to prolong its lifetime, facilitates the design of the corresponding power electronic converter as well. Indeed, with today's commercially-available high-efficient low and medium-power Silicon (Si) MOSFETs rated up to 1500 V the need to serialize a number of them to accommodate the DEAP generator operating voltages may be rendered obsolete.

Besides, recent advancements in wide-bandgap semiconductor materials, like SiC, have demonstrated that these materials hold a lot of promise as candidate competitors of Si MOSFETs in low, medium and high-power applications. Indeed, since Cree™ first published its SiC MOSFETs rated up to 1700 V [**?**, **?**], tremendous work has been conducted on these devices with recent research revealing 10 kV 120 A SiC MOSFETs [**?**]. Evidently, if the reliability and market price of SiC MOSFETs proves to be antagonistic with that of conventional Si MOSFETs in the near future, then the design of a high-efficient converter for high-power DEAP energy harvesting systems will not impose a significant challenge towards the latter one's intensive commercialization.

Bibliography

[1] M. Schwartz, *Smart Materials*, 1st ed., CRC Press, 2008.

[2] F. Carpi, D. D. Rossi, R. Kornbluh, R. Pelrine, and P. Sommer-Larsen, *Dielectric Elastomers as Electromechanical Transducers*, 1st ed., Elsevier, 2008.

[3] Y. Bar-Cohen, *Electroactive Polymer (EAP) Actuators as Artificial Muscles - Reality, Potential and Challenges*, 2nd ed., SPIE Press, 2004.

[4] Google Patents. [Online]. Available: www.google.com/patents

[5] United States Patent and Trademark Office. [Online]. Available: www.uspto.gov

[6] European Patent Office. [Online]. Available: www.epo.org

[7] World Intellectual Property Organization. [Online]. Available: www.wipo.int

[8] Danfoss PolyPower. [Online]. Available: www.polypower.com

[9] J. E. Huber, N. A. Fleck, and M. F. Ashby, "The selection of mechanical actuators based on performance indices," in *Mathematical, physical and engineering sciences*, vol. 453, no. 1965, Oct. 1997, pp. 2185–2205.

[10] A. D. Poole and J. D. Booker, "Design methodology and case studies in actuator selection," in *Mechanism and Machine Theory*, vol. 46, no. 5, May 2011, pp. 647–661.

[11] "Polypower DEAP material," White Paper, Danfoss PolyPower A/S, Dec. 2012.

[12] SRI International. [Online]. Available: www.sri.com

[13] Q. Pei, M. A. Rosenthal, R. Pelrine, S. Stanford, and R. D. Kornbluh, "Multifunctional electroelastomer roll actuators and their application for biomimetic walking robots," in *Smart Structures and Materials 2003:*

Electroactive Polymer Actuators and Devices (EAPAD), Proc. SPIE, vol. 5051, Jul. 2003, pp. 281–290.

[14] R. Zhang, P. Lochmatter, A. Kunz, and G. M. Kovacs, "Spring roll dielectric elastomer actuators for a portable force feedback glove," in *Smart Structures and Materials 2006: Electroactive Polymer Actuators and Devices (EAPAD), Proc. SPIE*, vol. 6168, Mar. 2006, pp. 1–12.

[15] G. M. Kovacs, S. M. Ha, S. Michel, R. Pelrine, and Q. Pei, "Study on core free rolled actuator based on soft dielectric EAP," in *Smart Structures and Materials 2008: Electroactive Polymer Actuators and Devices (EAPAD), Proc. SPIE*, vol. 6927, Apr. 2008, pp. 1–15.

[16] M. Tryson, H. E. Kiil, and M. Benslimane, "Powerful tubular core free dielectric electro activate polymer (DEAP) PUSH' actuator," in *Smart Structures and Materials 2009: Electroactive Polymer Actuators and Devices (EAPAD), Proc. SPIE*, vol. 7287, Apr. 2009, pp. 1–11.

[17] M. Y. Benslimane, H. E. Kiil, and M. J. Tryson, "Dielectric electroactive polymer push actuators: performance and challenges," in *Polym. Int.*, vol. 59, 2010, pp. 415–421.

[18] P. Thummala, Z. Zhang, M. A. E. Andersen, and S. Rahimullah, "Dielectric electro active polymer incremental actuator driven by multiple high-voltage bi-directional DC-DC converters," in *Energy Conversion Congress and Exposition (ECCE)*, Denver, CO, Sep. 2013, pp. 3837–3844.

[19] D. Nielsen, A. Knott, and M. A. E. Andersen, "A high-voltage class D audio amplifier for dielectric elastomer transducers," in *Twenty-Ninth Annual IEEE Applied Power Electronics Conference and Exposition (APEC)*, Forth Worth, TX, Mar. 2014, pp. 3278–3283.

[20] L. Huang, Z. Zhang, and M. A. E. Andersen, "Design and development of autonomous high voltage driving system for DEAP actuator in radiator thermostat," in *Twenty-Ninth Annual IEEE Applied Power Electronics Conference and Exposition (APEC)*, Forth Worth, TX, Mar. 2014, pp. 1633–1640.

[21] Artificial Muscle inc. [Online]. Available: www.artificialmuscle.com

[22] Bayer. [Online]. Available: www.materialscience.bayer.com

[23] mophie. [Online]. Available: www.mophie.com

[24] StretchSense. [Online]. Available: www.stretchsense.com

[25] S. J. A. Koh, C. Keplinger, T. Li, S. Bauer, and Z. Suo, "Dielectric elastomer generators: How much energy can be converted?" *IEEE/ASME Trans. Mechatronics*, vol. 16, no. 1, pp. 33–41, Feb. 2011.

[26] S. J. A. Koh, , X. Zhao, and Z. Suo, "Maximal energy that can be converted by a dielectric elastomer generator," *Appl. Phys. Lett.*, vol. 94, no. 26, pp. 262 902–262 902–3, Jun. 2009.

[27] R. Pelrine, R. D. Kornbluh, J. Eckerle, P. Jeuck, S. Oh, Q. Pei, and S. Stanford, "Dielectric elastomers: Generator mode fundamentals and applications," in *Smart Structures and Materials 2001: Electroactive Polymer Actuators and Devices (EAPAD), Proc. SPIE*, vol. 4349, San Diego, California, Jul. 2001, pp. 148–156.

[28] C. Graf, J. Maas, and D. Schapeler, "Energy harvesting cycles based on electro active polymers," in *Smart Structures and Materials 2010: Electroactive Polymer Actuators and Devices (EAPAD), Proc. SPIE*, vol. 764217, San Diego, California, Mar. 2010, pp. 1–12.

[29] ——, "Optimized energy harvesting based on electro active polymers," in *10th IEEE International Conference on Solid Dielectrics (ICSD)*, Postdam, Jul. 2010, pp. 1–5.

[30] B. Czech, R. van Kessel, P. Bauer, and J. A. Ferreira, "Dielectric elastomers as generators," in *Proceedings of the 14th European Conference on Power Electronics and Applications (EPE)*, Birmingham, Aug./Sep. 2011, pp. 1–10.

[31] R. van Kessel, A. Wattez, and P. Bauer, "The effect of converter efficiency on DEAP-based energy conversion: an overview and optimization method," in *Smart Structures and Materials 2014: Electroactive Polymer Actuators and Devices (EAPAD), Proc. SPIE*, vol. 9056, San Diego, California, Mar. 2014, pp. 1–12.

[32] E. Dimopoulos, I. Trintis, and S. Munk-Nielsen, "Energy harvesting cycles of dielectric electroactive polymer generators," in *38th Annual Conference on IEEE Industrial Electronics Society, IECON*, Montreal, QC, Oct. 2012, pp. 374–381.

[33] ——, "Comparison of the dielectric electroactive polymer generator energy harvesting cycles," in *Smart Structures and Materials 2013: Electroactive Polymer Actuators and Devices (EAPAD), Proc. SPIE*, vol. 8687, San Diego, California, Apr. 2013, pp. 86 870O–1–86 870O–13.

[34] E. Dimopoulos, I. Trintis, S. Munk-Nielsen, B. Rechenbach, M. Willatzen, and B. Lassen, "An electromechanical model for a dielectric electroactive polymer generator," in *15th European Conference on Power Electronics and Applications, EPE*, Lille, France, Sep. 2013, pp. 1–10.

[35] H. Prahlad, R. Kornbluh, R. Pelrine, S. Stanford, J. Eckerle, and S. Oh, "Polymer power: Dielectric elastomers and their applications in distributed actuation and power generation," in *International Conference*

on Smart Materials Structures and Systems, Proc. ISSS, Bangalore, India, Jul. 2005, pp. SA100–SA107.

[36] C. Jean-Mistral, S. Basrour, and J.-J. Chaillout, "Dielectric polymer: scavenging energy from human motion," in *Smart Structures and Materials 2008: Electroactive Polymer Actuators and Devices (EAPAD), Proc. SPIE*, vol. 6927, San Diego, California, Apr. 2008, pp. 1–10.

[37] S. Chiba, M. Waki, R. Kornbluh, and R. Pelrine, "Innovative power generators for energy harvesting using electroactive polymer artificial muscles," in *Smart Structures and Materials 2008: Electroactive Polymer Actuators and Devices, Proc. SPIE*, vol. 6927, San Diego, California, Apr. 2008, pp. 1–8.

[38] ——, "Innovative wave power generation system using electroactive polymer artificial muscles," in *IEEE Oceans Europe*, Bremen, May 2009, pp. 1–3.

[39] R. Kornbluh, R. Pelrine, H. Prahlad, A. Wong-Foy, B. McCoy, S. Kim, J. Eckerle, and T. Low, "From boots to buoys: Promises and challenges of dielectric elastomer energy harvesting," in *Smart Structures and Materials 2011: Electroactive Polymer Actuators and Devices (EAPAD), Proc. SPIE*, vol. 7976, San Diego, California, Mar. 2011, pp. 1–19.

[40] R. Vertechy, M. Fontana, G. P. R. Papini, and D. Forehand, "In-tank tests of a dielectric elastomer generator for wave energy harvesting," in *Smart Structures and Materials 2014: Electroactive Polymer Actuators and Devices (EAPAD), Proc. SPIE*, vol. 9056, San Diego, California, Mar. 2014, pp. 1–11.

[41] P. Jean, A. Wattez, G. Ardoise, C. Melis, R. van Kessel, A. Fourmon, E. Barrabino, J. Heemskerk, and J. P. Queau, "Standing wave tube electro active polymer wave energy converter," in *Smart Structures and Materials 2012: Electroactive Polymer Actuators and Devices (EAPAD), Proc. SPIE*, vol. 83400C, San Diego, California, Apr. 2012, pp. 1–21.

[42] P. Jean, W. Jenninger, D. Lovera-Prieto, D. Schapeler, and J. Wagner, "Electromechanical converter, method for producing same, and use thereof," Patent WO 2 011 161 052 A3, Jun., 2012.

[43] H. Wang, C. Wang, and T. Yuan, "On the energy conversion and efficiency of a dielectric electroactive polymer generator," *Appl. Phys. Lett.*, vol. 101, no. 3, pp. 033 904–1–033 904–5, Jul. 2012.

[44] R. Kaltseis, C. Keplinger, R. Baumgartner, M. Kaltenbrunner, T. Li, P. Mächler, R. Schwödiauer, Z. Suo, and S. Bauer, "Method for measuring energy generation and efficiency of dielectric elastomer generators," *Appl. Phys. Lett.*, vol. 99, no. 16, pp. 2904–1–2904–3, Oct. 2011.

[45] J. Huang, S. Shian, Z. Suo, and D. R. Clarke, "Dielectric elastomer generator with equi-biaxial mechanical loading for energy harvesting," in *Smart Structures and Materials 2013: Electroactive Polymer Actuators and Devices (EAPAD), Proc. SPIE*, vol. 86870Q, San Diego, California, Apr. 2013, pp. 1–11.

[46] S. Shian, J. Huang, S. Zhu, and D. R. Clarke, "Optimizing the electrical conversion cycle of dielectric elastomer generators," *Adv. Mater.*, vol. 26, no. 38, pp. 1–5, Aug. 2014.

[47] T. McKay, B. O'Brien, E. Calius, and I. Anderson, "Realizing the potential of dielectric elastomer generators," in *Smart Structures and Materials 2011: Electroactive Polymer Actuators and Devices (EAPAD), Proc. SPIE*, vol. 79760B, San Diego, California, Mar. 2011, pp. 1–8.

[48] J. Due, S. Munk-Nielsen, and O. Rasmus, "Energy harvesting with dielectro active polymers," in *5th IET International Conference on Power Electronics, Machines and Drives (PEMD)*, Brighton, UK, Apr. 2010, pp. 1–6.

[49] E. Dimopoulos and S. Munk-Nielsen, "A tapped-inductor buck-boost converter for a dielectric electroactive polymer generator," in *Twenty-Ninth Annual IEEE Applied Power Electronics Conference and Exposition (APEC)*, Fort Worth, TX, Mar. 2014, pp. 3125–3131.

[50] ——, "A tapped-inductor buck-boost converter for a multi-DEAP generator energy harvesting system," in *Smart Structures and Materials 2011: Electroactive Polymer Actuators and Devices (EAPAD), Proc. SPIE*, vol. 90560J, San Diego, California, Mar. 2014, pp. 1–11.

[51] 3M. [Online]. Available: www.3m.com

[52] H. E. Kiil and M. Benslimare, "Scalable industrial manufacturing of DEAP," in *Smart Structures and Materials 2009: Electroactive Polymer Actuators and Devices (EAPAD), Proc. SPIE*, vol. 7287, San Diego, California, Apr. 2009, pp. 1–10.

[53] M. Y. Benslimane and P. Gravesen, "Mechanical properties of dielectric elastomer actuators with smart metallic compliant electrodes," in *Smart Structures and Materials 2002: Electroactive Polymer Actuators and Devices (EAPAD), Proc. SPIE*, vol. 4695, San Diego, California, Jul. 2002, pp. 150–157.

[54] M. Y. Benslimane, H. E. Kiil, and M. J. Tryson, "Electromechanical properties of novel large strain polypower film and laminate components for DEAP actuator and sensor applications," in *Smart Structures and Materials 2010: Electroactive Polymer Actuators and Devices (EAPAD), Proc. SPIE*, vol. 7642, San Diego, California, Apr. 2010, pp. 1–11.

[55] M. Y. Benslimane and P. Gravesen, "A dielectric composite and a method of manufacturing a dielectric composite," Patent WO 2 008 052 559 A2, May, 2008.

[56] Z. Suo, "Theory of dielectric elastomers," *Acta Mechanica Solida Sinica*, vol. 23, no. 6, pp. 549–578, Dec. 2010.

[57] P. Lochmatter, G. Kovacs, and M. Wissler, "Characterization of dielectric elastomer actuators based on a visco-hyperelastic film model," *Smart Materials and Structures*, vol. 16, no. 2, pp. 477–486, 2007.

[58] G. Kofod, "The static actuation of dielectric elastomer actuators: how does pre-stretch improve actuation?" *J. Phy. D. Appl. Phys.*, vol. 41, no. 21, pp. 1–11, Oct. 2008.

[59] P. Haupt and K. Sedlan, "Viscoplasticity of elastomeric materials: experimental facts and constitutive modelling," *Archive of Applied Mechanics*, vol. 71, no. 2-3, pp. 89–109, Mar. 2001.

[60] J.-S. Lai and D. J. Nelson, "Energy management power converters in hybrid electric and fuel cell vehicles," *Proceedings of the IEEE*, vol. 95, no. 4, pp. 766–777, Apr. 2007.

[61] S. Aso, M. Kizaki, and Y. Nonobe, "Development of fuel cell hybrid vehicles in TOYOTA," in *Power Conversion Conference*, Nagoya, Apr. 2007, pp. 1606–1611.

[62] R. M. Schupbach and J. C. Balda, "Comparing DC-DC converters for power management in hybrid electric vehicles," in *IEEE International Electric Machines and Drives Conference (IEMDC)*, vol. 3, Jun. 2003, pp. 1369–1374.

[63] D. Yu, X. Zhou, S. Bai, S. Lukic, and A. Huang, "Review of non-isolated bi-directional DC-DC converters for plug-in hybrid electric vehicle charge station application at municipal parking decks," in *Twenty-Fifth Annual IEEE Applied Power Electronics Conference and Exposition (APEC)*, Palm Springs, CA, Feb. 2010, pp. 1145–1151.

[64] R. Carbone, *Energy Storage in the Emerging Era of Smart Grids*, 1st ed., InTech, 2011.

[65] J. Zhang, "Bidirectional DC-DC power converter design, optimization, modeling and control," Ph.D. dissertation, Virginia Polytechnic Institute and State University, 2008.

[66] J. Zhang, J.-S. Lai, R.-Y. Kim, and W. Yu, "High-power density design of a soft-switching high-power bidirectional DC-DC converter," *IEEE Trans. Power Electron.*, vol. 22, no. 4, pp. 1145–1153, Jul. 2007.

[67] D. P. Urciuoli and C. W. Tipton, "Development of a 90kW bi-directional DC-DC converter for power dense applications," in *Twenty-First Annual IEEE Applied Power Electronics Conference and Exposition (APEC)*, Dallas, TX, Mar. 2006, pp. 1375–1378.

[68] N. Mohan, T. M. Undeland, and W. P. Robbins, *Power Electronics: Converters, Applications and Design*, 3rd ed., Wiley, 2003.

[69] R. W. Erickson and D. Maksimovic, *Fundamentals of Power Electronics*, 2nd ed., Springer, 2001.

[70] I. Trintis, E. Dimopoulos, and S. Munk-Nielsen, "Simple DCM or CRM analog peak current controller for HV capacitor charge-discharge applications," in *15th European Conference on Power Electronics and Applications, EPE*, Lille, France, Sep. 2013, pp. 1–7.

[71] M. A. Meyers and K. K. Chawla, *Mechanical Behavior of Materials*, 2nd ed., Cambridge University Press, 2008.

[72] T. Andersen, L. Huang, M. A. E. Andersen, and O. C. Thomsen, "Efficiency of capacitively loaded converters," in *Thirty-Eighth Annual IEEE Conference on Industrial Electronics Society (IECON)*, Montreal, QC, Oct. 2012, pp. 368–373.

[73] D. Maksimovic and S. Cuk, "Switching converters with wide DC conversion range," *IEEE Trans. Power Electron.*, vol. 6, no. 1, pp. 151–157, Jan. 1991.

[74] D. A. Grant, Y. Darroman, and L. Suter, "Synthesis of tapped-inductor switched-mode converters," *IEEE Trans. Power Electron.*, vol. 22, no. 5, pp. 1964–1969, Sep. 2007.

[75] B. W. Williams, "Unified synthesis of tapped-inductor DC-to-DC converters," *IEEE Trans. Power Electron.*, vol. 29, no. 10, pp. 5370–5383, Oct. 2014.

[76] N. Vazquez, L. Estrada, C. Hernandez, and E. Rodriguez, "The tapped-inductor boost converter," in *IEEE International Symposium on Industrial Electronics (ISIE)*, Vigo, Jun. 2007, pp. 538–543.

[77] K. Yao, M. Ye, M. Xu, and F. C. Lee, "Tapped-inductor buck converter for high-step-down DC-DC conversion," *IEEE Trans. Power Electron.*, vol. 20, no. 4, pp. 775–780, Jul. 2005.

[78] H. Cheng, K. M. Smedley, and A. Abramovitz, "A wide-input-wide-output WIWO DC-DC converter," *IEEE Trans. Power Electron.*, vol. 25, no. 2, pp. 280–289, Feb. 2010.

[79] D. G. Lamar, M. Fernandez, M. Arias, M. Hernando, and J. Sebastian, "Tapped-inductor buck HB-LED AC-DC driver operating in boundary

conduction mode for replacing incandescent bulb lamps," *IEEE Trans. Power Electron.*, vol. 27, no. 10, pp. 4329–4337, Oct. 2012.

[80] A. Abramovitz and K. Smedley, "Analysis and design of a tapped-inductor buck-boost PFC rectifier with low bus voltage," *IEEE Trans. Power Electron.*, vol. 26, no. 9, pp. 2637–2649, Sep. 2011.

[81] Y. Ye, K. Cheng, K. Ding, D. Wang, and Y. Bao, "Hybrid energy storage system and associated converters examination for DC distribution," in *5th International Conference on Power Electronics Systems and Applications (PESA)*, Hong Kong, Dec. 2013, pp. 1–7.

[82] Y. Huleihel, A. Cervera, and S. Ben-Yaakov, "A high gain DC-DC converter for energy harvesting of thermal waste by thermoelectric generators," in *27th IEEE Convention of Electrical & Electronics Engineers in Israel (IEEEI)*, Eilat, Nov. 2012, pp. 1–5.

[83] S. Hong, V. Chitta, . Narushima, and D. A. Torrey, "Series connection of IGBT's with active voltage balancing," *IEEE Trans. Ind. Appl.*, vol. 35, no. 4, pp. 917–923, Jul./Aug. 1999.

[84] J. Saiz, M. Mermet, D. Frey, P.-O. Jeannin, J. Schanen, and P. Muszicki, "Optimisation and integration of an active clamping circuit for IGBT series association," in *Thirty-Sixth IAS Annual Meeting, Industry Applications Conference, 2001*, vol. 2, Chicago, USA, Sep./Oct. 2001, pp. 1046–1051.

[85] C. Abbate, G. Busatto, and F. Iannuzzo, "High-voltage, high-performance switch using series connected IGBTs," *IEEE Trans. Power. Electron.*, vol. 25, no. 9, pp. 2450–2459, Sep. 2010.

[86] J.-F. Chen, J.-N. Lin, and T.-H. Ai, "The techniques of the serial and paralleled IGBTs," in *Proceedings of the 1996 IEEE 22nd International Conference on Industrial Electronics, Control, and Instrumentation*, vol. 2, Aug. 1996, pp. 999–1004.

[87] S. J. Finney, B. W. Willliams, and T. C. Green, "RCD snubber revisited," *IEEE Trans. Ind. Appl.*, vol. 32, no. 1, pp. 155–160, Jan./Feb. 1996.

[88] S. Buonomo, F. Distefano, A. Gaito, R. Scollo, F. Chimento, A. Raciti, S. Tomarchio, and D. Armenia, "Series connection of power switches in high input voltage with wide range power supply for gate driving application," in *Energy Conversion Congress and Exposition (ECCE)*, Phoenix, AZ, Sep. 2011, pp. 2985–2992.

[89] R. Withanage and N. Shammas, "Series connection of insulated gate bipolar transistors (IGBTs)," *IEEE Trans. Power Electron.*, vol. 27, no. 4, pp. 2204–2212, Apr. 2012.

[90] A. Raciti, G. Belverde, A. Galluzzo, G. Greco, M. Melito, and S. Musumeci, "Control of the switching transients of IGBT series strings by high-performance drive units," *IEEE Trans. Ind. Electron.*, vol. 48, no. 3, pp. 482–490, Jun. 2001.

[91] P. R. Palmer and A. N. Githiari, "The series connection of IGBTs with active voltage sharing," *IEEE Trans. Power Electron.*, vol. 12, no. 4, pp. 637–644, Jul. 1997.

[92] P. Anthony, N. McNeill, D. Holliday, D. Grant, and G. Hearn, "A magnetically isolated gate driver for high-speed voltage sharing in series-connected MOSFETs," in *Proceedings of the 14th European Conference on Power Electronics and Applications (EPE)*, Birmingham, Aug./Sep. 2011, pp. 1–10.

[93] H. L. Hess and R. J. Baker, "Transformerless capacitive coupling of gate signals for series operation of power MOS devices," *IEEE Trans. Power Electron.*, vol. 15, no. 5, pp. 923–930, Sep. 2000.

[94] K. Sasagawa, Y. Abe, and K. Matsuse, "Voltage-balancing method for IGBTs connected in series," *IEEE Trans. Ind. Appl.*, vol. 40, no. 4, pp. 1025–1030, Jul./Aug. 2004.

[95] Y. Abe, K. Matsubara, T. Mochida, K. Sasagawa, and K. Matsuse, "A novel method for loss reduction in high-voltage inverters," in *Fortieth IAS Annual Meeting. Conference Record of the Industry Applications Conference*, vol. 3, Oct. 2005, pp. 1849–1854.

[96] Y. Abe, K. Maruyama, Y. Matsumoto, K. Sasagawa, and K. Matsuse, "Performance of IGBTs series connection technologies for auxiliary power supply system," in *Power Conversion Conference*, Nagoya, Apr. 2007, pp. 1382–1387.

[97] E. Dimopoulos and S. Munk-Nielsen, "Serializing off-the-shelf MOSFETs by magnetically coupling their gate electrodes," in *15th European Conference on Power Electronics and Applications, EPE*, Lille, France, Sep. 2013, pp. 1–11.

[98] ——, "Scaling the serialization of MOSFETs by magnetically coupling their gate electrodes," in *Energy Conversion Congress and Exposition, ECCE*, Denver, CO, USA, Sep. 2013, pp. 3664–3670.

[99] T. V. Nguyen, P. Jeannin, E. Vagnon, D. Frey, and J.-C. Crebier, "Series connection of IGBT's with self-powering technique and 3-D topology," *IEEE Trans. Ind. Appl.*, vol. 47, no. 4, pp. 1844–1852, Jul./Aug. 2011.

[100] R. Kochetov, A. Tsekmes, and P. Morshuis, "Dielectric characterization of Danfoss EAP films," TU Delft, Tech. Rep., Jun. 2014.

[101] P. van der Meer, A. van Staveren, and A. van Roermund, *Low-Power Deep Sub-Micron CMOS logic: Sub-threshold Current Reduction*, 1st ed., Springer, 2005.

[102] J. J. Yde, "Highly efficient low cost energy generation and actuation using disruptive DEAP technology - Final Steering Committee Report," Tech. Rep., Apr. 2015.

[103] Cree. [Online]. Available: www.cree.com

[104] Press Release: Cree Launches Industry's First Commercial Silicon Carbide Power MOSFET; Destined to Replace Silicon Devices in High-Voltage ($\geq$ 1200 V) Power Electronics. [Online]. Available: http://www.cree.com/news-and-events/cree-news/press-releases/2011/january/110117-mosfet

[105] K. M. Das, C. Capell, D. Grider, R. Raju, M. Schutten, J. Nasadoski, S. Leslie, J. Ostop, and A. Hefner, "10 kV, 120 A SiC half H-bridge power MOSFET modules suitable for high frequency, medium voltage applications," in *Energy Conversion Congress and Exposition, ECCE*, Phoenix, AZ, USA, Sep. 2011, pp. 2689–2692.